CHAPTER IV

Variability in Rift Propagation in the Amery Ice Shelf, East Antarctica

4.1 Introduction

Mass loss from Antarctic ice shelves is dominated by basal melting and iceberg calving. Although these two processes account for roughly equal proportions of mass loss in total, the relative proportions vary greatly between ice shelves. Moreover, although iceberg calving events occur sporadically, when they do occur they remove large amounts of mass nearly instantaneously. This process forms part of the cycle of ice shelf advance and retreat with typical recurrence times between major calving events of the order of several decades. Most of Antarctica's ice shelves experience tabular calving events, in which large sections of ice break off, usually following the years-long propagation of a rift in the ice shelf (e.g. *Lazzara et al.*, 1999; *Jacobs et al.*, 1986). However, changes in calving style have been implicated in some of the most rapidly changing regions of Antarctica, specifically the ice shelves of the Antarctic Peninsula. *Scambos et al.* (2003) showed that the abrupt disintegration of both Larsen A and Larsen B ice shelves occurred following a series of abnormally warm summers. Not only were these disintegrations surprising in terms of size, but also in the speed at which they occurred. The acceleration of tributaries in the

wake of such disintegration events (*De Angelis and Skvarca*, 2003; *Rignot et al.*, 2004; *Scambos et al.*, 2004) served to further demonstrate that ice shelves are coupled to flow of inland ice and are capable of modulating ice dynamics of upstream grounded ice through buttressing effects (e.g. *Rignot et al.*, 2004; *Joughin and Alley*, 2011).

Iceberg calving is the result of the propagation of rifts in ice, and the increasing availability of satellite imagery has provided the ability to monitor the process of rift propagation and how it varies over more than a decade. *Fricker et al.* (2005) first used satellite imagery to create an eight-year time series (1996-2004) of observations of rift propagation in the Amery, focusing on two rifts near the calving front. These data suggested a seasonal trend in propagation (faster in Austral summer than in Austral winter). Field investigations at one of the rifts supported their observations of rifting rate (*Bassis et al.*, 2005, 2007, 2008). These studies also showed that rift propagation did not appear to be triggered by environmental stresses such as temperature, wind, or ocean swell, though their results did suggest that environmental factors might become more important as an iceberg becomes closer to detachment. A similar conclusion was reached based on modeling studies of rifts on the Filchner-Ronne, Ross and Fimbul ice shelves (*Larour et al.*, 2004; *Joughin and MacAyeal*, 2005; *Humbert and Steinhage*, 2011). This conclusion has been challenged by studies that have argued that ocean stresses, including strong pulses of storm induced swell, infra-gravity waves and the impact of tsunamis might drive rift propagation (*MacAyeal et al.*, 2006; *Sergienko*, 2010; *Brunt et al.*, 2011; *Bromirski and Stephen*, 2012).

We are motivated to study the Amery Ice Shelf rifts in depth in light of recent observations that showed rifting in the Amery to be unusually active (*Walker et al.*, submitteda). In that study 72 rifts in 12 ice shelves were monitored. Of those rifts only seven propagated continuously over the ten year observation interval, and five of those active rifts were located in the Amery Ice Shelf. We expand the study by *Fricker et al.* (2005) and examine the variability in rift propagation near the front

of the Amery Ice Shelf, deduced from satellite imagery from the Multi-angle Imaging SpectroRadiometer (MISR) and Moderate resolution Imaging Spectroradiometer (MODIS) in more detail.

4.2 The Amery Ice Shelf

Our study focuses on the Amery Ice Shelf, which is supplied by the seaward flow of ice from three main tributaries (Lambert Glacier, Mellor Glacier, and Fisher Glacier), and has a surface area of roughly 64342 km^2 (*Griggs and Bamber*, 2011). It has steadily advanced since its last major calving event in late 1963 or early 1964 (*Budd*, 1966; *Fricker et al.*, 2002; *Bassis et al.*, 2007). Several rifts have opened at the front (Fig. 4.1) which has advanced back to near its pre-calved position (Fig. 4.2). Two longitudinal-to-flow rifts initiated approximately 30 km apart in the late 1980s (L1 and L2) and propagated for several years. Around 1995, the tip of L1 split in two directions forming a triple junction, first observed in a 1996 satellite image (*Fricker et al.*, 2002).

We expand on the observational datasets acquired by *Fricker et al.* (2005) temporally and spatially. We continued to monitor the central rifts, T1 and T2 (Fig. 4.1) between 2002-2012, extending observations eight years beyond those reported by *Fricker et al.* (2005). We expand the dataset spatially by observing three other rifts along the front. Two rifts formed at the western edge of the Amery, approximately 10 km apart (W1 and W2), which propagate roughly transverse-to-flow; the third formed in the eastern front (E3), is notably different from the others as it meanders among previously-existing fractures in the area (Fig. 4.1) and is oriented roughly transverse-to-flow.

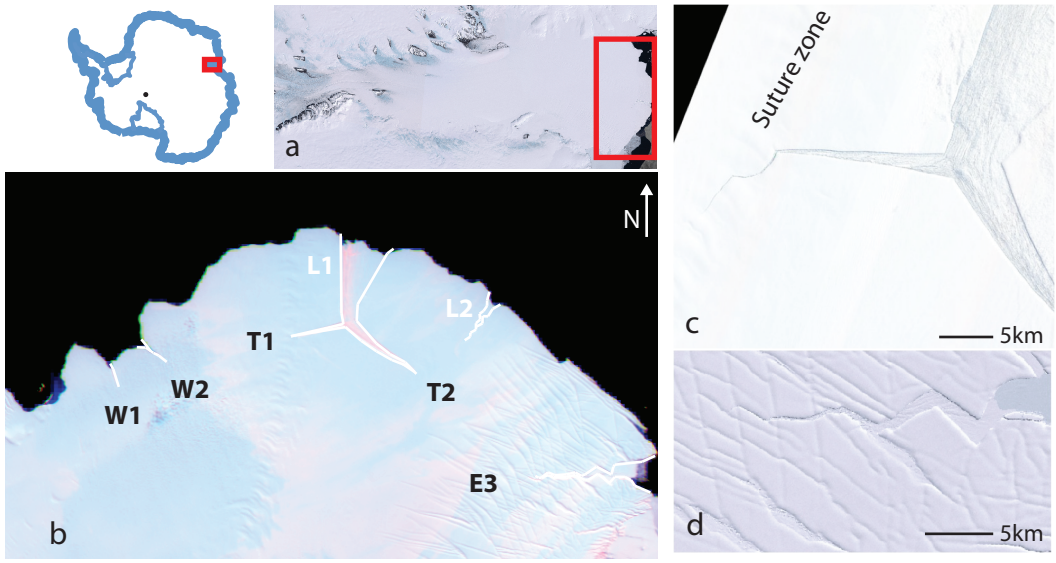

Figure 4.1: False-color MISR (Multi-angle Imaging SpectroRadiometer) images acquired 07 January 2010 show the full Amery Ice Shelf (a) and a zoomed-view of the ice shelf front (b). The five rifts monitored in this study are labeled in black (white trace). (c) A zoomed view of rift T1 acquired 27 January 2012 shows its changing propagation direction as it crosses a suture zone in the ice shelf. (d) A zoomed view of rift E3 acquired 17 November 2002 shows its meandering path among pre-existing crevasses near the ice front.

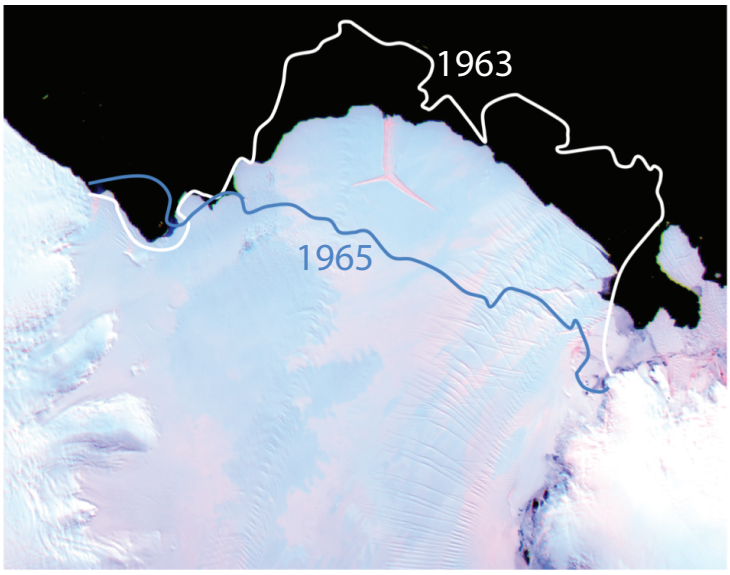

Figure 4.2: The Amery's front positions from Fricker et al. (2002) from 1963 and 1965, framing the last major calving event of the Amery in late 1963/early 1964, are juxtaposed onto a MISR image showing its current front position.

4.3 Data and Methods

4.3.1 Satellite imagery

We collected available satellite imagery of the Amery Ice Shelf between January 2002 and March 2012 from the MISR instrument on NASA's Terra spacecraft (data available from the Atmospheric Sciences Data Center (ASDC) at NASA's Langley Research Center) and the MODIS instrument onboard the Terra and Aqua spacecrafts. We first determined usable images from browse data, requiring that (a) the ice front was sunlit and (b) the images were mostly free of cloud cover. We then downloaded a raw image file for each suitable day for further processing.

4.3.2 Image processing and analysis

We obtained visible channel imagery from the MODIS instrument from the NSIDC (*Scambos et al.*, 1996). Alternatively, the MISR instrument is made up of nine digital cameras—configured so that one camera points toward nadir and the others provide successive aftward and forward views of the Earth's surface—each of which gather image data in four spectral bands (blue, green, red, and near-infrared) (e.g. *Diner et al.*, 2005). To complete analysis of MISR imagery, we acquired data files from the CA (blue), AN (green), and CF (red) camera bands and created false-color images using the publicly-available MISRView software prior to image analysis. The false-color images enhance visibility of the rifts as a result of MISR's multiple camera look angles. False color acts as a proxy for reflectance variations from which we can infer changes in surface texture, and improve upon the visibility of the rifts (*Fricker et al.*, 2005; *Walker et al.*, submitteda). We performed toning, brightening, and contrast-stretching to enhance the visibility of the rifts and increase our ability to differentiate between the rift and background ice.

We measured rifts relative to the same point in the ice shelf to account for ice

advection. Rifts stemming from the edge of the ice front were measured from the upstream rift wall edge to the rift tip; those stemming from the triple junction (T1 and T2) were measured from the center of the triple junction to the rift tips. We defined "rift tip" as the point at which a rift pixel was discernible, i.e., the point in the image where the rift occupied enough of a pixel to provide contrast with the background. We estimate the uncertainty in identifying this point to be one pixel (250m for MODIS, 275m for MISR). Although it may not represent the true rift tip, which may be narrower than a single pixel, our approach provided a systematic method of observing how the rift extended over time. Dependent upon cloud cover in available images, temporal sampling of imagery varied, with gaps ranging between two days (Terra spacecraft revisit time) and up to 48 days. However, on average, usable images were available every nine days during the Austral summer.

4.4 Results

4.4.1 Average rift propagation rates

All of the rifts that we monitored in the Amery Ice Shelf system lengthened throughout the observation period (Fig. 4.3). There were, however, significant differences in the rates of propagation. Overall, the three rifts propagating eastward, W1, W2, and T2, had lower average rates than the two west-propagating rifts, T1 and E3 (Fig. 4.3).

The two west-propagating rifts, T1 and E3, had the greatest overall changes in length. T1 increased from 3.8km to 17.3km and E3 increased from 28.8km to 40.8km. This translates into an average rate of propagation for T1 of 3.8$\pm$ 0.07 m day^{-1} and 3.2$\pm$ 0.07 m day^{-1} for rift E3. These rates are similar to the average rate found by *Fricker et al.* (2005) of 4 m day^{-1} for T1 (2000-2004). These rifts both changed direction at least twice over the decade. (Fig. 4.1(c-d)).

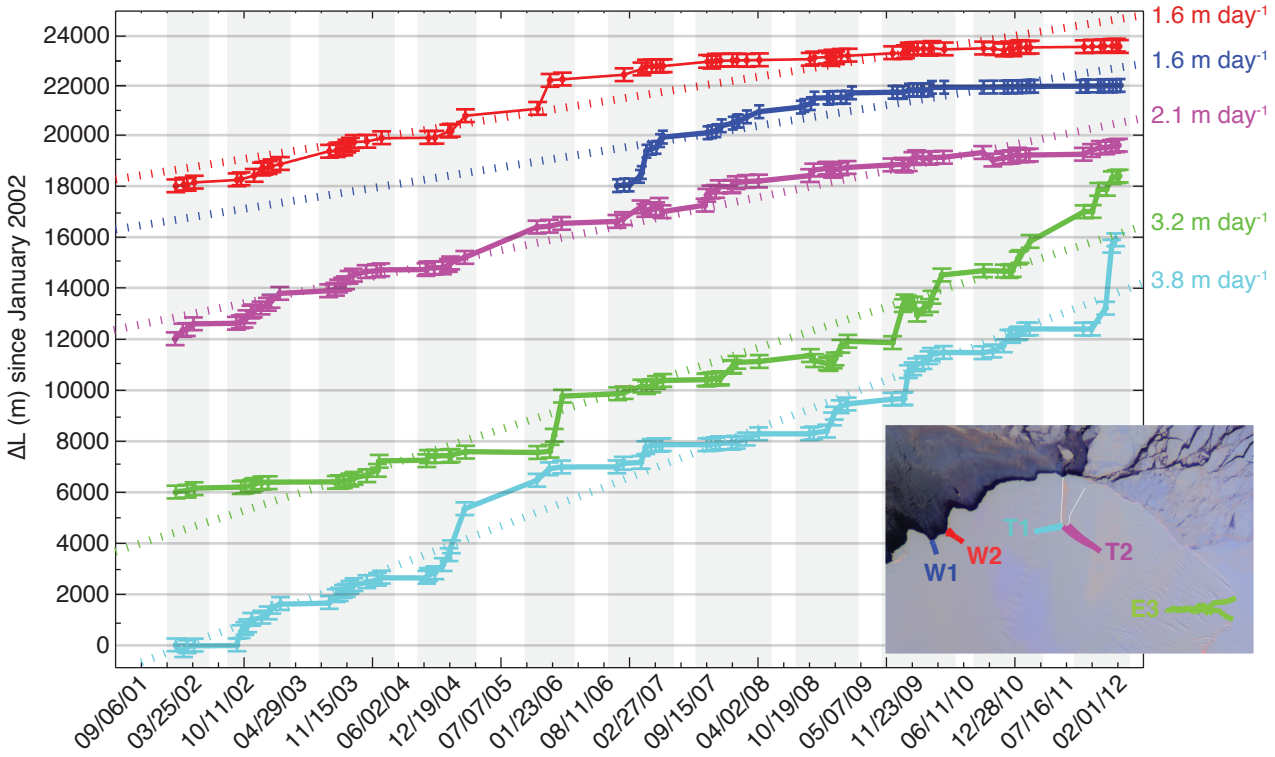

Figure 4.3: The relative change in length for each rift illustrates the general trend that all rifts lengthened over the decade. Gray regions indicate the seasons observed, and dotted lines highlight decadal averages for rift propagation (shown at right). Rift positions are shown (map, inset).

Since January 2002, rift T2 lengthened by 5 km (from an initial length of approximately 14.2 km) at an average rate of 2.1 $\pm$ 0.07 m day^{-1}. This is about half the rate found by *Fricker et al.* (2005) for T2 between 2000-2004. Rift W2 lengthened by approximately 4 km (starting from a length of 4.2 km in January 2002) at an average rate of 1.6$\pm$ 0.07 m day^{-1}. Rift W1, which became visible in October 2006, grew approximately 4 km over the subsequent 5.5 years at an average rate of 1.6$\pm$ 0.13 m day^{-1}.

4.4.2 Seasonal variability

Lack of sunlight during the Austral winter limited our time series to observations between October and April. However, the length of the rift at the end of each Austral summer season was similar to the length at the beginning of the following season (Fig. 4.4), indicating that rift propagation primarily occurs during the summer with negligible propagation during the winter most years. There are, however, two exceptions to this trend. Rifts W2, T1 and T2 all lengthened significantly during the winter of 2005 and rift lengthened during the winter of 2011 (Fig. 4.4).

4.4.3 Evidence for linked activity between rifts

While some rifts' propagation rates have decreased over time (e.g., W1 and W2 have slowed significantly, averaging about 0.2 m day^{-1} after 2010, from approximately 1.8 m day^{-1} in prior years) and others continue to sporadically make large jumps in size (e.g., T1 and E3), all five rifts were still active at the end of the study period. Further investigating the variability of individual propagation events among the rifts, we examined the correlation coefficient between rift pairs. This correlation coefficient quantifies the synchronicity in changes in rift propagation rate between any two pairs of rifts. A higher correlation coefficient suggested that a given pair of rifts propagated in tandem. Rifts that propagated in tandem may respond to a common stimulus

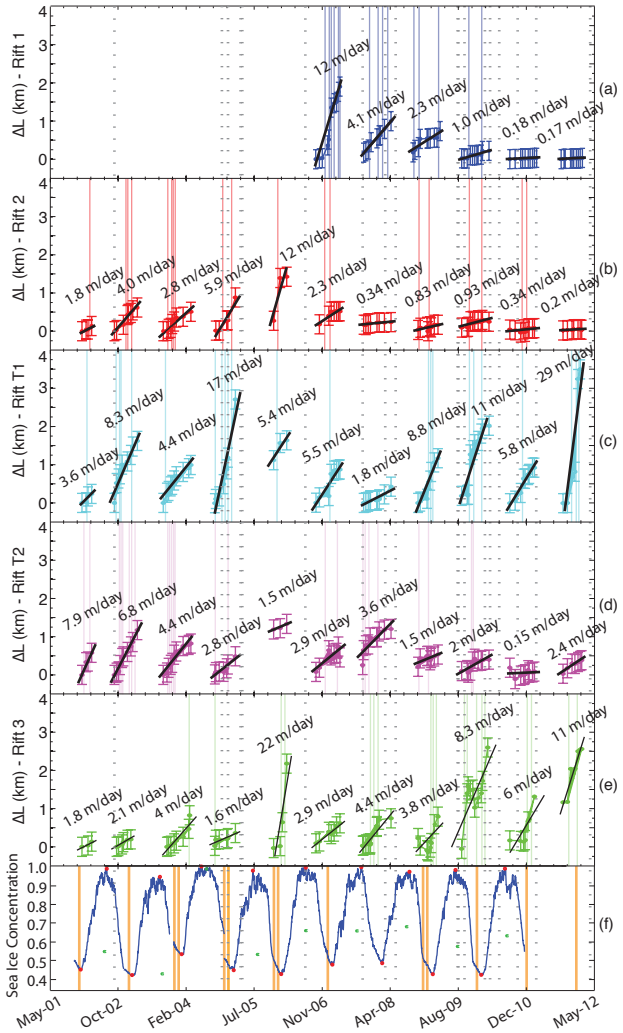

Figure 4.4: Panels (a) through (e) show change in rift length per season. Length changes over the winter are calculated relative to the length at the end of the previous season. Vertical lines in matching color mark propagation events that are outside of the inter-quartile range of the data. Black lines show average propagation rate per season. Panel (f) shows sea ice concentration (blue) and yearly sea ice maxima and minima (red) in front of the Amery; orange lines denote months in which average atmospheric temperature surpassed 0 °C as measured from Mawson and Davis stations. Dotted gray vertical lines denote occurrences of Indian Ocean tsunamis that reached the Amery over the decade.

(or stimuli); alternately, a negative correlation coefficient corresponded to rifts that traded off, a situation in which one rift potentially relieved stress from another.

Since rift W1 initiated in 2006, about halfway through the observation period, we analyzed the correlation between rift pairs by breaking the time series into two shorter periods: in the first, from 2002 until April 2006, we monitored just rifts W2, T1, T2, and E3 (Fig. 4.5, left panels). In the second period, from October 2006 until April 2012, we monitored all five rifts (Fig. 4.5, right panels). Between 2002-2006, the pair with the highest positive correlation was that of W2 and T1, closely followed by T1 and T2. After the initiation of W1 in 2006, these relationships changed, and between the years 2006-2012 W1 and W2 shared the highest correlation, followed by W2 and T1 (the former highest-correlated pair), whose correlation decreased by approximately half. The correlation coefficient between T1 and T2 also significantly changed, to where there was nearly-zero correlation in the second period.

The relationship between W2 and T2 did not change significantly between the two periods and stayed relatively close to zero. The negative correlation between W2 and E3 decreased in the later years towards zero while E3's correlation with W1 became increasingly negative, which is consistent given the geometry of these three rifts: prior to winter 2006, W2 and E3 were the rifts closest to the eastern and western margins of the ice shelf, respectively. Beginning in October 2006, W1 effectively replaced W2 in the western-most margin trade-off position. Overall, correlation coefficients for the original four rifts decreased in magnitude after the addition of W1, with the exception of T1 and E3 (the only west-propagating pair). The change in nearly every pair of rifts between the two time periods showcased the effects of introducing a new rift into the system; rift W1 changed the interaction of the previously-existing four rifts.

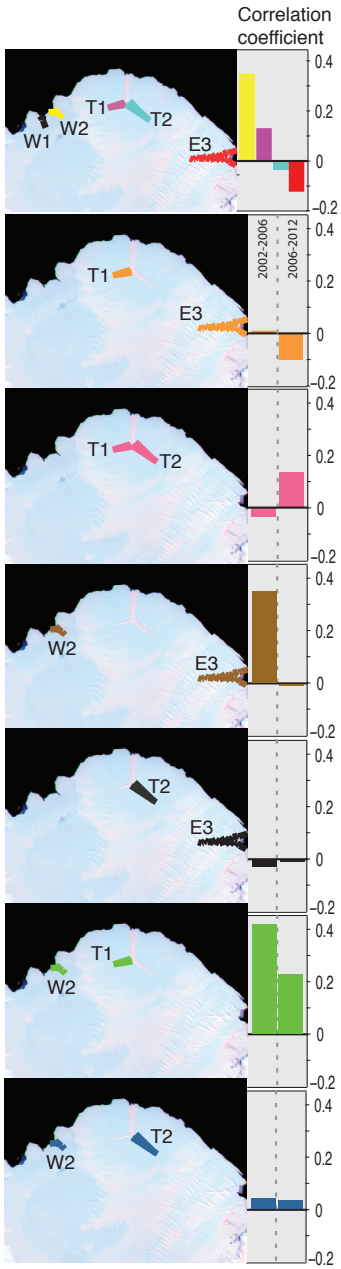

Figure 4.5: The correlation of movement between specified rift pairs shows whether pairs propagate in tandem or are offset from each other. The left panel shows relationships between the pairs between 2002-2006; the right panel shows the altered relationships between rift pairs in the years following the initiation of W1 in 2006. The center panel shows the combined correlation coefficients over the decade.

4.4.4 Large propagation events

We investigated the role of intermittent "large propagation events", which we define as propagation events with magnitudes larger than the inter-quartile range of the data (Fig. 4.4). For most seasons, large rifting events more often occurred in December and January than in October and November. Large propagation events were determined individually for each rift (Fig. 4.4). While infrequent, the occurrence of a small number of large propagation events dominate the seasonal averages. Moreover, the number of large events for the east-propagating rifts declined significantly by the beginning of the 2010. The absence of most large events in either W1 or W2 after January 2010 coincides with their near-arrest in subsequent seasons. Rifts T1 and E3, however, continued to experience large sporadic propagation events throughout the decade, which coincided with the changes we observed in their directions of propagation.

Rifts E3 and T1 were observed to propagate in regions with visible surface features in the satellite images (Fig. 4.1(c-d)). T1 propagated westward, transverse-to-flow, until January 2009 when it intersected a suture zone in the shelf, which formed where two ice streams merged upstream (*Fricker et al.*, 2002; *Bassis et al.*, 2007). It changed direction twice before exiting the suture zone in December 2011 and has continued to propagate longitudinal-to-flow since then. These changes in direction were both associated with large propagation events that averaged 63 m day^{-1} and 18 m day^{-1} respectively. Similarly, E3 lies in an area of the shelf that contains a system of crevasses, along which E3 meanders. Since January 2002, it has changed direction six times. Almost all of these direction changes occurred after 2007, a trend that correlates with the clear increase in propagation events for E3 after 2007 (Fig. 4.4).

4.4.5 Atmosphere and ocean forcing

Previous studies have implicated above freezing atmospheric temperatures, changes in sea ice concentration and the effect of tsunamis impinging on the calving front as triggers of rift propagation. We examine whether we can attribute the variability in rift propagation rates and/or large propagation events are triggered by any these variables next.

4.4.5.1 Atmospheric temperatures

We acquired monthly-averaged air temperature data recorded by automatic weather stations at Davis and Mawson Stations (Fig. 4.4(f)). The Amery Ice Shelf ice front is located between these stations, farther north than Davis and farther south than Mawson. Summer temperatures generally remained below 0°C, and averaged -4°C. There were a few instances in which monthly averages rose above freezing in December and/or January. The maximum monthly average was approximately 2.5°C at Davis in December 2005 and again in January 2010. Large propagation events appeared in both rifts W2 and E3 in December 2005; following January 2010's high temperatures, rift E3 experienced a propagation event, although this event was not classified as a large event (Fig. 4.4). Aside from these well-correlated instances, the pattern of propagation events following the warmest months is not observed consistently. Correlation between above-0°C monthly averages and subsequent rift propagation occurs less than half of the time (approximately 40% of the time in rifts W2 and T1, 30% in W1 and W3, and 15% of the time in T2). It may be possible that the effect of atmospheric temperature is negligible except when paired with other factors; as suggested by *Bassis et al.* (2008), it may exert more influence as the point at which an iceberg calves approaches. However, at this time, the Amery Ice Shelf is still relatively cold and it does not appear to be significantly affected by surface melting.

4.4.5.2 Sea ice and ocean influence

Ocean swell can be dampened by the presence of sea ice in front of the shelf (e.g. *Bassis et al.*, 2008). Therefore, as a proxy for short period ocean swell, we compared the monthly sea ice concentration in front of the Amery Ice Shelf to our rift propagation data (Fig. 4.4(f)) (long period ocean swell is less affected by sea ice, but there is also much less wave energy at these wavelengths.). The sea ice data were retrieved from monthly Nimbus-7 SMMR and DMSP SSM/I-SSMIS passive microwave data (*Cavalieri et al.*, 1996). There was little change in rift length over the winters (Fig. 4.3), when sea ice concentration was at a maximum. In the summer, rift propagation increased as sea ice concentration decreases, thereby showing a seasonal anti-correlation pattern. We further investigated the influence of sea ice by comparing annual averages seasonally averaged sea ice concentration with seasonally averaged rift propagation to determine whether or not a decrease in sea ice could explain some of the more extreme propagation events or variation in rates between years. If sea ice concentration controlled the propagation of rifts, we would expect that years with higher average concentration to correlate with slower annual propagation rates in the ice shelf, and vice versa. However, although sea ice concentration after 2005 remained relatively stable, rifts continued to propagate at high speed, especially rifts T1, T2, and E3. We also examined the maxima and minima of each season. In this scenario, we looked for significant propagation events that followed periods of minimal sea ice, and conversely for little rift motion during periods of high sea ice. However, we did not observe this pattern, and find little evidence that variations in sea ice concentration are controlling rift propagation. This suggests that short-period ocean swell is also not responsible for rift propagation. We have no direct observations of longer period infra-gravity waves and cannot rule out a mechanical interaction with these waves.

4.4.5.3 Effects of forcing by tsunamis

The effect of tsunamis on front-initiated ice shelf rifts was documented by *Walker et al.* (submitteda), who showed that tsunami arrivals around the Antarctic continent correlated with large rift propagation events or iceberg calving events throughout the decade (2002-2012). These included events in the Filchner, Larsen C, Abbott, Ross, Shackleton, and Fimbul ice shelves; *Brunt et al.* (2011) showed that the 2011 Honshu tsunami likely caused the separation of an iceberg from Sulzberger Ice Shelf following wave arrival there. We compared our rift propagation record with the occurrences of tsunamis capable of producing runup in the Amery Ice Shelf region (data available from the Historical Tsunami Database maintained by NOAA National Geophysical Data Center) (Fig. 4.4). The four rifts present in 2004 were affected by the tsunami associated with the December 2004 Sumatra earthquake, with significant increases in length following the event (between 26 December 2004 and 9 January 2005) (*Walker et al.*, submitteda). In contrast to *Bassis et al.* (2008) who argued that the correlation between rift propagation and the arrival of the tsunami may have been coincidental, we found that four of the rifts propagated after the arrival of the tsunami providing a stronger correlation. Moreover, we found eight examples in which one or more rift propagated following the arrivals of other tsunamis (Fig. 4.4). Furthermore, the abnormal winter propagation event we observed in winter of 2005, is coincident with the predicted impact of a tsunami during the austral winter suggesting that these events may have also been triggered by the arrival of a tsunami.

4.5 Discussion

Our observations show that rift propagation on the Amery Ice Shelf is highly variable with complex spatial and temporal patterns. The spatial pattern of rift propagation and changing relationship between rift pairs suggests that mechanical

rift interaction between rifts is an important component of the variability in rift propagation rate. The initiation and propagation of a nearby rift changes the state of stress in the shelf on the whole and how other rifts respond to it. Our observations also reinforce previous studies (*Bassis et al.*, 2005, 2008) and show that variability in rift propagation is not caused by changes in atmospheric temperature or sea ice concentrations. We did find, however, that many of the large propagations events we observed followed the projected arrival of tsunamis in the region. This correlation has been noted for rifts in other ice shelves (*Brunt et al.*, 2011; *Walker et al.*, submitteda), but appears to be more pronounced for the Amery Ice Shelf rifts.

We postulate that the reason that the Amery Ice Shelf rifts are sensitive to tsunamis is because they are front-initiated and open to the ocean. Most rifts observed on the other Antarctic ice shelves initiated upstream from the calving front, transverse to the direction of flow and advect downstream as the ice flows towards toward the ocean. The rifts in the Amery Ice Shelf, in contrast, initiated from the front and propagated inwards, and are directly open to the ocean. Tsunamis induce small changes in wave height (e.g., 15-30 cm wave amplitude in front of the Amery Ice Shelf following the 26 December 2004 Sumatra earthquake) and have long wavelengths, but as the low-amplitude wave penetrates into the relatively narrow rift, it builds up an increased pressure at the rift tip that is higher than normal (*Muller et al.*, 2000, 2002; *Wolters and Muller*, 2004; *Walker et al.*, submitteda). Additionally, as the tsunami wave reflects back off the rift walls and sweeps back out of the rift, it may remove debris, decreasing the amount of mélange filling the rift and thereby the stress at the rift tip (*Cox and Cooker*, 2001).

Our observations also suggest that structural heterogeneity within the shelf appears to influence rift propagation (rate and direction). Pre-existing crevasses create an area of less resistance in which a rift can propagate more easily due to differences in ice properties from the adjacent ice. The observed large jump in rift T1 over the

winter of 2002 occurred after the rift intersected with a pre-existing crevasse (*Fricker et al.*, 2005). The role of crevasses is also evident in the meandering pattern of Rift E3, which formed in an area of the shelf with an intense system of crevasses. Since January 2002, it has changed direction six times. Almost all of these direction changes occurred after 2007, which correlates with the clear increases in propagation events after 2007. Similarly, Rift T1 propagated westward, transverse-to-flow, until it intersected a suture zone in the ice shelf. The rate of propagation slowed down and the rift changed direction twice before exiting the suture zone in December 2011. The two changes in direction were associated with large propagation events that averaged 63 m day^{-1} and 18 m day^{-1}, respectively.

Surprisingly, although pre-existing crevasses can modulate the propagation of rifts, the active rifts in the Amery Ice Shelf do not stem from pre-existing crevasses that have advected downstream; instead they are front-initiated. Fractures that advected from upstream were notably inactive over the decade, with the exception of the meandering propagation of rift E3 through a crevasse field. Once crevasses or rifts stagnate, they are not easily re-activated, despite their position near or at the ice front.

We suggest that the formation of front initiated rifts is a consequence of the thinning as it approaches its most extended position prior to its last large calving event in 1963/64. This front-initiated setting, which was a setting observed for only a few other rifts around Antarctica (*Walker et al.*, submitteda), along with intense surface crevassing (and possibly basal crevassing) is the reason why the Amery rift system is so much more active that rift systems elsewhere and is also why these rifts are so more sensitive to perturbations from environmental forcings like tsunamis.

4.6 Conclusions

We have monitored five rifts at the front of the Amery Ice Shelf using MISR and MODIS satellite imagery, and have created a decadal record of propagation. While

all five rifts lengthened over the observation period, the three east-propagating rifts have slowed significantly since 2010, while the remaining two west-propagating rifts continue to propagate at higher rates. Their average rates for the period differed, but they also varied annually and exhibited a seasonal pattern with most propagation occurring during the austral summer.

Comparison with atmospheric temperatures and sea-ice concentration suggests that internal glaciological stress is the primary drivers behind the propagation of the rifts, consistent with previous studies. As the Amery approaches its 1963/64 calving position, it is becoming increasingly unstable as it tears itself apart. We suggest that propagation of rifts at the Amery is also augmented by both structural heterogeneity within the shelf and the existence of an interacting system of rifts, which has created a more complicated stress field than would likely exist surrounding a single isolated rift. These five rifts are also unusual in that they initiated and extend from the shelf front, rather than initiating upstream, like most other rifts observed on Antarctic ice shelves (e.g. *Walker et al.*, submitteda). Their precarious position and the observation that Amery seems poised for a large calving event may make the rifts increasingly sensitive to the effects of tsunamis. The fact that structural heterogeneity, internal glaciological stress due to shelf geometry, and intermittent tectonic events (by way of tsunamis) contribute to the propagation of rifts and that the rifts exhibit interactive behavior suggests that these parameters should be considered in the modeling of rift propagation in ice shelves. By continuing to observe the rifts, in the future it may be possible to connect rifting activity levels to the imminence or likelihood of large calving events.

CHAPTER V

Propagation of Closely-spaced Fractures in a Planetary Ice Shell

5.1 Introduction

Recent observations have revealed that liquid water and other trace chemicals may be erupting onto the surfaces of icy satellites (e.g. *Miyamoto et al.*, 2005; *Prockter and Schenk*, 2005). A prominent example of this is the liquid water escaping at the south pole of Enceladus from a set of fractures called the "tiger stripes" (*Porco et al.*, 2006). From Cassini's first observations of the moon in 2005, it was inferred that the plumes were erupting from above a high-heat anomaly concentrated at the south pole (e.g. *Spencer et al.*, 2008). all along the fractures (*Porco et al.*, 2006). Following the discovery of the jets, dedicated flybys of Enceladus were planned for later in the mission and upon closer approach, it has recently been discovered that the water is escaping from 98 individual jets located along the four parallel tiger stripe fractures (*Porco et al.*, 2013). Unlike Enceladus, active eruption of subsurface water in the form of geysers has not been observed. However, there are features that indicate that Europa may have been (or may still be) erupting subsurface water in a manner similar to magma flows on the Earth (cryo-volcanism) (e.g. *Fagents*, 2003). There are a few different feature types on Europa that have been associated with effusive

cryovolcanism as a possible origin, including lobate flows, circular lenticulae, chaos regions, and low-lying, smooth surfaces (e.g. *Kargel*, 1995). In both cases of extrusive and effusive release of water (or a mixed solution of subsurface materials called "cryo-magma"), a conduit must exist between a subsurface reservoir and the surface. The surfaces of the satellites are riddled with cracks, and those that penetrate the entire thickness of the shell may serve as these conduits connecting the subsurface to the surface.

Previous studies have focused on determining conditions in which surface-initiated fractures can penetrate through the entire ice shell. To do so, variations of linear elastic fracture mechanics models (LEFM) have been used to determine the depth to which vertical fractures can penetrate (e.g. *Lee et al.*, 2005; *Qin et al.*, 2007; *Rudolph and Manga*, 2009). Using LEFM and accounting for variable porosity, it was shown by *Lee et al.* (2005) and *Qin et al.* (2007), that a single-layered 1 km brittle Europan ice shell could be fully-fractured with tensile stresses greater than 200 kPa. It was later shown by *Rudolph and Manga* (2009) that a Europan ice shell less than 5 km could be completely fractured under 3 MPa of tensile stress and a 30 km Enceladus ice shell could be completely fractured under 3 MPa of tensile stress when a brittle layer overlies a ductile layer (however, these results were based on the assumption that the tensile strength of the ice was equal to the tensile stress applied in the upper brittle layer). Model results are highly dependent upon assumptions.

Aside from the tensile strength, porosity profile, and layer structure, determination of fracture penetration depth using LEFM also depends on an assumption of ice shell thickness. Such estimates for the shell thicknesses of Enceladus and Europa are uncertain (e.g. *Billings and Kattenhorn*, 2005; *Porco et al.*, 2006; *Schubert et al.*, 2007). Estimates of Europa's ice shell thickness range between 1 and 30 km for the layer that behaves elastically and can be described by LEFM (e.g. *Nimmo et al.*, 2003; *Billings and Kattenhorn*, 2005; *Lee et al.*, 2005; *Rudolph and Manga*, 2009).

Estimates of the elastic shell thickness at Enceladus encompass the range of 10-90 km (*Schubert et al.*, 2007; *Rudolph and Manga*, 2009), but estimates on the thinner end of the spectrum ($\leq$40 km) are favored in models of the formation of the South Polar Terrain and shear failure of the tiger stripe fractures (*Nimmo et al.*, 2007; *Smith-Konter and Pappalardo*, 2008; *Olgin et al.*, 2011; *Walker et al.*, 2012).

Additionally, estimates of fracture penetration depth also depend on the magnitude of the tensile stresses applied. Estimates from a variety of sources of tensile stress at the icy moons include the diurnally-varying tidal stress to which the shells are exposed throughout their orbits. At Europa, due to its Laplace resonant orbit, these stresses are on the order of 0.1 MPa (*Hurford et al.*, 2007b). At Enceladus, due to an orbital eccentricity of 0.0047, tidal stress is also on the order of 0.1 MPa. Another contributor to tensile stress that acts upon the shells is the cooling of icy material at the base of the shells, which may induce extensional stresses in the upper part of the shell on the order of 10 MPa in shells greater than 10 km thick (*Nimmo*, 2004). These stresses, however, are likely reduced to less than 3 MPa for Europa and 1-10 MPa for Enceladus, depending on thickness changes, when compressibility of the subsurface ocean is included. Europa may have been in a state of non-synchronous rotation (*Leith and McKinnon*, 1996) or undergone true polar wander earlier in its evolution (*Schenk et al.*, 2008). In these cases, induced tensional stresses would be of the order of 1-10 MPa. At Enceladus, *Nimmo and Schenk* (2006) suggested that diapir-induced re-orientation of the shell may have induced tensile stresses on the order of 10 MPa. Additionally, *Patthoff and Kattenhorn* (2011) highlighted features at the south pole that suggest non-synchronous rotation of the shell, and determined the stresses induced by this process are between 1-5 MPa.

We approach the problem of crack propagation in the icy shells using a LEFM model, but consider the fact that the shells are extensively fractured, and linear fracture formations are often closely-spaced. Most previous studies have focused

exclusively on the penetration of surface fractures because it is believed that warmer ductile ice at the base is too viscous to fail brittely (e.g. *Lee et al.*, 2005). However, terrestrial observations show intense basal crevassing of Antarctic ice shelves. The bases of these freely-floating bodies of ice are close to the pressure melting point, despite the fact that they flow viscously. Because of this, we also consider fractures that initiate from the bottom of the ice shell and become filled with water. We show that whether initiated from the surface or bottom of the shell, multiple fractures interact, and that the tensile stress may need to exceed previous estimates by an order of magnitude to allow fractures to penetrate the entire ice thickness. This is supported by observations of terrestrial ice (*Weertman*, 1973; *van der Veen*, 1998a) and other materials containing fracture arrays (*Cowles et al.*, 1985; *Parker*, 1998; *Myer*, 2000).

5.2 Crack propagation model

Linear elastic fracture mechanics (LEFM) is a simplified approach that can be used to model the propagation of an initial crack or flaw from the surface or bottom of an elastic ice layer. A value used in LEFM to determine the propagation of an initial crack under certain conditions is the stress intensity factor, K_Σ. When K_Σ surpasses a critical value K_{IC} the critical stress intensity factor, then the fracture will propagate. The critical stress intensity most often used for terrestrial ice is 0.15 MPa $m^{1/2}$, but we use a range of 0.1 - 0.4 MPa $m^{1/2}$, consistent with previous studies. When a crack initiates at the surface, an estimate for the depth to which it will propagate can be obtained by finding the depth at which the net stress intensity factor is equal to the critical stress intensity factor, $K_I = K_{IC}$. To determine whether or not tensile stresses in the crust cause stress concentration at the crack tip to surpass the critical stress intensity, the stress intensity factor is decomposed into contribution due to the depth-independent tensile stress $K_I^{(1)}$ and depth-dependent overburden pressure $K_I^{(2)}$.

5.2.1 Stress intensity due to tensile stress

The depth-independent tensile stress intensity at the crack tip ($K_I^{(1)}$) can be expressed as:

$$K_I^{(1)} = F(\lambda)\sigma_T\sqrt{\pi d} \tag{5.1}$$

where σ_T is the far field tensile stress within the shell, λ is the ratio of fracture depth d to thickness H, d/H, and $F(\lambda)$ is a non-linear function of this ratio given by *Tada et al.* (2000) as

$$F(\lambda) = 1.12 - 0.23\lambda + 10.55\lambda^2 - 21.72\lambda^3 + 30.39\lambda^4, \tag{5.2}$$

where H is the thickness of the brittle top layer (e.g. *Lee et al.*, 2005; *Collins et al.*, 2009). As $\lambda \to 0$, $K_I^{(1)}$ approximates the expression by *Weertman* (1973) and *Smith* (1976, 1978) for propagation in an infinite half-space, $K_I^{(1)} \approx 1.12\sigma_T\sqrt{\pi d}$. The difference between the infinite half-space model and the model that includes the non-linear function (i.e., Eq. 5.2) is that the former was shown by *Lee et al.* (2005) to underestimate the depth to which a fracture would penetrate by between a third to a half of the depths predicted by Eq. 5.2.

5.2.2 Stress intensity due to overburden stress

Large-scale tensile stress in the crust is counterbalanced by the lithostatic overburden stress, which acts to close the fracture through compression. Lithostatic overburden stress L varies linearly with depth if it is assumed that ice density ρ_i is constant (e.g. *Weertman*, 1973; *Smith*, 1976; *van der Veen*, 1998a), where

$$L = -\rho_i g b \tag{5.3}$$

where b represents the depth below the surface. However, ice comprising the shells at the icy moons is much more porous in the near surface layers than it is in the bottom layers of the shell (*Nimmo et al.*, 2003). A porosity profile determined by *Nimmo et al.* (2003) estimated that higher porosities can persist through the upper half of the elastic layer, before going to 0 in the lower half of the shell. We consider that h_p is the depth to the transition between porous upper section and condensed lower section, and augment the linear expression for overburden stress given by *Weertman* (1973) and *Smith* (1976, 1978) above to include terms to account for the change in layer properties. In the *Black et al.* (2001a) model, porosity is given by:

$$v_b = \int_{r_0}^{r_m} \frac{4\pi}{3} \kappa r_a^{3-\vartheta} dr \tag{5.4}$$

where r_a is the radius of the pores (and r_0 and r_m are the minimum and maximum pore sizes), κ is a constant and ϑ is a scaling value found in *Black et al.* (2001a,b). The modified stress intensity due to overburden stress (K_I^2) in a shell with a porous upper layer is expressed as (*Lee et al.*, 2005):

$$\begin{aligned} K_I^{(2)} &= -0.683\rho_i(1-v_b)gd\sqrt{\pi d} && (5.5)\\ &\quad -u(d-h_p)\frac{2d\sqrt{d}}{\sqrt{\pi}}\rho_i v_b g && (5.6)\\ &\quad \times \int_{\sin^{-1}(h_p/d)}^{\pi/2} \left(\sin\theta - \frac{h_p}{d}\right) && (5.7)\\ &\quad \times (1.3 - 0.3(\sin\theta)^{5/4}) d\theta && (5.8) \end{aligned}$$

where $u(d-h_p)$ is a step-function to differentiate between the porosity above and below h_p.

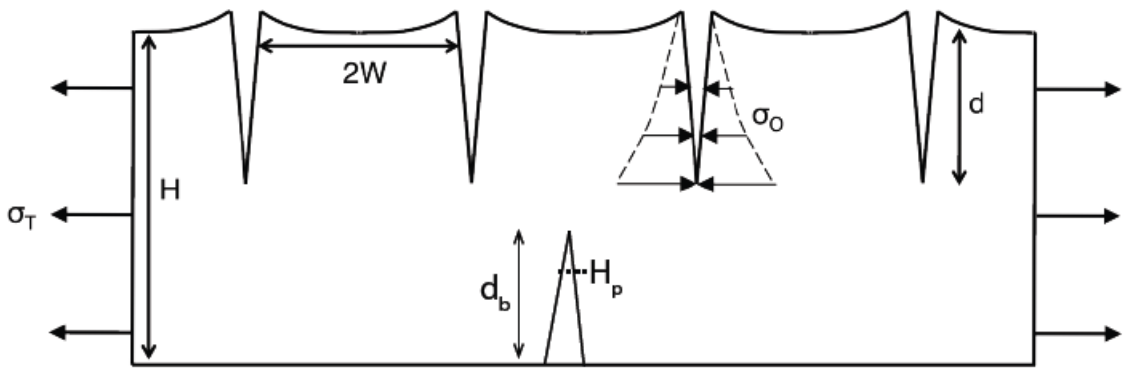

Figure 5.1: Free-body diagram of multiple cracks in a region of ice. σ_O is the overburden stress which increases with depth. σ_T is the tensile stress acting on the brittle layer of thickness H, initiating cracks of depth d, which are spaced 2W apart.

5.2.3 Stress intensity modification by multiple fractures

Neighboring fractures affect the field of elastic stresses concentrated near the crack tip (Fig. 5.1). In this case, the stress intensity factor due to tensile stress in the highly fractured medium is modified from Eq. 5.1 and expressed as (*Benthem and Koiter*, 1973):

$$K_I^{(1,m)} = D(S)\sigma_T\sqrt{\pi dS} \tag{5.9}$$

Here, $D(S)$is a depth-independent function of S, which is a ratio of crack spacing W to crack depth,

$$S = \frac{W}{W+d} \tag{5.10}$$

and as in *Cowles et al.* (1985)

$$\begin{aligned} D(S) &= \frac{F(\lambda)}{\sqrt{\pi}}(1+\frac{1}{2}S+\frac{3}{8}S^2+\frac{5}{16}S^3+\frac{35}{128}S^4 && (5.11)\\ &\quad +\frac{63}{256}S^5+\frac{231}{1024}S^6)+22.501S^7 && (5.12)\\ &\quad -63.502S^8+58.045S^9+17.577S^{10}. && (5.13) \end{aligned}$$

Weertman (1973) showed that when fractures were closely spaced (i.e., spacing of fractures much less than depth of fractures), stress shadowing reduces the stress concentration so that fractures only penetrate to the depth at which the tensile stress vanishes.

$$d_s = \frac{\sigma_T}{\rho_i g}, \tag{5.14}$$

which assumes $K_{IC} = 0$. This relation is known in glaciology as the Nye zero stress model. Observations show that in the absence of information about fracture spacing, the Nye model predicts fracture depth in glaciers better than single LEFM-based models, which tend to over-estimate fracture depths.

5.2.4 Bottom cracks

Another modification to previous models of planetary shell penetration is the consideration of basal fractures. Previous studies doubt their existence (e.g. *Lee et al.*, 2005) and therefore ignored their plausible contribution to delivering ocean water closer to the surface and enhancing the likelihood of full surface fracture penetration. Fractures may form at the base of the shell due to longitudinal stress gradients that over time cause stress corrosion, as observed in both ice and rock settings (*Anderson and Grew*, 1977; *Crawford and Stevenson*, 1988; *Maimon et al.*, 2012). If overlying a subsurface ocean, these basal fractures can become filled with water. Fluid within a crack—in either the multiple or single fracture case—applies water pressure on the crack walls and opposes overburden stress (e.g. *Weertman*, 1973). We can estimate the depth to which these fractures can penetrate in two ways: (1) by LEFM and (2) the limit of closely-spaced fractures (zero-stress model).

The height above the base to which water will rise in a bottom crack of height d_b is called the piezometric head (H_p). In the LEFM case, the water pressure (σ_w) at a

given height z above the base is given by (e.g. *van der Veen*, 1998b)

$$\sigma_w(z) = \rho_w g(H_p - z) \tag{5.15}$$

where ρ_w is the density of water filling the fracture. Water pressure decreases with increasing height z below H_p (z = 0 at the base of the shell). Above H_p, the water pressure is zero. As in the surface fracture case, to calculate the net stress intensity factor, we combine the contributing stresses at the base, which include the water pressure, lithostatic overburden stress, and tensile stress. As in *van der Veen* (1998b) and *Mitri and Showman* (2008), for a basal crevasse the net stress intensity factor is

$$K_I = \int_0^h \frac{2\sigma_n(z)}{\sqrt{\pi h}} G(\gamma, \lambda) dz \tag{5.16}$$

where $\gamma = z/d_b$, $\lambda = d_b/H$, and

$$G(\gamma, \lambda) = \frac{3.52(1-\gamma)}{(1-\lambda)^{3/2}} - \frac{4.35 - 5.28\gamma}{(1-\lambda)^{1/2}} + \left[\frac{1.30 - 0.30\gamma^{3/2}}{(1-\gamma)^{1/2}} + 0.83 - 1.76\gamma\right] \times [1 - (1-\gamma)\lambda]\,. \tag{5.17}$$

Alternately, the zero-stress model accomodates the effect of water infill in basal crevasses by amending Eq. 5.14 to calculate the penetration height of the crevasse as:

$$d_b = \frac{\rho_i}{\rho_w - \rho_i} \left[\frac{\sigma_T}{\rho_i g}\right] \tag{5.18}$$

In most cases the Nye zero-stress model in both the basal and surficial scenarios underestimates the depths predicted by the LEFM approach, but has been observed to more accurately model crevasse depths when compared to actual observations (e.g. *Mottram and Benn*, 2009).

5.3 Model parameters and experimental setup

We considered four different model setups for each ice shell, whose thicknesses were 1 km (Europa) and 30 km (Enceladus) which serve as lower bounds from shell thickness estimates in the literature. In these models we considered porosities of 33% for Europa (*Black et al.*, 2001a; *Lee et al.*, 2005) and 20% for Enceladus (e.g. *Kieffer et al.*, 2006) in the upper half of the elastic layers, and $v_b = 0$ for the section of ice below h_p (bottom half of elastic layer and ductile layer). We first considered a single fracture in each ice shell and modeled the fractional penetration depth (d/H) for a range of tensile stresses (0.2 - 3 MPa) using the LEFM method for a single fracture (Eq. 5.1). Second, we modeled the same fracture under the same tensile stress range, but instead set it among closely-spaced fractures (Eq. 5.9). In the case of Enceladus, we used a crack spacing equal to that observed between the tiger stripe fractures of 35 km (e.g. *Gioia et al.*, 2007). For fracture spacing at Europa, determining a set of nearly-parallel fractures like the tiger stripes is dependent upon the area over which the fracture sets are observed, since its fracture systems are mainly cycloidal arcs. We worked from an example case in Argadnel Regio (trailing hemisphere region). In this region, the space between the segments of the cycloidal fractures was approximately 10% of the observed area. Next, we modeled the propagation of bottom cracks. First, we considered a single bottom crack in each ice shell and assumed that water fully-filled the fracture. Next, we considered a bottom fracture among an array of other bottom fractures, and set the spacing to the same used in the case of multiple surface fractures.

5.4 Results

For both Europa and Enceladus, we found that larger tensile stresses are required to completely fracture the ice shell when multiple fractures are present. In the case

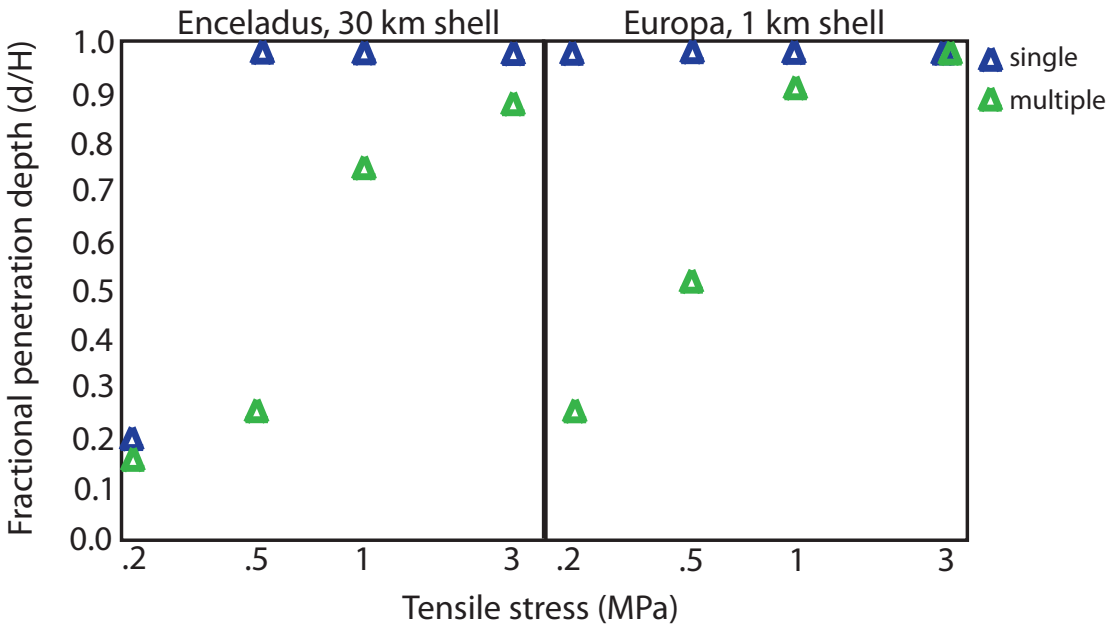

Figure 5.2: Fractional penetration depth (d/H) of surface fractures for a range of tensile stress (0.2-3 MPa) in a 30 km Enceladus shell (left) and a 1 km Europa shell (right). Blue markers signify d/H for a single fracture, green markers signify d/H for a fracture in a fracture array.

of a single crack at Enceladus, a 30 km ice shell was completely fractured under loads greater than 500 kPa. Alternately in the multiple fracture case, the same shell was only completely cracked with a minimum tensile stress of 4.5 MPa (Fig. 5.2). Similarly, for a single fracture at Europa, the shell was completely cracked under loads that exceeded 0.25 MPa. In the case of multiple fractures, this shell was only completely fractured under tensile loads exceeding 1 MPa (Fig. 5.2).

Likewise for basal fractures that are filled by water, larger tensile stresses are required to completely fracture the shell. A single crack in the shell penetrates deeper into the ice than in the multiple fracture case. For a single basal fracture at Enceladus, a tensile stress of 0.2 MPa at the base of the shell drove the propagation of a single water-filled crevasse to a height of 10.8 km through the shell. For multiple basal fractures, the same applied stress allowed for propagation through the ice shell to a height of only 8.9 km (Fig. 5.3). This result was corroborated by the zero-stress model

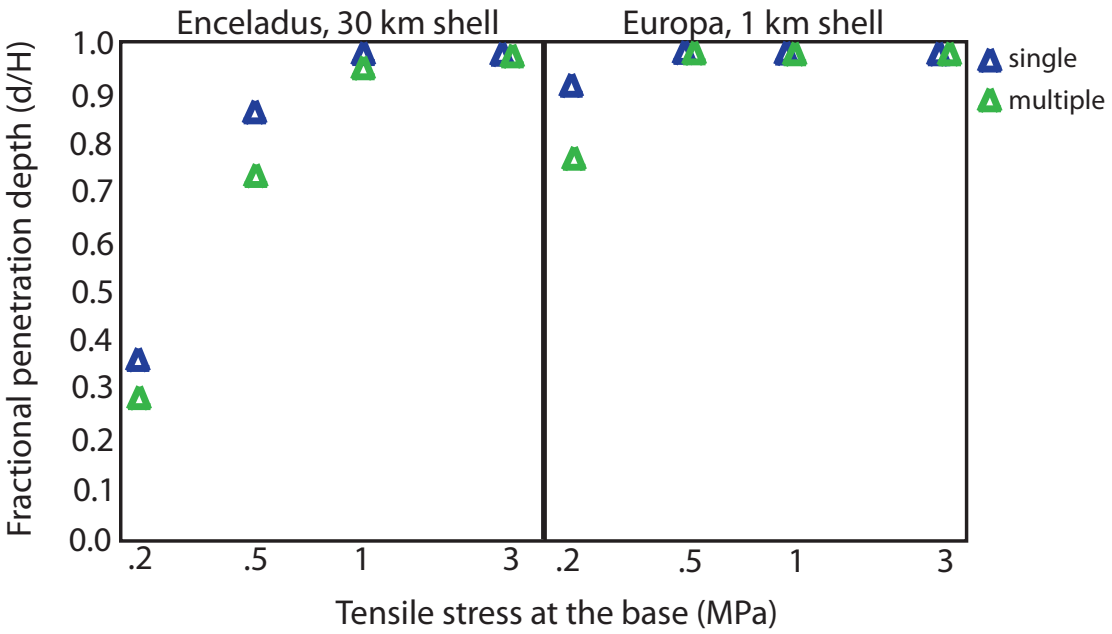

Figure 5.3: Fractional penetration depth (d/H) of basal fractures for a range of tensile stress (0.2-3 MPa) in a 30 km Enceladus shell (left) and a 1 km Europa shell (right). Blue markers signify d/H for a single fracture, green markers signify d/H for a fracture in a fracture array.

resulting in a predicted penetration height of 9.4 km. At Europa, under a 0.2 MPa tensile stress, a single water-filled crevasse reached 940 m in height through the shell. In the case that Europa's ice shell is actually $\leq$1 km, such a model would predict the total rupture of the shell. In the case of multiple basal fractures at Europa, a basal tensile stress of 0.2 MPa would cause propagation up to a height of 770 m into the ice shell. We note that the zero-stress model predicted a penetration height of 790 m.

5.5 Discussion

Models of crack propagation of isolated fractures in ice shells underestimate the amount of stress required to fully penetrate the ice due to the highly fractured state of the ice shells. The effect of accounting for adjacent cracks is to lower the stress intensity at each crack tip since tensional stress is reduced in slabs between fractures. It is likely that even if fractures are not perfectly parallel, segments or blocks of ice

between the fractures have a reduced tensile stress. Since the stress intensity factor is decreased at the crack tip, to further penetrate the fracture, the applied stress must increase to cause through thickness penetration.

One way in which to increase the likelihood of full shell rupture is to consider fluid-filled basal fractures. This is a feature that is often cited as improbable due to the ductility of the basal layer of ice, but we suggest that under certain regimes basal fractures can form under stress. Basal crevasses are prevalent at the base of ice shelves even though the bottom of the ice shelf is at the pressure melting point. Water pressure can at least partially counteract the closing effect of lithostatic stress. Our linear elastic fracture mechanics model demanded that we consider only the section of the shell which deforms elastically, and so our assumptions on that depth affected our results. A larger or smaller stressed fraction may allow or further preclude complete fracture penetration of that layer.

In the case of Enceladus more so than Europa, another consideration is how the small radius of curvature can affect it. It was shown by *Walker et al.* (2012) that results of rift and ridge flexure calculations were significantly altered when the curvature of the surface was taken into account (Appendix A). In the case of the stress intensity problem, membrane and bending stresses can further contribute to the net value and affect the vertical propagation of a fracture in Enceladus' ice shell (the effect is not as large for Europa).

Another implication of our study of the effects of multiple fracture interaction and how they affect the existing stress field is the opening rates for fractures like the tiger stripes. These fractures are thought to release plumes of gas and water under the control of tidal shear and normal stresses (*Hurford et al.*, 2007a; *Porco et al.*, 2013), but to accurately model their opening and closing by tides, their setting amongst other fractures must be taken into account. In the case of multiple fractures, horizontal stress fields are also affected and the applied tidal stresses must be able

to open rifts between which tensile stress cannot exist. This may match well with the hypothesis that in order for the south polar plumes to be concentrated into 98 individual jets along the fractures, the fractures must be very narrow (*Porco et al.*, 2013), i.e., existing tidal stresses are not capable of opening the tiger stripes to the extent previously thought. It is likely that once a fracture penetrates to the depth of a subsurface reservoir and enables active venting, volatiles and gas that fill the fractures lead to increased pressure on the fracture walls (e.g. *Kieffer et al.*, 2006). This increased horizontal pressure on the walls may lead to a similar effect of water pressure in basal fractures, in that they oppose the closing effect of overburden stress and enable further opening of fractures.

5.6 Conclusions

Cracks that propagate in a field of fractures are less likely than single, isolated fractures to penetrate the full ice shell thickness unless larger tensile stresses are present than have previously been reported. Higher stresses, like those predicted for tectonic or re-orientation events in the shells of Europa and Enceladus may be sufficient to fully fracture a thin shell, but the estimated tidal stresses on the order of 0.1 MPa are not. Our results firmly suggest that the fact that the shells are so fractured has significant impact on the feasibility of completely fracturing the ice shell. This conclusion serves to suggest that the highly-fractured state of the ice shells at Europa and Enceladus should be considered in models of fracture propagation and in models of subsurface material escape. Our results advocate the likelihood that the most likely means of enabling through penetration are the formation of basal fractures, and despite previous skepticism, based on terrestrial observations they are likely to exist. An area of future exploration would be to further investigate conditions required for their formation and effects of plume eruption (from a high pressure subsurface reservoir) on their opening rates.

CHAPTER VI

On the Formation of a Rift Basin in the Ice Shell at the South Pole of Enceladus

6.1 Introduction

Saturn's moon Enceladus is unusual in that it is among only a handful of solar system objects known to be geologically active; a striking characteristic given that the global surface temperature is 70 K and the moon, covered in an icy shell, has an effective radius of only 250 km (*Porco et al.*, 2006). Observations of the icy surface indicate a long history of activity and deformation. Different sections of the surface range in age from primordial (cratered plains regions have estimated age up to 4.2 billion years or 1.7 billion years, depending on impactor flux model used (*Spencer et al.*, 2009b)) to geologically recent (*Porco et al.*, 2006; *Bland et al.*, 2007; *Barr*, 2008). The variation in surface features and ages across the moon imply that regional, rather than global, resurfacing processes are dominant (*Kargel and Pozio*, 1996).

The region of interest in this paper is the South Pole Terrain (SPT), the youngest region of the satellite's surface with an age <10 Myr (*Barr and Preuss*, 2010). The SPT most notably features the "tiger stripe" fractures at its center, along with their associated active plume vents (e.g. *Spencer et al.*, 2009b). Evidence of continual tectonic activity in the region and the observation of the active venting at the South

Pole suggest the possibility of a subsurface ocean (e.g. *Collins and Goodman*, 2007). The SPT on the whole has been described in detail by *Gioia et al.* (2007), *Spencer et al.* (2009b), and others; the terrain can be generally classified into the central tiger stripe terrain, which coincides with the underlying thermal anomaly at the South Pole, a slim circular terrain which surrounds the central terrain but has few fractures of its own, and a prominent, concentric ring of ridges. The floor of the region is relatively flat and shallowly depressed relative to the geoid (*Thomas et al.*, 2007; *Schenk and McKinnon*, 2009). Estimates of the depth of the floor range from 200 m (*Thomas et al.*, 2007; *Roberts and Nimmo*, 2008) to about 500 m at the center (*Helfenstein et al.*, 2011) and up to about 800 m (*Schenk and McKinnon*, 2009), depending on assumed shape models and density structures within the ice, respectively. The area is enclosed by a curved, pole-ward facing cliff system, creating a nearly-circular border to the region at about 55°S (*Spencer et al.*, 2009b) and has been interpreted as a convergent feature resulting from compressive stress along that boundary in the North-South direction (*Porco et al.*, 2006). The steep footwalls and gradually sloping flanks have been estimated to be roughly 1 km in height (e.g. *Schenk and McKinnon*, 2009; *Spencer et al.*, 2009b). Another significant feature of the SPT manifests itself in a radial set of large rifted features, extending in a "starfish" shape towards the equator (*Gioia et al.*, 2007) (Figure 6.1). Speculation that the topographic appearance and activity at the SPT are manifestations of subsurface dynamics and/or variability in structure is bolstered by the observation of a hotspot beneath the SPT region (e.g. *Howett et al.*, 2011) suggesting that the SPT may have a (partially) tectonic origin.

Similarly, rift basins found on the Earth are generally complex features, but can be characterized by large-scale structural components, including: a depressed floor or trough, occasionally found to have relatively flat (e.g. *Colman et al.*, 2003), *Lagabrielle et al.* (1997) and faulted (e.g. *Allen and Allen*, 2005), (e.g. *Withjack et al.*, 2002) floors; moderately-to-steeply dipping footwalls, uplifted flanks, and border faulting; and

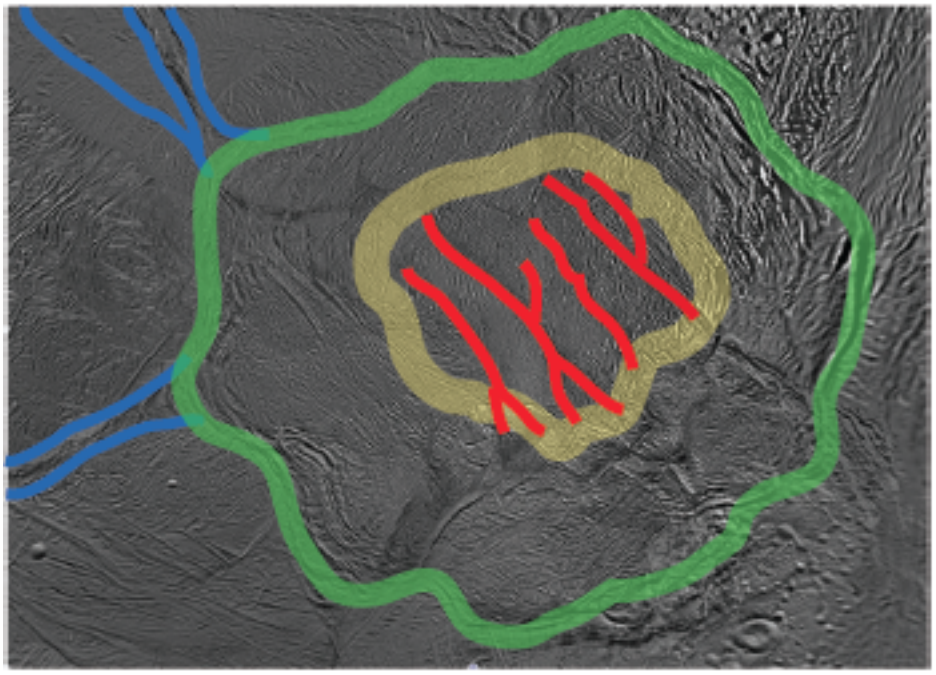

Figure 6.1: Enceladus' South Polar Terrain, imaged by Cassini (NASA/ JPL/ Space Science Institute). The major sections of topography at the SPT are denoted here: the four main tiger stripes marked in red, within the central depressed tiger stripe terrain outlined in yellow; the surrounding region that appears mottled but has few fractures itself, also depressed, outlined in green; the green outline, thereby, also highlights the location of the mountainous uplift at the boundary of the region. The highest point of uplift is estimated at 1 km. Blue lines radially outward from the SPT mark two of the "starfish arms" - large-scale fracture features radiating away from the SPT towards the equator.

transform zones (*Withjack et al.*, 2002). Noting the topographic similarity between rift basins on the Earth and the SPT region of Enceladus, we seek to use simple terrestrially-motivated rift basin models to determine if the predicted magnitude of rift basin depression and mountainous uplift are consistent with observations. The models are intended to explain the overall shape of the region (i.e., floor depression and uplifted flanks) rather than the tiger stripe rifts themselves; our models seek to provide the tectonic setting in which such features could form (subject to additional tidal forcing, e.g., tidal flexure, differential rotation of the shell, etc.).

To explore the possibility that similar processes formed the SPT, we examine three mechanical models that have historically been proposed to explain the topographic signatures observed in terrestrial rift basins, and examine which of these models are consistent with observed topographic features of the SPT. The models we examine here provide first order estimates of the processes controlling basin floor depth and the height of the rift wall bounding fault zone consistent with known material properties, rheological structure of the moon and observations. The models we use are summarized in the next sections, after which we present our results, and then compare the topography predicted by the models with observed topography at Enceladus.

6.2 On the North Fiji Basin

While the parallel rifts on Enceladus' SPT are a unique feature, the phenomenon is observed elsewhere. Our application of a terrestrial rift basin model to Enceladus' south pole was motivated by the observation that the North Fiji Basin (NFB) in the South Pacific exhibits similar features. Most notably, the NFB features several currently-active rifts that are parallel, along with some remnant rifts following the parallel trend but are not North-South trending as the current rifts are, reminiscent of the "paleo tiger stripes" of the SPT shown by *Patthoff and Kattenhorn* (2011). The NFB, as the result of intensive studies by various international scientific teams,

is one of the most extensively researched sections of sea floor, and is one of the most evolved back-arc basins in the world's oceans. It has the largest cumulate length of active spreading centers for a given surface of ocean floor (*Lagabrielle et al.*, 1997) in the world. Much like the SPT of Enceladus, the area is dominated by rifting patterns, which makes it a unique example among the world's oceanic basins. *Lagabrielle et al.* (1997) reviewed a comprehensive body of geological, geophysical and geochemical evidence which collectively demonstrated that a hot upper mantle underlies the NFB, suggestive of a similarity to the high heat anomaly beneath the SPT. Active upper mantle convection is a key process in controlling the large crustal and lithospheric dynamics in the NFB, and is largely independent from the evolution of larger structural features, such as the Vitiaz and New Hebrides subduction zones; i.e., the spreading at the ridges is largely controlled by the existence of subsurface heat and subsequent convection rather than the subduction action zones at the borders. This independence of the NFB basin formation from an adjacent subduction zone suggests that the maintenance and propagation of the ridges may be similar to that of the SPT, as the SPT features are likely dependent upon subsurface processes rather than active subduction, e.g., convection (*Barr*, 2008; *Mitri and Showman*, 2008). At large scale, the NFB can be considered and/or interpreted as a deformation zone at the boundary of two different plates, or tectonic regions (*Auzende et al.*, 1995).

The currently active spreading system includes the main Central Spreading Ridge (CSR), roughly North-South trending (Fig. 6.2), which lies in the middle of the basin floor, and a smaller parallel spreading ridge system (the West Fiji Ridge (WFR)) to the west. The WFR consists of successive segments, and is generally southward-propagating (*Huchon et al.*, 1994). The cumulate length of active spreading centers in the NFB, whose surface is on the order of 10^6 km^2, is more than 2500 km. The ratio of ridge length over basin surface is thus 0.0025 per km, which is about 20 times higher in the NFB than in the whole of the Pacific ocean floor (*Lagabrielle et al.*,

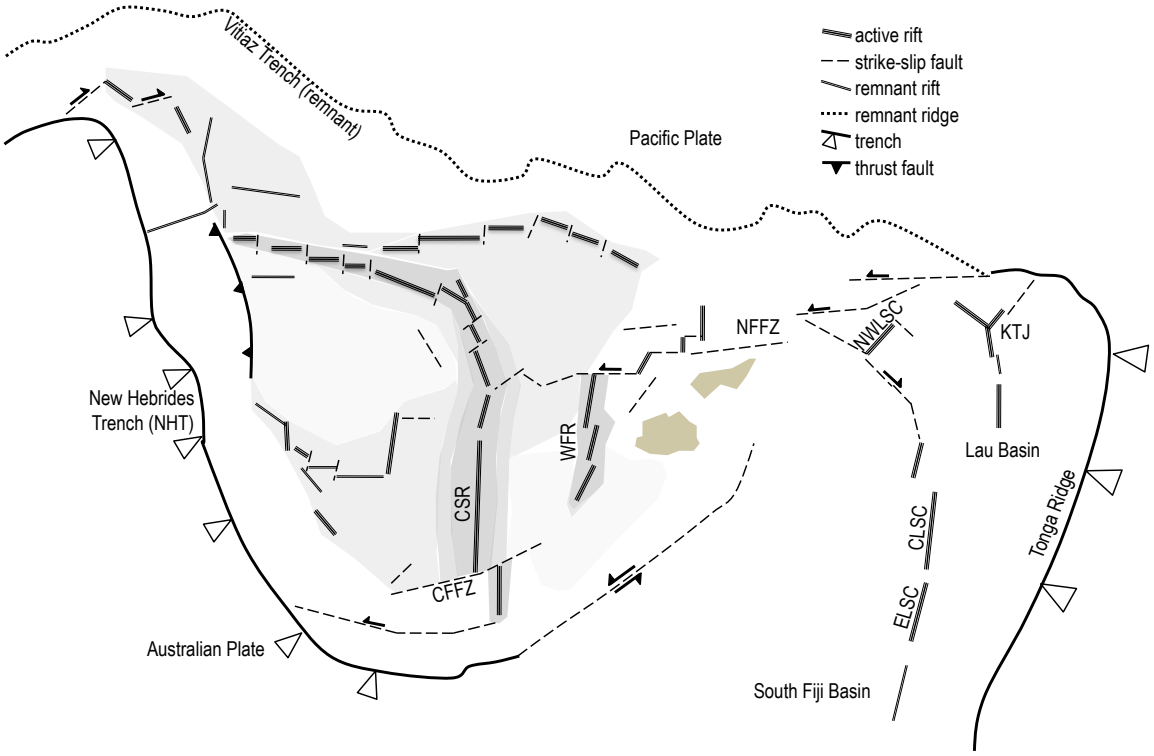

Figure 6.2: A tectonic map of the North Fiji Basin in the South Pacific ocean. The multiple active parallel rifts at the center region of the basin lie in a region that is depressed by about 500 m. They are surrounded by a convergent zone to the south, east, and west and a remnant rift to the north.

1997), a ratio which exhibits the highly rifted nature of the area. Comparatively, the SPT features a ratio of cumulative rift length (approximately 600 km) to basin area (approximately 70,000 km^2) of approximately 0.0085 per km.

Unlike the parallel ridges of the NFB on the Earth, in which active rifting takes place, the size and formation of the SPT may not have been enough to activate the rifts; it is possible that the tiger stripes are features synonymous to "failed rifts", or passive rifting, in the terrestrial setting. Passive rifting is also related to heating and thinning, but rather than an impinging mantle plume placing tensional stresses on a section of lithosphere, existing tensional stresses cause the lithosphere to fail, allowing a flow of mantle material upwards. This is the basis for the McKenzie model, in which rifting is a passive response to a regional stress field. It is possible that the

SPT formed as a result of lithospheric failure, or thinning of its solid ice shell, due to a regional stress field in the near-surface interior, which allowed for warm subsurface ice or water to approach shallower depths than in the rest of the ice shell. This is consistent with the observed features that appear to have originated by faulting and collapse at the boundaries, and flexural uplift at the rift flanks that are consistent with terrestrial models of uplift at, in addition to sea floor rifts, at Antarctic ice shelf rifts also. Our inquiry as to whether or not the bizarre topography at the SPT could have formed in the fashion of a basin on the Earth was motivated by our simple observation that the NFB seemed to be somewhat similar in appearance. We therefore use simple basin models to illustrate large-scale agreement with both the NFB and SPT topography.

6.3 Mechanical models of basin formation

The three terrestrial basin-forming models we consider are illustrated in Fig. 6.3. The first model, formation due to thinning, shall describe the subsidence of the floor, while we intend to describe the flank uplift at the sides of the basin using the flexural models. These models are not necessarily independent and we later include the non-local flexural response of the ice into the thinning model. We describe the physical setting of each model in the following sections. We note that Enceladus has a radius of just 250 km, and so in contrast to the traditional Cartesian geometry often employed, our model calculations are carried out using a spherical geometry, described in Appendix A.

6.3.1 An icy analog: Enceladus' structure

Prior to constructing mechanical models of the SPT topography, we need to make assumptions about the internal structure and composition of Enceladus (Fig. 6.4). We consider Enceladus to be differentiated with a rocky silicate core and a concentric

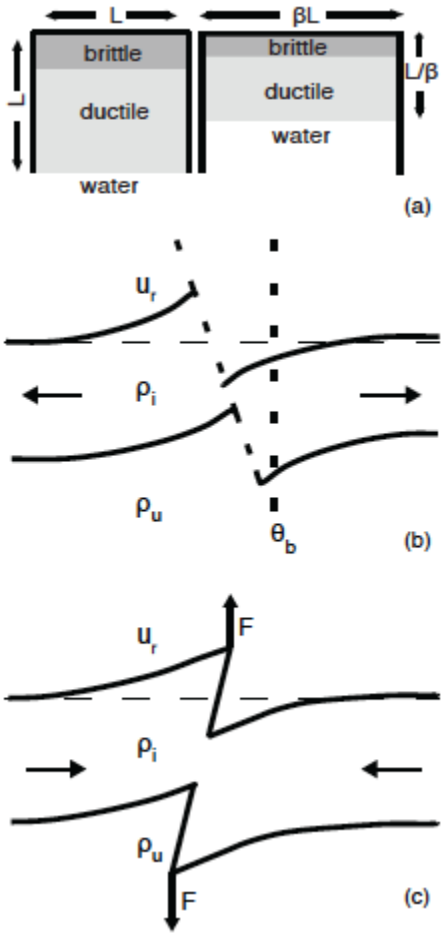

Figure 6.3: Schematics of the three basin models considered: (a) Thinning model: a section of crust is stretched by β, thereby thinning the solid layer by β, which leads isostatic imbalance and subsequent subsidence at the surface. (b) Extensional model of rift flank uplift: Dependent upon elastic response in the crust, we envision tensional forces pull apart a crustal block which breaks at angle θ_b, causing uplift u_r. The footwall block (right) rises to maintain isostasy above the hanging wall block (left). (c) Compressional model of rift flank uplift: assuming an elastic response in the crust, we envision that horizontal forces push on a block until it breaks, causing a reverse fault and uplift u_r. All three models are dependent on layer properties, most importantly ρ_i (ice density), and the density of the underlying substratum, ρ_u. In our models we consider several states for ρ_u.

water and ice layer of approximately 100 km, up to Enceladus' effective radius of 250 km. We assume this 100-km outer layer consists of a liquid layer between 40 and 60 km thick (roughly consistent with estimates by *Barr and McKinnon* (2007); *Barr* (2008); *Mitri and Showman* (2008); *Smith-Konter and Pappalardo* (2008); *Olgin et al.* (2011); *Patthoff and Kattenhorn* (2011)) beneath an upper layer of solid ice between 60 and 40 km, respectively (consistent with estimates above). Unlike rocky material, ice remains brittle up to the melting point and so, consistent with previous studies, we define the brittle-ductile transition as the depth d that a fracture penetrates. We generally assume the brittle layer thickness H_b to be 3 km, on the high-end but roughly consistent with *Tobie et al.* (2010), who showed the brittle-ductile transition depth to be 2 - 3 km, but consider a range of fracture penetration depths. Later, we employ an elastic layer thickness to investigate the flexural response in the ice. Although not well constrained (*Smith-Konter and Pappalardo*, 2008), estimates for elastic thickness in the past range between 0.3 km in flexural studies by *Giese et al.* (2008), 0.4-1.4 km in heat flux analyses (*Bland et al.*, 2007), at least 0.5 km in satellite reorientation models (*Nimmo and Pappalardo*, 2006), and up to approximately 8 km in tidal stress models (*Smith-Konter and Pappalardo* (2008), *Olgin et al.* (2011)). In order to justify our own use of values, we computed preliminary results using a range of values for elastic and brittle thickness (between 1 and 10 km), and compared these to the profile produced by *Schenk and McKinnon* (2009). Keeping in mind that this single profile may not be completely representative, our best RMS misfit values come from elastic thicknesses between 1 and 5 km; however, the elastic thickness of 1 km curve also reaches roughly the elevation that we would expect (1 km). It is due to this that we assume a 1 km elastic thickness, which also allows us to remain roughly consistent with the lower range of previous estimates.

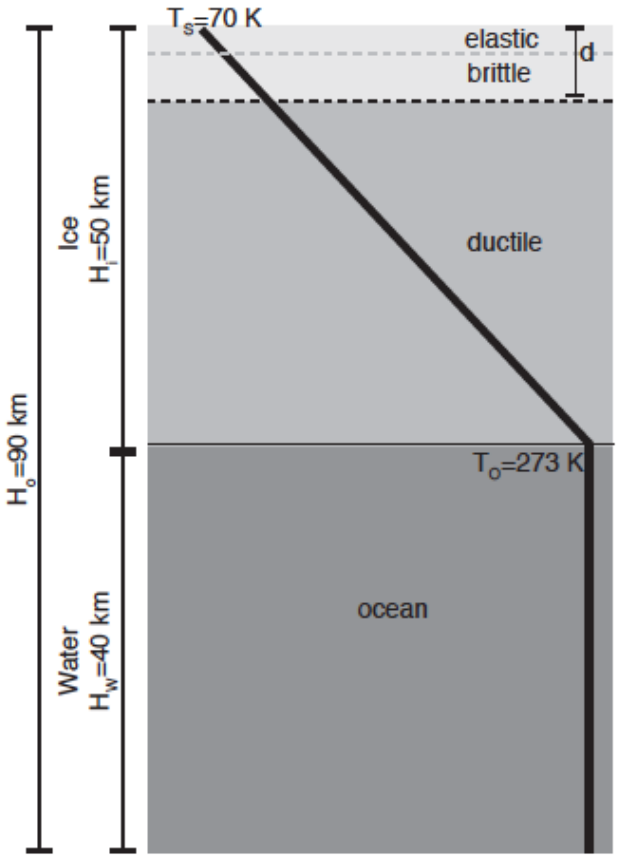

Figure 6.4: Model structure for Enceladus. We assume an ice shell of thickness 50 km over an ocean of 40 km depth, for a total outer water-ice layer of 90 km. For models of flexure, we assume that the elastic thickness, T_e (light gray), at Enceladus is 1 km. The brittle layer of ice, or the depth t which fractures penetrate (d), is taken to be 3 km (though we experiment with upper bounds in our results). We assume a surface temperature of 70 K, a thermal gradient in the ice layer (thick black line), and an isothermal water ocean (dark gray) beneath at 273 K.

6.3.2 Subsidence of the SPT floor

The first model we consider is motivated by early studies of sedimentary basins on Earth. *McKenzie* (1978) hypothesized that the stratigraphy of basins was formed through stretching and extensive normal faulting in the brittle crust (as suggested by *Vening-Meinesz* (1950)), followed by local isostatic subsidence. In contrast, for a basin to form without horizontal stretching, a large amount of material must be removed by erosion. In the case of Enceladus, even the most conservative estimate for elevation change would require the removal of 200 m (*Thomas et al.*, 2007) of icy material across the approximately 300 km wide area across the South Pole. Although the terrestrial *McKenzie* (1978) model involves complexities due to thermal diffusion that are not relevant to our simpler ice-water structure, we postulate that the extensional portion of the model still provides a reasonable setting in which the SPT basin may have formed.

The *McKenzie* (1978) thinning model (Fig. 6.3a) describes a section of lithosphere that is stretched and thinned, allowing warmer subsurface material to rise to fill the thinned region from below. Neglecting elastic effects, the subsidence of the floor is described as the isostatic adjustment due to the thinning, where, as in *Schenk and McKinnon* (2009), the isostatic adjustment at the base of the shell is given by

$$S_i = \frac{l \Delta \rho g_b}{\rho g_s} \tag{6.1}$$

where l is the amount of thinning of the ice (positive upwards from the base), $\Delta\rho$ is the density difference between ice and water at the base of the shell, ρ is the ice density, and g_s and g_b are the surface and basal acceleration due to gravity, which ranges between 0.11 up to 0.15 m/s^2, respectively, depending on the thickness of the ice shell.

This model is attractive in that it describes the formation of a depressed surface

associated with a thinned ice layer. The model, however, has several deficiencies, including the possibility of regional (flexural) compensation. We can address this easily by including a finite elastic thickness of the ice. More problematic, we have employed this thinning model to describe the floor subsidence, but we also need to explain uplift at the boundary of the subsided region. To bound the magnitude of uplift, we imagine that we have one of two scenarios. In the first scenario, we assume the SPT is subject to a large-scale tensile stress and examine whether rift flank uplift as the result of the formation of extensional grabens is sufficient to explain the size of the mountains. In the second scenario, we imagine that the tensile stresses that caused subsidence are more local, allowing for extension in our basin that is then compensated by compressional stress at the edges of the region. These flexural models are described next.

6.3.2.1 Flexural response to thinning

If we assume that at least the top layer of cold ice behaves elastically (elastic thickness: 1 km) and that the extension is accommodated by a brittle layer H_b of roughly 3 km, the change in topography due to thinning at the SPT described above induces a flexural response in the elastic shell, described by the spherical flexure equation (Equation A.21). The pressure at the base of the shell can be found as in *Turcotte et al.* (1981) for a change in topography:

$$p = g\left[\rho_i h - \rho_u h_g - (\rho_u - \rho_i) u_r\right], \tag{6.2}$$

Here, ρ_i is the ice density and ρ_u as the underlying substratum density (here defined as warm ductile ice), h is the change in topography after thinning, h_g is the displacement of the geoid, and u_r is the flexure of the shell as before. The associated force over the basin (F_r in Equation A.21) induces bending stress in the elastic shell in the ϕ

direction (co-latitude), calculated as (*Tanimoto*, 1997)

$$\sigma_{\phi\phi} = \frac{E}{1-\nu^2}\left(\varepsilon_{\phi\phi} + \nu\varepsilon_{\psi\psi}\right), \tag{6.3}$$

where $\varepsilon_{\phi\phi}$ and $\varepsilon_{\psi\psi}$ are extensional strains. In determining stress over the shell, we can investigate points at which the yield strength of ice is surpassed, and therefore predict possible boundary fault locations (at which the uplift, calculated above, would occur). While the yield strength of ice at Enceladus is difficult to constrain (*Rudolph and Manga*, 2009), in this study we assume a yield strength of 1 MPa, consistent with terrestrial values (*Bassis and Walker*, 2011) and experimentally derived values for temperatures more appropriate for icy moons (e.g. *Schulson*, 1999).

6.3.2.2 Boundary flexure due to crustal extension

It was suggested by *Vening-Meinesz* (1950) that if an extensional force were applied to a section of crust, normal faulting would eventually occur, illustrated in Fig. 6.3b. In the past it has been applied to active rift systems as well as to basin settings; more specifically, to "syn-rift" basins that form in response to extension, e.g., sea-floor spreading (a mechanism that had previously been suggested for the tiger stripes (e.g. *Parkinson et al.*, 2008; *Abramov and Spencer*, 2009)). The Vening-Meinesz model considered the mechanics of blocks on either side of a fault (the original crustal block fractured along an angle, effectively leading to a reduction of mass of one crustal block (the footwall) and the addition of this mass to the opposite block (the hanging wall) (*Watts* (2001), p. 290-294), as illustrated in Fig. 6.3b). In this terrestrial model, when considering the restoration of isostasy, the removal of mass from a section of crust will cause uplift and that area will rise; likewise the addition of mass to an adjacent section of crust, the hanging wall, will cause loading and sinking.

In estimating the point of greatest curvature, and therefore bending stress, it is

possible to determine the distance along the surface to a break in the plate. After this break, the gradual sinking of the downward block is eventually counteracted when the wedge is "caught" by the inward-sloping walls of the normal faults, unless extensional forces continue to act. This process produces a structure called a "graben," a bounding fault zone that characterizes a terrestrial basin (*Schlische*, 1991). After *Watts* (2001), faulting disturbs the isostatic balance of the initial block, and a load is applied by the crustal block on the left in Fig. 6.5 onto the right block.

While this is easily applied to the layer and density structure of the Earth, because the ice can remain brittle up to the melting point, in our study we can envision three different scenarios. In case A, we consider the (unrealistic) upper bound and imagine that brittle faulting due to extension penetrates the entire shell (fault depth d = shell thickness H_i). In case B, we allow faulting to penetrate a brittle layer thickness of 3 km, overlying a ductile ice layer. In this case, we can assume that the ductile layer is either (i) entirely relaxed, thus negating any upward force at the base due to hydrostatic equilibrium, or (ii) that it is not entirely relaxed, and an upward force at its base due to the loading of the subsided block results in some amount of surface uplift. In case C, if we assume that the ductile layer of ice is partially infiltrated by ocean water, then a dense layer underlies the surface ice and allows for a small amount of buoyant uplift.

Regardless of the case we consider, in order to determine the flexure in Equation A.21, we must determine the force experienced by the shell in extension. To do this, we consider the process described by *Watts* (2001), and adapt it to our spherical frame (outlined in Appendix A). We find that the force on the shell at the plate break can be expressed as

$$F_E = \frac{A_{ACD}\rho_i g S_i}{T_e L_\phi}, \tag{6.4}$$

where we have defined T_e as the elastic thickness; ρ_i as the density of ice (averaged); g is the acceleration due to gravity; S_i is the vertical distance the subsided block

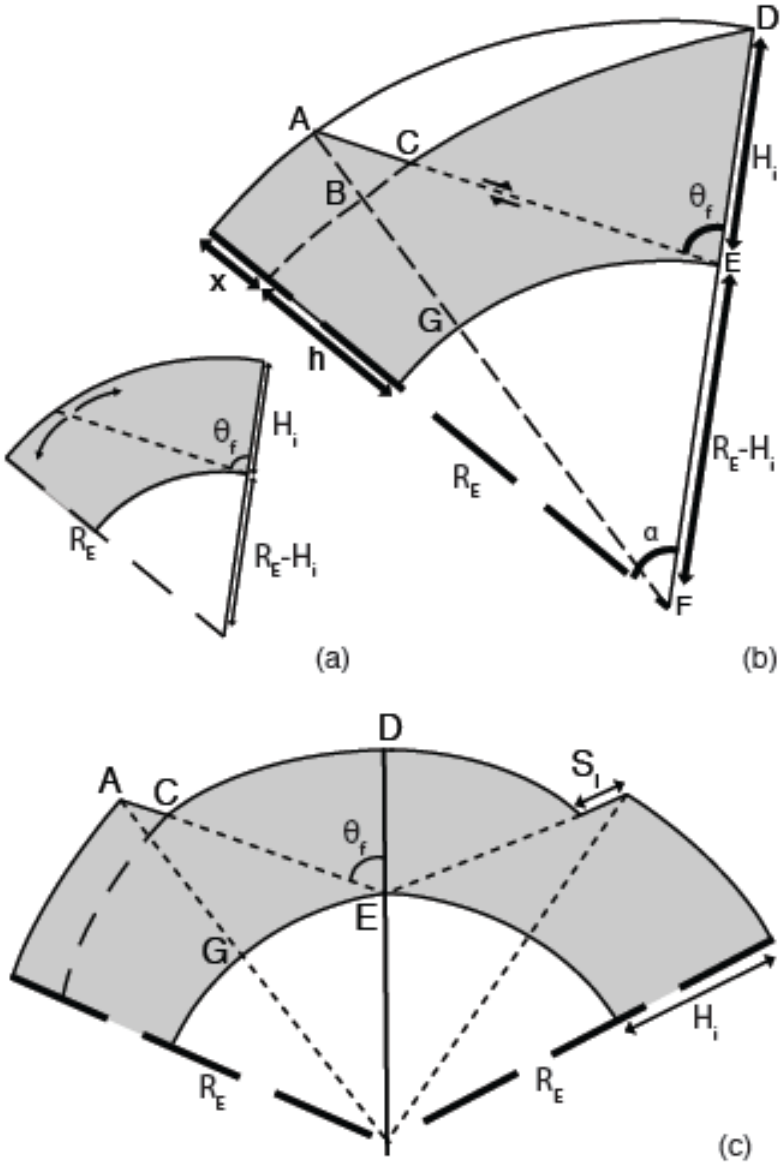

Figure 6.5: Schematic diagram illustrating the geometry of a section of shell in extension and the effective load neccessary in order to return to isostatic equilibrium after a normal fault disrupts balance. (a) Prior to rifting, extensional stresses act on a section of shell; (b) the right hanging wall block slides downward, creating an isostatic imbalance thereby inducing uplift of the left footwall block; (c) a second break due to bending stress creates (ideally) a symmetric graben structure about the South Pole. Adapted to the spherical equivalent from *Watts* (2001), Figure 7.6.

has been forced down as defined in Equation 6.1; L_ϕ is the length of the bending surface between breaks in the ϕ (co-latitude) direction, here taken to be the width of the SPT; and A_{ACD} is the area of semi-triangle ACD in Fig. 6.5. This equation effectively calculates the force initiated by the subsided block that impinges upon the base of the shell at the opposite block and can be simplified down to the linear elastic plate case found in *Watts* (2001) by altering the geometry in Fig. 6.5.

6.3.2.3 Boundary flexure due to crustal compression

Bullard (1936) hypothesized instead that rift basins formed in compressional stress regimes. We suppose that local extension that created the subsided floor of the basin may have resulted in corresponding compression at the border of the region that then results in uplift. In the *Bullard* (1936) theory, compression would cause a reverse fault, allowing one crustal block to ride up on the opposing block, resulting in buoyancy-induced flexure (dependent on density differences between layers), as illustrated in Fig. 6.3c. *Bullard* (1936) further proposed that the reverse faulting causes bending of the opposing block, leading to a second plate break (from extension) in the plate where the bending stress is greatest, allowing the central block to sink, thereby forming a basin. To determine the depth and width of a rift valley in this model, Bullard used an early broken elastic plate model developed by *Jeffreys* (1915), using a calculated force on the end of the plate.

As in the extensional case (Section 6.3.2.2), while this proposed process works well for the structure and densities of the Earth's layers, we have to think carefully about how to apply an analogous model to the ice and water layers at Enceladus. In case A, we imagine again that the entire ice shell behaves as a brittle layer, allowing faults to penetrate through to the base ($d = H_i$); in case B, we assume a more realistic brittle layer thickness of 3 km, allowing fractures to penetrate to this depth only over a ductile ice layer below; and in case C, we again investigate the possibility

that there exists an ice-water mixed layer that allows for buoyant uplift of the dense, cold surface ice. Of course, as before, the outcome is dependent upon the density differences between layers; by splitting Case B into two subsets (density difference between warm and cold ice vs no density difference at all), we will show that in this case that densities have less of an effect, ceding dominance to the assumed elastic thickness term (1 km).

As in the extensional model, we use our spherical flexure equation (Equation A.21) and apply a calculated line force at the plate break to determine uplift. To determine this upward force acting at the plate break, we adapt the approach of *Bullard* (1936) (as adapted by *Watts* (2001)) to our spherical structure, and express the force as

$$F_C = \frac{\rho_u L_\phi g x}{2T_e} \tag{6.5}$$

where ρ_u is defined again here as the underlying layer density, dependent on which case (A, B, or C) is being considered (ice or water density). This force is then applied at the plate break to determine uplift.

Geological evidence has subsequently shown that most terrestrial rift basins formed in extensional rather than compressional tectonic stress regimes, a criticism that has since proven fatal to the *Bullard* (1936) hypothesis (e.g., (*Weissel and Karner*, 1989; *Watts*, 2001)), as measurements of gravity and increased observations of rift valleys could be better explained in an extensional regime. Nonetheless, compression has been proposed as a mechanism for the SPT mountainous features and we consider this as a viable model for the uplift surrounding the SPT basin, even if it is not observed on Earth.

6.4 Model results and comparison to topographic observations

6.4.1 Subsidence of the basin floor due to thinning

In applying our thinning model (i.e., Section 6.3.2), we assume that a section of the icy shell was stretched by a factor of β due to far-field extensional stresses (e.g. *Withjack et al.*, 2002; *Allen and Allen*, 2005) leading to thinning of the ice shell in the localized region beneath the SPT (final extended basin width can be calculated by β and an initial basin width). In this case, this assumed instantaneous thinning causes subsidence S_i (Equation 6.1). We find that by stretching the region by $\beta = 1.11$ to 1.13 thins the crust by approximately 5 to 6 km, and the resulting topographic subsidence is approximately 600 m. This value corresponds reasonably well with previously published estimates of SPT topography and the elevation change, which range between 200 and 800 m (*Thomas et al.*, 2007; *Roberts and Nimmo*, 2008; *Schenk and McKinnon*, 2009; *Helfenstein et al.*, 2011).

6.4.2 Flexural response of the crust

6.4.2.1 Flexural response to thinning

The change in topography due to thinning at the SPT induces a flexural response in the shell, described by Equation A.21. This flexure (top) and stress (bottom) are shown in Fig. 6.6. Black squares on the stress curve denote the location at which the stress in the elastic shell surpasses 1 MPa, our projected yield strength of ice. These points result in a basin floor with a diameter of approximately 250 - 310 km, illustrated by white squares in the top panel. This result roughly agrees with observations of the basin width (approximately 300 km across in the ϕ direction).

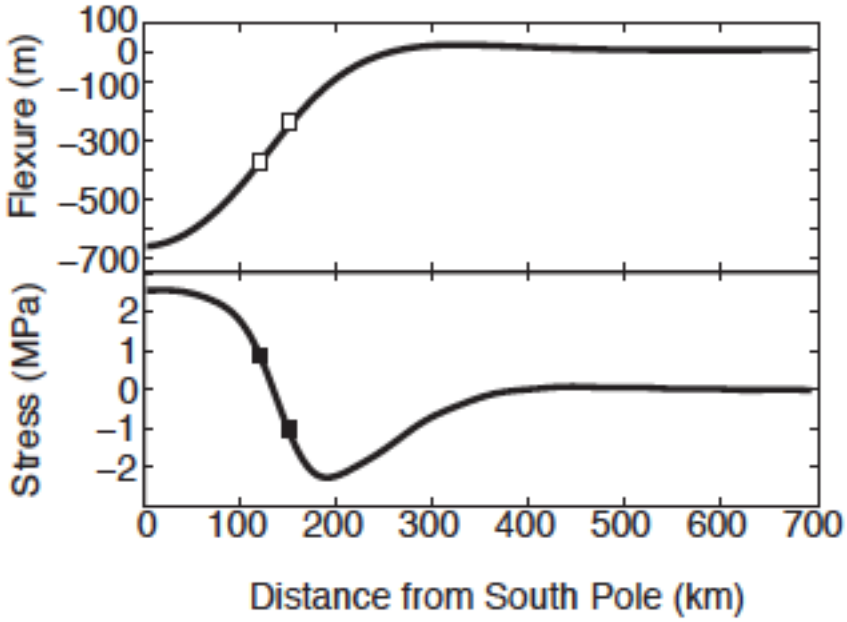

Figure 6.6: Flexure of the ice shell due to thinning-induced subsidence (top), used to calculate associated tensional stress (bottom). Black squares in the bottom panel show points at which stress surpasses 1 MPa, our assumed yield strength of ice. These locations are translated to the top plot in white, showing the locations at which the ice will fail, noting that negative stress implies compressive stress. This break allows for uplift at the boundary and shows the width of our predicted basin, roughly 240 to 310 km across, assuming an elastic response in the ice.

6.4.2.2 Boundary zone uplift by extensional forces

Porco et al. (2006) observe that the mountainous boundary reaches approximately 1 km in height, a value matched by *Schenk and McKinnon* (2009). In applying the model of crustal extension attributed to *Vening-Meinesz* (1950) (Section 6.3.2.2), we can calculate the amount of flexural footwall uplift, dependent upon the normal faulting angle (*Watts*, 2001) at the break. Fig. 6.7 shows the amount of uplift for an assumed fault angle of 20° and floor depression (about 500 m), for an elastic thickness of 1 km. The value is similar to best-fit values used to assess normal faulting on Europa, an icy satellite of Jupiter with a possibly similar ice shell. *Nimmo and Schenk* (2006) studied two possible normal faults on Europa and found best-fit angles to be 11° and 22°. Figure 6.7 shows that for this faulting angle in cases A, B, and C, if the South Polar basin formed in this extensional manner, flexural uplift at the boundary is predicted to be approximately 4.6 km in case A ($d = H_b = H_i$), 1.8 km in case B ($d = H_b = 3$ km) assuming the ice below is not completely relaxed (total viscous relaxation results in sinking rather than uplift), and 2.05 km in case C ($d = T_e$) over a "slushy" ice-water layer. Even this lowest result (Case B, also the most realistic) is about twice the height of the uplift observed today. Though it is likely that, over its active lifetime, the SPT has undergone additional topography-altering events (i.e., heights predicted here may have been altered by subsequent tectonic events), the requirements (i.e., cases A, B, and C) for uplift under extension are unlikely. So we conclude that the extension model cannot realistically predict the basin at the South Pole.

6.4.2.3 Boundary zone uplift by compressional forces

Similarly, in applying the compressional uplift model as described by *Bullard* (1936) (Section 6.3.2.3), we find that uplift can develop at the edge of the region if we assume that compression is accommodated at that location in response to the

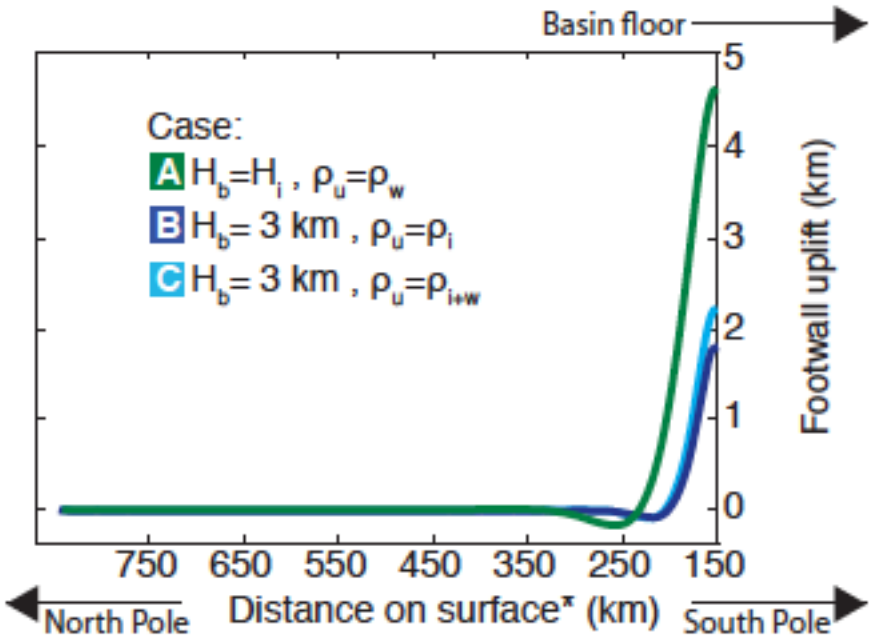

Figure 6.7: Footwall uplift in the case of extensional forces at the boundary of the SPT area. Uplift varies with assumed layer properties. Case A (green): Fracturing penetrates the entire ice thickness ($d = H_i$), and underlying substratum taken to be water ($\rho_u = \rho_w$). Case B (dark blue): Fracturing penetrates an brittle layer of 3 km, over a warm ductile ice layer, whose density is related to the temperature gradient in the ice layer (coldest ice at surface: 933 kg/m^3, warmest ice at base: 917 kg/m^3), i.e., $\rho_u = \rho_{i(warm)}$. Case C (light blue): Fracturing penetrates a brittle layer of 3 km, over a substrate of a "slushy" ice-water mixture.

extension of the floor. We find that the footwall uplift height of a basin with floor depth of roughly 500 m and elastic thickness of 1 km reaches approximately 2.6 km in case A ($d = H_b = H_i$), approximately 1.15 km in case B ($d = H_b = 3$ km) in which the brittle layer overlies warmer ductile ice, and roughly 1.06 km in case C ($d = 3$ km over"slushy" water-ice matrix). The most realistic scenario, case B (in which the brittle layer accommodates fracture overlying warmer ductile ice) also gives promising results, approximately the mountain height observed today (1 km). These results are shown in Fig. 6.8 and further discussed in our integrated model in the following section.

6.5 Discussion

6.5.1 Thinning and flexural uplift: Integrated model

In our best integrated model from those analyzed in the previous section, we postulate that the ice shell at the South Pole was stretched by local extensional stresses, which induced thinning of the shell. The associated subsidence, as described by our thinning model, places the SPT floor in a depression of 600 m. The local extension of the area is compensated by compression at the boundary of the thinned region, resulting in reverse faulting of the brittle ice layer (of thickness 3 km) overlying a warmer ductile ice layer, which results in uplift of roughly 1.15 km. We postulate that the overall bowl-shape of the SPT region is reflected in this model and that it begets generally favorable agreement with past observations of topography there. This integrated model also assumes a structure similar to that suggested by past analyses (e.g. *Smith-Konter and Pappalardo*, 2008; *Patthoff and Kattenhorn*, 2011) and others, with an ocean layer of 40 km underlying a solid ice shell of 50 km, which features an elastic thickness of 1 km. The stresses that we predict in the shell are larger than diurnal tidal stresses at Enceladus (*Rudolph and Manga*, 2009) but on the order of previous

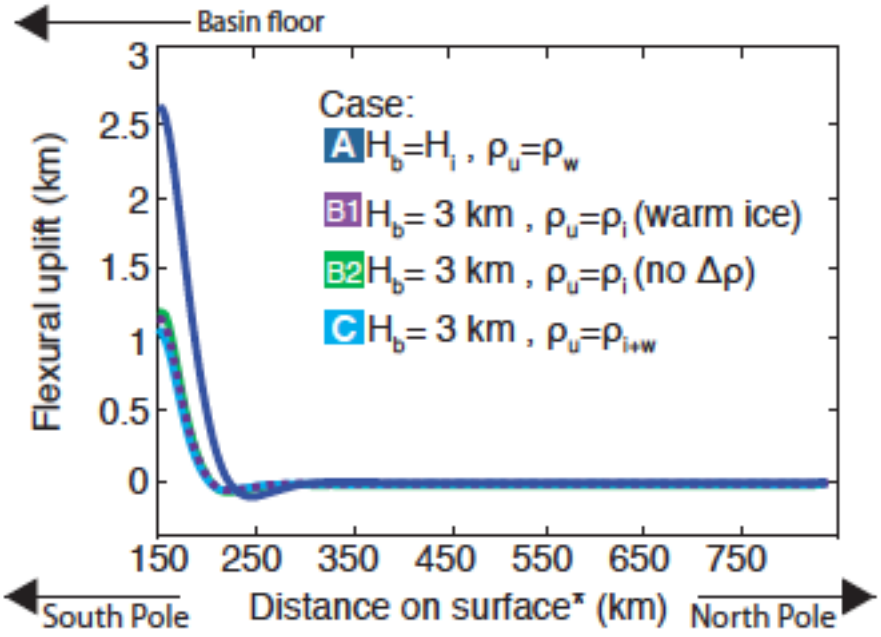

Figure 6.8: Footwall uplift profile in the case of compressional forces at the boundary of the SPT area. Case A (dark blue): Fracturing penetrates the entire ice thickness ($d = H_b = H_i$), and underlying substratum taken to be water ($\rho_u = \rho_w$). Case B1 (purple): Fracturing penetrates a brittle layer of 3 km, over a warm ductile ice layer, whose density is related to the temperature gradient in the ice layer (coldest ice at surface: 933 kg/m^3, warmest ice at base: 917 kg/m^3), i.e., $\rho_u = \rho_{i(warm)}$. Case B2 (green): similar to Case B1 in structure, this case was used to illustrate the small effect of assumed substratum density on result. In this case, we assume no density difference between the brittle ice and underlying ice, resulting in only a small change from the density-gradient version in Case B1. Case C (light blue): Fracturing penetrates a brittle layer of 3 km, over a substrate of a "slushy" ice-water mixture.

estimates of tectonic stresses (e.g. *Nimmo and Pappalardo*, 2006) and estimates of stress due to thickness changes (*Manga and Wang*, 2007). The locations along the surface where the stress surpasses our assumed yield strength of 1 MPa are marked in Fig. 6.9 as magenta (tensile) and orange (compressive) squares. It is worthwhile to note that the maximum compressive stress occurs at the flank location, bolstering our argument that our compressive model of flank uplift is appropriate here. It is also relevant to point out that, while our model exhibits axial symmetry, the "tiger stripes" notably break that symmetry, suggesting that the additional processes, such as tidal stresses, may be responsible for the observed symmetry-breaking formation of these features; the tectonic stress and thinning provide the background environment which makes this likely.

Fig. 6.9 shows the topography derived by *Schenk and McKinnon* (2009) through the use of digital terrain maps, illustrating the bowl-shaped basin of the SPT and its boundary uplift relative to sea level. As many properties and parameters at Enceladus are poorly constrained, the gray block in Fig. 6.9 exhibits the effect on the results when model parameters are varied. Varying the thinning model between upper and lower limits of published parameters at Enceladus cause the margin of resulting subsidence levels (gray) to remain fairly wide. Elevation estimates from published sources mentioned above are shown on the plot in Fig. 6.9 in varying colors, and exhibit a good fit within the grayed area of our model estimates. This agreement with previously published values reinforces the possibility that the extensional model is a viable model for subsidence of the floor (and therefore basin formation) at the SPT region.

While we include simplifying assumptions in our models (e.g., layer composition, column-averaged densities, assumed elastic thickness), our basin models do, in most cases, reasonably describe the subsidence and mountainous uplift at the boundary and provide self-consistent estimates of the uplift and subsidence of the topography.

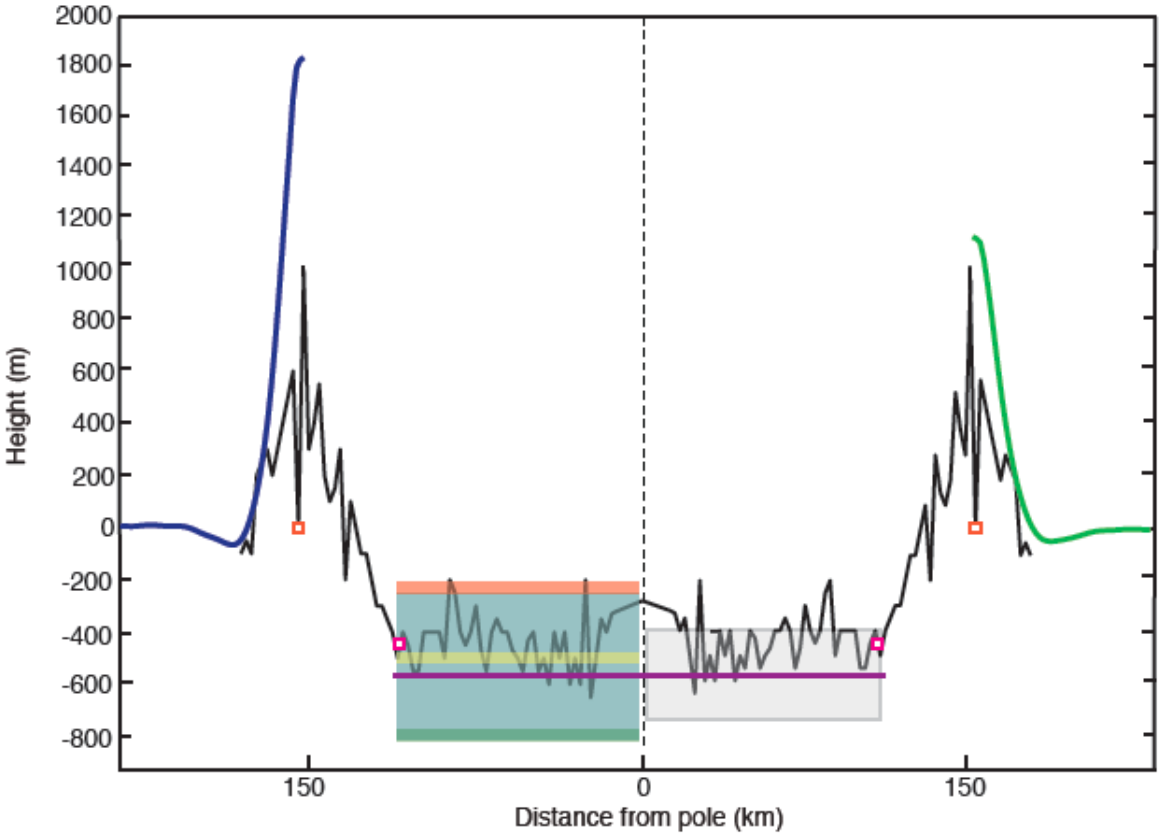

Figure 6.9: The topographic profile (black) of the SPT from *Schenk and McKinnon* (2009) is used to illustrate model results. Left hand navy blue line denotes the best-fitting result from the extensional model. This reaches approximately 1.8 km in height, assuming a brittle layer overlying a warm ductile ice layer. On the right hand side, the green line denotes our best fit curve of flank uplift in the compressional model, reaching 1.15 km, assuming a brittle layer of 3 km over a ductile layer of ice beneath. This result and structure match previous estimates of elevation and internal structure. Purple line denotes the subsidence we find from our thinning model (600 m depression); we put this in context of previous estimates of the depression depth at the SPT (*Thomas et al.* (2007) and *Roberts and Nimmo* (2008) (red); *Helfenstein et al.* (2011) (yellow); *Schenk and McKinnon* (2009) (green (lowest estimate)); teal box denotes the span of estimated depths at the South Pole). Due to the uncertainty in parameters at Enceladus, we include error in our assessment, marked by the gray box. Maximum extensional stress (magenta) and compressional stress (orange) are marked by boxes (see Fig. 6.6). Note that the profile is a single side of the basin mirrored over the central axis.

6.5.2 Terrestrial basins and implications for the SPT

Standard rift basins in the terrestrial setting are related to stresses in the crust and are idealized as manifestations of active or passive rifting. During active rifting, deformation is associated with impingement by a mantle plume (warm material) on the base of the lithosphere, causing thinning, doming, and eventual downwarping of the area, along with extensional rifting. Alternatively, under passive rifting, far-field tensional strains in the lithosphere cause a weakening of the surface material, allowing for upwelling of hot material (e.g. *Huismans et al.*, 2001). Most terrestrial basins exhibit features of both behaviors (*Allen and Allen*, 2005), and so these are generally regarded as end-members of the formation spectrum. They mostly refer to whether or not a basin forms at a plate boundary (active) or not (passive). Rift basins in general are complex features, but can be characterized by large-scale structural components, including: a depressed floor or trough, occasionally found to be relatively flat (e.g. *Colman et al.*, 2003; *Lagabrielle et al.*, 1997) and faulted (e.g. *Allen and Allen*, 2005; *Withjack et al.*, 2002); moderately-to-steeply dipping footwalls, uplifted flanks, and border faulting; and transform zones (*Withjack et al.*, 2002). These large-scale components of basin topography are observed at the SPT of Enceladus - the circular depression features a rifted floor, steep cliff footwalls, and uplifted boundary flanks (see original DEM profile by *Schenk and McKinnon* (2009)). The SPT also overlies a high-heat temperature anomaly, suggestive of the subsurface heating that normally goes along with basin formation, as noted above. The possibility that basin-forming mechanisms may be used to explain the formation of circular depressions on planetary surfaces has been suggested previously, both on Earth (e.g., the Michigan Basin (*Sleep et al.*, 1980)), and on other planets (e.g., Atalanta Planitia (*Solomon et al.*, 1982), and regions of Atropos Tessera (*Ori and Baker*, 1995), both on Venus) to explain the formation of circular basins that did not originate via impact cratering.

An example of thermally-driven basin formation presents itself in the North Fiji

Basin (NFB) in the Pacific Ocean. Overlying a hotspot, *Lagabrielle et al.* (1997)) showed that active upper mantle convection is a key process in controlling the crustal dynamics of the NFB, and is largely independent from the evolution of larger structural features, such as the Vitiaz and New Hebrides subduction zones (*Lagabrielle et al.*, 1997). This is an important point in our Enceladus application: the spreading at the ridges is largely controlled by the existence of subsurface heat and subsequent convection rather than the action of subduction zones at the borders. This independence of the NFB basin formation from an adjacent subduction zone suggests that the maintenance and propagation of its ridges may be similar to that of the SPT, as the SPT features are likely dependent upon subsurface processes related to South Polar hotspot rather than active subduction, i.e., heat and/or subsurface convection (*Barr*, 2008; *Mitri and Showman*, 2008) may have driven (and continue to drive) the evolution of the SPT. This study shows that the depression at the SPT could have formed during a tectonic event analogous to those responsible for the formation of rift basins on our own planet, an inquiry motivated by our simple observation that the NFB seemed to be somewhat similar in appearance and thermal setting. While current surface expressions of stress and activity (including the tiger stripes) are likely just the latest in a long history of deformation, we suggest that the original subsidence of the SPT floor, and therefore the large-scale shape of the region still seen today, may have originated in a similar fashion to Earth's basins.

It is also notable that stresses computed due to a change in topography of the icy shell are on the order of estimates of tidal stresses, bolstering the possibility that, first, stresses on this order exist in the shell, and second, that the shell reacts to such stresses (e.g., the activation of the tiger stripes). Our hypothesis was motivated by the simple observation that terrestrial rift basins have similar structural characteristics, including those mentioned above and an associated "starfish" pattern at the tectonic boundary, seen both at the SPT and tectonic boundaries on Earth (*Mahadevan et al.*,

2010).

6.6 Conclusions

Through an application of simple terrestrial basin models, we conclude that it is possible that the SPT of Enceladus formed by processes analogous to those associated with the formation of our own terrestrial rift basins. This application was motivated by the observation that the SPT topography agrees with the overall characteristics of a terrestrial rift basin, exhibiting a rifted central depression, steep footwalls, uplifted flanks, and border faulting, in addition to its existence over a high-heat spot that is independent of active subduction zones. Our best integrated model, assuming local extension of the shell at the South Pole that is accommodated by compression at the border, shows that our SPT basin attains a shape that approximates previous topographic estimates to a fair degree. Although we speculate on both compressive and extensional scenarios, in reality the models constitute end members of a continuous spectrum of processes; it is widely thought that Enceladus' SPT current form is the result of a sequence of tectonic events that continues today, and is likely a combination of many processes. Here we speculate only on the origin of the depression and ringed boundary uplift region.

While the compression case showed more favorable results, it is likely that the elevation of the mountains, in either case, has been modified by subsequent tectonic events. Our results, while based on simple models, lend themselves to the possibility that the general shallow bowl-shape of the SPT may have an origin similar to that of terrestrial rift basins. Future work could include enhanced modeling, most specifically the use of 3D geometries, the influence of rheology, and better estimates of ice strength at the SPT. Enhancing this model to the level of current advanced terrestrial basin models (e.g., those used for petroleum geology) would be a prudent next step.

CHAPTER VII

Conclusions and Future Work

7.1 Summary

The primary aim of this dissertation was to improve our knowledge of the processes and mechanisms involved in the fracture of ice, and the application of this knowledge to improving understanding of tectonic processes at the icy moons. Here we summarize each chapter to provide a roadmap from which to gain a sense of synthesis and a backdrop for our discussion of future work.

The variability of rifting in Antarctic ice shelves: In Chapter 3, we discussed the development of an observational record of Antarctic ice sheet-wide rift propagation over the decade 2002-2012, by observing a total of 72 rifts within 30 km of the ice fronts on 13 Antarctic ice shelves around the continent. This is the most comprehensive rift propagation dataset collected to date. The variation in rifting behavior emphasizes that rifting is a complex and variable process, and reinforces the idea that it is driven or controlled by more than one mechanism. We only found seven to be continuously active throughout the decade; one on the Filchner, one on the Ronne, and five on the Amery. Other rifts fell into one of three categories: (i) completely dormant; (ii) consistent intermittent propagation for two to eight years before arrest; or (iii) "sudden burst" propagation. We did not find an observable correlation between the rifting activity and changes in local atmospheric temperatures or

sea ice concentration, and there was no geographical pattern to the variation. However, we found that the arrival of tsunamis often triggers rift propagation in rifts that are front-initiated. This observational dataset serves as a basis for further study of regional and Antarctica-wide changes in ice shelf processes in the years to come.

Intermittent and variable rift propagation in the Amery Ice Shelf: In Chapter 4, we focused solely on the five rifts at the front of the Amery Ice Shelf in East Antarctica. This focus was motivated by the observations noted in Chapter 3 that the Amery Ice Shelf is uniquely active among the ice shelves of Antarctica. We described observations of the propagation of the five rifts over the past decade (2002-2012). And so, with this study, we delved deeper into the possible causes and mechanisms at work in this location that contribute to such activity. Our work expands on a study completed by *Fricker et al.* (2005), and is novel in that it presented a decadal observational dataset for the Amery Ice Shelf. We used satellite imagery to observe rift propagation in the five interacting rifts. While we did not find any strong correlation between temperature fluctuation or ocean swell and rift propagation, we were able to link the unique front-initiated geometry of the rifts to increased sensitivity to tsunamis. Our dataset can continue to be amended in the future and serves as a benchmark upon which we can compare future activity.

Implications for rift propagation in highly-fractured ice at Enceladus and Europa: In Chapter 5, we presented amendments to current models of fracture penetration models in planetary ice shells. Most current models of fracture penetration in icy shells (a) consider fractures are singular, isolated features and (b) do not consider basal crevasses. We applied our observations of the interaction of closely-spaced rifts and crevasses in the Amery Ice Shelf (Chapter 4) to the highly-fractured shells of Enceladus and Europa by modeling fracture propagation in a structurally-compromised shell, i.e., the propagation of a fracture among a field of pre-existing crevasses. We showed that the current singular models of fracture propagation under-

estimate the stresses required at the surface to fully penetrate the shell. We suggest that either larger stresses or smaller ice thicknesses are required to do so. Additionally, we show that basal crevasses at the ice-ocean interface may become water-filled and facilitate the propagation of multiple cracks from the bottom of the shell, and may increase the likelihood of full shell penetration to allow sub-surface material to escape.

The formation of a rift basin at the south pole of Enceladus: In Chapter 6, we developed a theory and model for the formation of the large rifted depression known as the South Polar Terrain at the south pole of Enceladus based on terrestrial rift basin processes. In this study we applied three basin formation models (lithospheric thinning, extension, and compression) to investigate the possibility that the SPT depression and surrounding mountainous region near the SPT may have formed in a manner similar to that of a basin on Earth. Comparing predicted topography from our models to estimates of topography by previous studies for both subsidence of the basin floor and footwall uplift at the boundary, we conclude that an extensional mechanism with flexural uplift provides a consistent explanation for the formation of the SPT. We completed all of these models in spherical geometry, although most models of Enceladus tectonics thus far have employed a Cartesian approach. We showed (in an Appendix to that work) that the consideration of the spherical geometry significantly affected the outcome.

7.2 Contributions

With the work carried out as summarized in this dissertation, our contributions can be considered to be as follows:

1.) We have compiled the most extensive dataset of rift propagation to date over 13 of Antarctica's ice shelves, and shown that while variable, rift behavior generally falls into one of three categories: (i) completely dormant; (ii) consistent intermittent

propagation for two to ten consecutive years; or (iii) "sudden burst" propagation events. We could not find a geographic pattern to the rift propagation activity, suggesting that local temperature fluctuations may not play a large role in the modulation of ice shelf rifting.

2.) In our Antarctic-wide survey, we discovered that the Amery Ice Shelf is currently unique among other ice shelves, given that all five of the rifts within 30 km of its front are actively propagating; only one has stopped propagating (prior to our observation period). We postulate that this is due to the fact that it is approaching its position prior to its last large calving event in 1964/65. As it does so, it tears itself apart as it spreads radially over the ocean. We hypothesize that it will likely undergo another large calving event in the next decade or so.

3.) We have corroborated the previous hypothesis by *Bassis et al.* (2007) that short-term environmental variables have very little effect or control over the propagation of rifts at the Amery Ice Shelf. This finding indicates that the primary drivers behind rifting are internal glaciological stresses in the ice shelf. While this has been hypothesized previously, we have shown that over a decadal timescale, the rifts remain insensitive to environmental variables like temperature fluctuations and ocean swell.

4.) We have observed the effect of tsunamis on front-initiated rifts in the Amery Ice Shelf and elsewhere. This is novel in that we have connected extreme solid-Earth events to the propagation of rifts in Antarctica, and in some cases, these events have led to the calving of icebergs. We showed that the Amery Ice Shelf's position in the path of tsunamis that originate in the Sumatra region often results in runup there on the average order of 5 cm. Elsewhere, we observed calving events that may be associated with the arrival of tsunamis: the calving of a an iceberg from the Larsen C ice shelf between following the 26 December 2004 Sumatra tsunami and from the Abbott Ice Shelf following the 11 March 2011 Honshu tsunami are two examples. All

of the rifts that we observed to be affected by tsunami runup (demonstrating either propagation or iceberg isolation) were front-initiated rifts. We have shown that front-initiated rifts are susceptible to tsunamis due to the pressure impulse imparted by wave impact on the rift walls.

5.) We have shown that nearby rifts at the front of the Amery Ice Shelf interact. Some pairs propagate in tandem, while others are anti-correlated and seem to engage in a trade-off of stress. We suggest that this interaction may facilitate the increased level of activity that we observe at the Amery with respect to other shelves. We have also demonstrated that, even among the closely-spaced rifts, once a rift stops propagating and become dormant, it is not easily re-activated. Especially in the case of rift E3, it propagates among dormant crevasses that are only "re-activated" when rift E3 propagates along one, rather than continuing to propagate themselves as they advect towards the front.

6.) We have demonstrated that current models of fracture propagation and tidal opening of cracks at the icy moons underestimate the magnitude of stresses required to do so, or overestimate shell thicknesses, by modeling fracture propagation in the more realistic setting of a highly-fractured shell rather than a pristine, homogenous shell. Additionally, we have discussed the possibility that basal crevasses may form at the ice-ocean interface and become water-filled, thereby making the complete rupture of the shell more feasible, even in the multiple-fracture case.

7.) We have developed a new theory for the formation of the bizarre south polar terrain at Enceladus that agrees with current estimates of topography. The work is novel in that not only does it approach the formation of the active region on Enceladus upon a comparative planetology platform, it approaches the formation of the bizarre terrain region as a whole, rather than simply focusing on parts; previously published material has focused on the formation or activity of particular features within the region, rather than treating the features as linked phenomena within one

model or description. By introducing the comparative planetology platform we show that similarly complex regions are found on the Earth and can be the result of similar mechanisms.

7.3 Future Work

Overall, the work presented here sought to advance the field of comparative cryospheres, combining the observation of rifting in Earth's ice shelves with observations of the surface morphology of the icy moons of the solar system. While we have achieved answers to the questions set out in the introduction of this dissertation, further investigation of the overlap between terrestrial glaciology and planetary ice will only improve upon the results we found as described here.

Our observations of rift propagation over the past decade serve as a good starting point for the continuation of rift monitoring. Continuing to monitor rifts around Antarctica into the next decade will supply us with rift propagation data over increasingly long timescales, with which we can compare records of environmental changes to determine possible longer-term effects. Additionally, we only observed one ice shelf that is likely close to a large calving event (the Amery Ice Shelf); as time goes on, others will approach their critical front positions. It will be an intriguing long-term observational study to see if an ice shelf's propagation activity increases as it approaches its final calving position. In that case, it could be possible to attribute higher activity level as a precursory signal of a large calving event. Further rift monitoring is essential to the advancement of a longer-term understanding of the role of ice shelf rift propagation. Another avenue to pursue in this vein is the activation or re-activation of crevasses. We observed at the Amery Ice Shelf that crevasses that had advected from upstream not re-activate as they approached the calving front. However, a future study would closely monitor the evolution of crevasse fields on a variety of ice shelves. It may be that crevasses alter the stress field enough to lead to

the arrest of a propagating rift or negate the initiation of a new rift altogether until stress is great enough.

Our conclusion that the highly-fractured shells of the icy moons make it more difficult for a fracture to fully penetrate the shell was based on our initial linear elastic fracture mechanics approach. While this first-order model is currently the norm for planetary models, it will be necessary in the future to further the investigation by modeling the full dynamic fracture mechanics of the propagation. For the sake of comparison with previous models, our approach is sufficient but does not fully describe the dynamics of the phenomenon. In that vein, it will be beneficial to investigate the formation of basal crevasses at the ice-ocean interface of the ice shells. While currently a controversial hypothesis that such crevasses could form in the ductile ice at that interface, showing that stress at the base of the shell are sufficient for such features to form would lead to significant modification of current models of feature formation at the icy moons.

In our investigation of extension and compression of Enceladus' shell in the formation of the SPT, we migrated a model of terrestrial ice to the moon for further testing. The model was developed to accomodate the fact that highly crevassed ice may behave more like a granular material than a simplified rectangular slab of ice, and therefore was prime for an application at the icy moons. While it is conceptual in nature, it has been calibrated with remotely-sensed observations and Antarctic field data, and the yield strength envelope we employ correlates with laboratory measurements of terrestrial ice. The model is based on "molecular dynamics"; it is based upon the dynamics of the "atom" and "molecules" (atoms held together by bonds). The atoms and molecules of ice interact through three set parameters: elasticity, friction, and bond strength. Contrary to other models of ice shelf stability, in addition to models of fracturing and rifting in rock and fracture penetration in the icy moons, this model allows us to consider the fact that the ice is heavily fractured and thereby

structurally compromised. We have conducted preliminary studies in the adaptation of the model to compressional and extensional features in a 2D-ice shell at Enceladus and presented said work at two conferences, but have yet to complete it. The continuation of this work would lead to improved constraints on the mechanisms driving feature formation on the icy moons. The novelty in the use of this model at the icy moons, and in fact in the use of any terrestrial ice dynamics model at the moons, is that ice shelves and sheets on the Earth are generally in extension. There are few places on the Earth in which ice is found to be compressed as it is on the moons. Hence, we are presented with a thought experiment of marrying two ideas: the dynamics of glaciology and orogeny. There are two modes in which we can conceptually approach designing a compressional experimental setup. The basic approach assumes one thin viscous layer representing the ice crust of Enceladus with an overlying thin weak semi-brittle layer. In the first model setup, we can assume horizontal flow in a subsurface layer creates a conveyor belt like velocity at the base of the viscous layer, driving the flow outwards due to convection or other cause. This leads to vertical shear within the overlying crustal layer and begins to form a basin at the center point of motion and pile-up of material at the edges. The second model involves the same layer model, but this time we impose a horizontal velocity through the entire crust (simulating some large-scale tectonic compressional force, perhaps analogous to the opening of the tiger stripes) on one side of the model and impose a zero-velocity "wall" at the other end of the domain, into which the moving icy material flows and builds upwards as a result. In these two model designs, we determine the resulting topography and subsequently compare it to observations of the SPT in order to determine constraints on various parameters, most importantly surface velocity and topographic height.

Aside from modeling compressive failure and extensional faulting in the ice of Enceladus, this model will also be useful in studying other features found on the

moons and placing constraints on the physical properties necessary to support their formation and maintenance. In particular, intriguing applications for our proposed future work include: the formation and stability of the chaos regions of Europa; effects of thinned areas of the ice shell; Iapetus landslide features; the extensional rifts and bright regions on Ganymede; tidal modulation of ice shelves and icy moons and associated hydro- and fatigue-fracturing; and the development of a spherical granular model for application at the icy moons and to contribute to the study of the dynamics of a Snowball Earth.

We have made some contributions to the emerging field of comparative cryospheres, and intend to continue to do so through the further development of models like the one described above and continued observations of rifting in terrestrial ice. Through remote sensing observation, field work, and modeling, we can construct a "virutal field study" of ice dynamics at the icy moons. Being a relatively young field, there are many promising directions for future research.

APPENDICES

APPENDIX A

Consideration of the Spherical Shell in Tectonic Problems

A.1 The flexural model in a spherical shell

The work showcased in Chapter 5 on the formation of a basin at the SPT of Enceladus required us to consider the application of geophysical expressions in a spherical frame rather than a Cartesian one. We summarize our formulation of flexure in the spherical shell here, and in the next section compare our spherical results with those acquired in the equivalent Cartesian formulation to showcase the differences between the cases.

A.1.1 Flexural formulation

Idealizing Enceladus as a spherical shell, the flexure equation on a sphere can be written as the sixth-degree partial differential equation (*Turcotte et al.*, 1981)

$$D\nabla^6 u_r + 4D\nabla^4 u_r + EhR^2\nabla^2 u_r + 2EhR^2 u_r = R^4\left(\nabla^2 + 1 - \nu\right)p \qquad \text{(A.1)}$$

where h is the thickness of the shell, R is the radius of curvature, E is Young's modulus, ν is Poisson's ratio, and where D is the flexural rigidity, defined as

$$D = \frac{Eh^3}{12(1-\nu^2)} \tag{A.2}$$

Equation (A.1) can alternately be written (*Beuthe*, 2008; *Sandwell and Schubert*, 2010) as

$$\begin{aligned} \eta D\nabla^2\nabla'^2\nabla'^2 u_r + FR^2\nabla'^2\nabla'^2 u_r + EhR^2\nabla'^2 u_r \\ +R^4(\nabla^2 + 1 - \nu)\Delta\rho g u_r = R^4(\nabla^2 + 1 - \nu)q_0\partial(\phi) \end{aligned} \tag{A.3}$$

where F is the end load on the shell, q_0 is the point vertical load applied at ϕ, and ϕ is the polar angle (or co-latitude). We define η as in *Sandwell and Schubert* (2010) as

$$\eta = \frac{12R^2}{12R^2 + h^2} \tag{A.4}$$

In Equation A.3, the differential operators ∇^2 and ∇'^2 are given by

$$\nabla^2 = \frac{1}{sin\phi}\frac{\partial}{\partial\phi}(sin\phi\frac{\partial a}{\partial\phi}) \tag{A.5}$$

and

$$\nabla'^2 = \nabla^2 + 2a \tag{A.6}$$

where a, in both cases, serves as a placeholder for the subject of the operator. *Beuthe* (2008) shows that these equations stem from a balance of forces. Assuming a symmetric shell as in *Tanimoto* (1998), we can define a balance of forces in spherical coordinates as

$$\frac{1}{sin\phi}\frac{\partial}{\partial\phi}(sin\phi\bar{\sigma}_{r\phi}) - \bar{\sigma}_{\phi\phi} - \bar{\sigma}_{\psi\psi} = -\frac{R}{h}f_r + \frac{R}{h}\Delta\rho g u_r \tag{A.7}$$

$$\frac{1}{sin\phi}\frac{\partial}{\partial\phi}(sin\phi\bar{\sigma}_{\phi\phi}) + \bar{\sigma}_{r\phi} - \bar{\sigma}_{\psi\psi}cot\phi = 0 \tag{A.8}$$

$$\frac{1}{sin\phi}\frac{\partial}{\partial\phi}(sin\phi M_{\phi\phi}) + Rh\bar{\sigma}_{r\phi} - M_{\psi\psi}cot\phi = 0 \tag{A.9}$$

with ϕ the polar angle (or colatitude) as above and ψ the azimuthal angle (or longitude) and f_r is the vertical line load acting at $\phi = \phi_0$. Equations (A.7), (A.8), (A.9) represent the force balance in r, ϕ, and moment balance about a constant colatitude (*Timoshenko and Woinosky-Krieger*, 1959; *Tanimoto*, 1997), respectively. $\bar{\sigma}$ represents the depth-averaged stress over the shell thickness. u_r is the vertical displacement in the radial direction (deflection) as defined previously in the main text. As we will simplify our problem by ignoring azimuthal variations, then from *Beuthe* (2008), the stress component can be written

$$\bar{\sigma}_{\phi\phi} = \frac{E}{1-\nu^2}(\varepsilon_{\phi\phi} + \nu\varepsilon_{\psi\psi}) \tag{A.10}$$

where ε is the extensional strain. This can be related to the displacement as

$$\varepsilon_{\phi\phi} = \frac{u_r}{R} + \frac{1}{R}\frac{\partial u_\phi}{\partial\phi} \tag{A.11}$$

and

$$\varepsilon_{\psi\psi} = \frac{u_r}{R} + \frac{cot\phi}{R}u_\phi \tag{A.12}$$

The bending moments $M_{\phi\phi}$ and $M_{\psi\psi}$ are related to the curvature of the shell and can also be expressed in terms of the displacement.

$$M_{\phi\phi} = \frac{D}{R^2}\left[\left(\frac{\partial^2 u_r}{\partial\phi^2} - \frac{\partial u_\phi}{\partial\phi}\right) + \nu\left(\left(\frac{\partial u_r}{\partial\phi} - u_\phi\right)cot\phi\right)\right] \tag{A.13}$$

and

$$M_{\psi\psi} = \frac{D}{R^2}\left[\left(\left(\frac{\partial u_r}{\partial\phi} - u_\phi\right)cot\phi\right) + \nu\left(\frac{\partial^2 u_r}{\partial\phi^2} - \frac{\partial u_\phi}{\partial\phi}\right)\right] \tag{A.14}$$

Since the vertical displacement that we seek should be of the spheroid vector form, then we can expect it to have the form (*Tanimoto*, 1997; *Sandwell and Schubert*, 2010)

$$u_r = \sum_{l=0}^{\infty} U_l P_l(cos\phi) \tag{A.15}$$

and

$$u_\phi = \sum_{l=1}^{\infty} V_l \frac{dP_l}{d\phi} \tag{A.16}$$

Employing (for now) the asymptotic solution found in *Tanimoto* (1997), assuming that a downward line force loads the shell at $\phi = \phi_0$ (axisymmetric), we can write the full solution for the vertical deformation u_r using the asymptotic formula for Legendre polynomials as

$$u_r = -A \left(\frac{sin\phi_0}{sin\phi} \right)^{1/2} exp(-\alpha(\phi - \phi_0)) x (cos\alpha(\phi - \phi_0) + sin\alpha(\phi - \phi_0)) \tag{A.17}$$

Here, A is a conglomerate of parameters:

$$A = \frac{R^4}{2\sqrt{2}Dk^3} F_r \tag{A.18}$$

and α can be expressed as $\frac{k}{\sqrt{2}}$. In these expressions, k is defined as (*Tanimoto*, 1998)

$$k^4 = \frac{12(1-\nu^2)R^2}{h^2}(1 + B_E) \tag{A.19}$$

where B_E represents the buoyancy ratio between the elastic crust and the viscous layer below it:

$$B_E = \frac{\Delta\rho g h}{E} \left(\frac{R}{h} \right)^2 \tag{A.20}$$

More fully, we can also write the complete solution using Legendre Polynomials as

$$u_r = -\frac{R^4}{D} F_r \sum_{l=0}^{\infty} \frac{\left(l + \frac{1}{2}\right) sin\phi_0}{G(l)} P_l(cos\phi_0) P_l(cos\phi) \tag{A.21}$$

Here, we have defined $G(l)$ as in *Tanimoto* (1997):

$$G(l) = \left[L^2 - (1-\nu)L\right]\left(1 - \frac{V_l}{U_l}\right) + 12(1+\nu)\frac{R^2}{h^2}\left(2 - L\frac{V_l}{U_l}\right) + \frac{\Delta\rho g R^4}{D} \qquad \text{(A.22)}$$

where V_l and U_l are Legendre coefficients and their ratio can be simplified, as shown in *Tanimoto* (1997), and written

$$\frac{U_l}{V_l} \approx \frac{l(l+1)}{(1+\nu)} \qquad \text{(A.23)}$$

Applying this flexural model to Enceladus' ice crust requires specification of various ice parameters as well as the magnitude and nature of the deforming load (F_r) applied to the shell. In each of the three basin models used in this study, F_r will be defined as a load in the radial direction that impinges on the shell. Using the flexure to determine the stress within the shell, it is possible to determine the point at which the shell is likely to break (using an assumed value for the strength of ice).

A.1.2 Comparison of spherical shell flexure to Cartesian geometry

Enceladus has a small radius of curvature, and we therefore adopted a spherical geometry with which the deformation was modeled. In the interest of comparison, we present the Cartesian results of the models described in the text.

In the application of the compressional model of *Bullard* (1936), we find flexure y as a function of distance x away from the plate break using the broken elastic plate solution to find a maximum uplift of roughly 0.5 km. This an order of magnitude less than our results (computed in a spherical geometry) of 1.15 km. It could be that the difference can be attributed to stresses due to the curvature of the shell adding to the compressive force in the spherical model.

In the case of the extension model of *Vening-Meinesz* (1950), we use the Cartesian geometrical set-up by *Watts* (2001), which we had adapted to spherical form,

to determine the uplift by finding the force on the block and applying it to the end of a broken plate. In this case, we find a total uplift, assuming a 20° fracture, of approximately 0.6 km. This is about one-third of our lowest results in the spherical formulation, which is to be expected from our geometric approach. The difference between flexure results likely arises from the application of the spherical flexure formula which incorporates stresses due to the curvature of the shell into the results.

A.2 Effects of bending moment and membrane forces on stress intensity factors in spherical ice shells

In Chapter 4 we discussed the contribution of different stress scenarios to the stress intensity factor and therefore the propagation of a fracture in the ice shell. Due to the small radius of curvature of Enceladus, it might be relevant to calculate the stress intensity contributions from the membrane and bending stresses in the shell. We describe our spherical formulation of the stress intensity factors due to bending and membrane stresses here.

An additional scenario to consider is that planets with smaller radii should be considered in the spherical case rather than subjected to the Cartesian treatment. Planets on the scale of Earth are large enough with respect to features such as fractures that studies of these surface features can be simplified by assuming a Cartesian geometry. However, Enceladus is small enough (radius ≈250 km) that its spherical shape may affect results if not taken into account (*Walker et al.*, 2012). Therefore, assuming a crack has penetrated the shell, we discuss the affects of bending and membrane stresses on horizontal crack closure. In theory, if the ice shell of Enceladus (or Europa) is approximated as a thin spherical shell, we can determine the stress intensity factors due to bending and membrane stresses on a through-crack. *Delale and Erdogan* (1979) analyzed this problem using previous studies by *Green* (1962);

Reissner (1969), who linearized shallow shell theory, to reduce the problem to the expressions:

$$\int_{-1}^{1} \frac{g_1(\tau)}{\tau - \eta} d\tau + \int_{-1}^{1} \left[k_{11}(\eta, \tau) g_1(\tau) + K_{12}(\eta, \tau) g_2(\tau) \right] d\tau = 2\pi F_1(\eta) \tag{A.24}$$

and

$$\frac{1 - \nu^2}{\lambda_0^4} \int_{-1}^{1} \frac{g_2(\tau)}{\tau - \eta} d\tau + \int_{-1}^{1} \left[k_{21}(\eta, \tau) g_1(\tau) + K_{22}(\eta, \tau) g_2(\tau) \right] d\tau = 2\pi F_2(\eta) \tag{A.25}$$

and $\int_{-1}^{1} g_i(\tau) d\tau = 0, (i = 1, 2)$. g_1 and g_2 are the derivatives of crack face opening displacement and the crack face rotation:

$$g_1(\frac{x}{a}) = \frac{\delta}{\delta x} \nu(\frac{x}{a}, 0^+) \tag{A.26}$$

$$g_2(\frac{x}{a}) = a \frac{\delta}{\delta x} \beta(\frac{x}{a}, 0^+) \tag{A.27}$$

where $\nu(\frac{x}{a}, 0^+)$ and $\beta(\frac{x}{a}, 0^+)$ represent the crack face displacement and the crack face rotation, respectively. Non-dimensional parameters γ_0 and γ are used to determine kernels k_{ij} in Eqs. A.24 and A.25 and are found by Eqs. (7.6-7.10) of *Delale and Erdogan* (1979) for an isotropic shell as:

$$\gamma_0^4 = 12(1 - \nu^2) \frac{a^2}{h^2} \tag{A.28}$$

and

$$\gamma = \left[12(1 - \nu^2) \right]^{1/4} \frac{a}{\sqrt{Rh}} \tag{A.29}$$

In Eqs. A.24 and A.25, F_1 and F_2 are the stress functions related to the membrane force and bending moment,

$$F_1(\frac{x}{a}) = -\frac{\sigma_{mem} \frac{x}{a}}{E} \tag{A.30}$$

and

$$F_2(\frac{x}{a}) = -\frac{\sigma_{bend}\frac{x}{a}}{6E} \tag{A.31}$$

Here, σ_{mem} and σ_{bend} represent the membrane and bending stress distributions along the prospective crack path. Positive stress denotes tension in the outer surface. Under a given geometry and loading condition, Eqs. A.24 and A.25 can be solved via the Gauss-Chebyshev integration method (e.g., *Theocaris and Ioakimidis* (1977)), outlined in Appendix A of *Liu et al.* (1999). *Delale and Erdogan* (1979) showed that the membrane and bending stresses around crack tips have the same angular dependence as those for plane extensional cracks, and so implied that the stresses in the region of the crack tip can be expressed in the same form as above in the (Eq. 2.1):

$$\sigma_{ij} = \frac{K_{mem} + \frac{2z}{h}K_{bend}}{sqrt2\pi r} f_{ij}(\theta) \tag{A.32}$$

where $(i, j) = (x, y, z)$ and functions f_{ij} are the same as in the elasticity solution (Sec. 2.2). In this case, K_{mem} and K_{bend} denote the stress intensity factors induced by the membrane and bending stresses, and are expressed as:

$$K_{mem} = \frac{-E\sqrt{\pi a}}{2} h_1(1) \tag{A.33}$$

$$K_{bend} = \frac{-E\sqrt{\pi a}}{2} \frac{h}{2a} h_2(1) \tag{A.34}$$

for a crack tip located at $x = a$. It can be noted that for a given fracture length, K_{mem} and K_{bend} depend only on parameters $\frac{a}{h}$ and γ. Of course, this formulation applies only to "shallow" cracks, those that have long lengths with respect to the radius of the shell. "Shallowness" can be expressed as the ratio between height d and cap diameter $2a$ (*Liu et al.*, 1999):

$$S = \frac{d}{2a} = \frac{R - \sqrt{R^2 a^2}}{2a} \tag{A.35}$$

It can also be expressed in terms of γ:

$$S = \frac{a}{2h} \frac{[12(1-\nu^2)]^{1/2} - \left[12(1-\nu^2) - \lambda^4 \frac{h^2}{a^2}\right]^{1/2}}{\gamma^2} \tag{A.36}$$

As discussed in *Liu et al.* (1999) (for example), the acceptable shallowness limit inside which linearized shallow shell theory applies is around $S = \frac{1}{8}$, though it has been shown through finite element analysis that stress intensity factors determined by the theory above remain reasonably accurate up to $S = \frac{1}{5}$. In the case of Enceladus, tiger stripe rifts are approximately 130 km in length. Determining the radius of the associated spherical cap to be $a = 71.6km$ and using a planetary radius of $R = 250km$, through Eq. A.35, we find that the tiger stripe rifts are sufficiently shallow for this method ($S = 0.073 \leq \frac{1}{8}$). In that case, the stress intensity factors at the ends tiger stripe rifts (assumed to be through-cracks to a subsurface reservoir) can be calculated by Eqs. A.33 and A.34 for varying rift lengths and shell thicknesses.

APPENDIX B

Bounds on Compressional Features in the Ice Shell of Enceladus

B.1 Introduction

The SPT of Enceladus is made up of several distinct features and terrain types, noted by *Gioia et al.* (2007) as the central tiger stripe terrain, which coincides with the underlying thermal anomaly at the South Pole; a slim circular terrain which surrounds the central tiger stripes but has no fractures of its own; and a prominent ring of ridges at the border. A fourth type of feature manifests itself as large rifts that extend northwards from the mountainous ring to the equator. In many past analyses, the features have been treated as separate quantities rather than analyzed as a coupled system. For instance, in the past it has been suggested that the tiger stripe terrain is a spreading center of sorts, with the tiger stripes themselves being the surface expression, similar to mid-ocean spreading ridges on Earth (e.g., *Parkinson et al.* (2008), *Abramov and Spencer* (2009), popular articles). Alternately, it has been suggested that horizontal surface motion arises from convection in the subsurface

warm ice which induces motion in frozen "mobile lids" at the surface (e.g., *Barr* (2008)).

Doubts arise as to whether or not horizontal spreading in the fashion of mid-ocean ridges occurs when the lack of compressional features between the stripes is observed. *Porco et al.* (2006) and subsequent papers have attributed the circular ridge boundary feature to compression (convergence), though no model has explicitly shown that such uplift by compression in the ice shell is occuring. Although the topographical evidence with regard to similar features on the Earth would suggest that the spreading scenario and consequent compression at the outer boundary makes sense, it is the aim of the work described here in particular to determine whether or not motion in the ice shell could form such a boundary feature.

B.2 Experimental regimes of crustal deformation

A new model of terrestrial ice was recently developed at Michigan (e.g. *Bassis and Walker*, 2011) to accomodate the fact that highly crevassed ice may behave more like a granular material than a simplified rectangular slab of ice. It was therefore primed for an application at the icy moons. While conceptual in nature, it has been calibrated with remotely-sensed observations and Antarctic field data, and the yield strength envelope we employ correlates with laboratory measurements of terrestrial ice. The model is based on molecular dynamics, based upon the dynamics of the atom and molecules (atoms held together by bonds). The atoms and molecules of ice interact through three set parameters: elasticity, friction, and bond strength. Contrary to other models of ice shelf stability, in addition to models of fracturing and rifting in rock and fracture penetration in the icy moons, this model allows us to consider the fact that the ice is heavily fractured and thereby structurally compromised. We have conducted preliminary studies in the adaptation of the model to compressional and extensional features in a 2D-ice shell at Enceladus (*Walker and Bassis*, 2011b,a), but

have yet to complete it. The novelty in the use of this model at the icy moons, and in fact in the use of any ice dynamics model, is that ice shelves and sheets on the Earth are generally in extension; there are few places on the Earth in which ice is found to be compressed as it is on the moons. Hence, we present a "thought experiment", marrying two ideas: the dynamics of ice and mountain-building (orogeny). Our model setup assumes one thin viscous layer representing the warmer lithosphere of Enceladus with an overlying thin brittle layer.

There are two modes in which we can conceptually model a compressional scenario. In the first model scenario, we assume horizontal flow in a subsurface layer creates a conveyor-belt-like drag velocity at the base of the viscous layer, driving the flow outwards, perhaps due to convection or other cause. This leads to vertical shear within the overlying crustal layer and begins to form a basin at the center point of motion and pile-up of material at the edges (shown in Fig. B.1). The second compressive model involves the same layer model, but this time we impose a horizontal velocity through the entire crust (simulating some large-scale tectonic compressional force, perhaps analogous to the opening of the tiger stripes) on one side of the model and impose a zero-velocity "wall" at the other end of the domain, into which the moving icy material flows and builds upwards as a result (shown in Fig. B.2). In these two model designs, we show that the overall topography of the icy mountain belt can be reproduced.

Alternately, *Gioia et al.* (2007) noted that the SPT may have formed after the section of icy crust at the south pole endured alternating compressive and extensional stresses over a long period. Setting the ice shelf model to float and allowing the walls to move apart, we illustrate the effect of an extensional regime, as in Figure 3, in which the extension occurs at the boundary of the SPT rather than within it. These results are also promising in that we observe a depressed region at the center and uplift at the sides (shown in Fig. B.3).

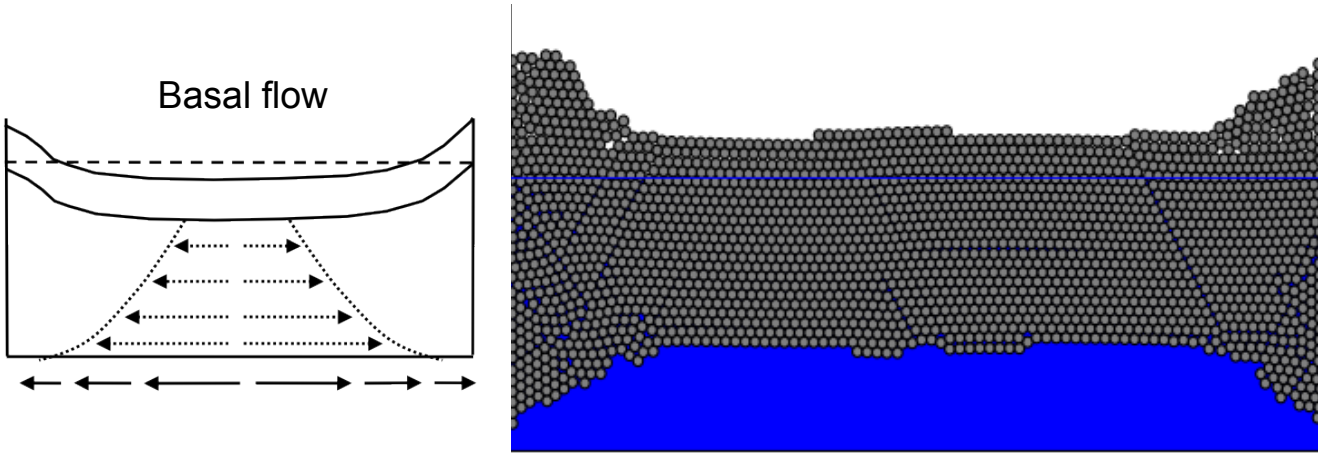

Figure B.1: A preliminary study: formation of mountainous ridges at Enceladus by basal flow into a backstop. Formation of desired topography (uplifted side walls and depressed center) and thinned region at center matches well with expected setting at the SPT.

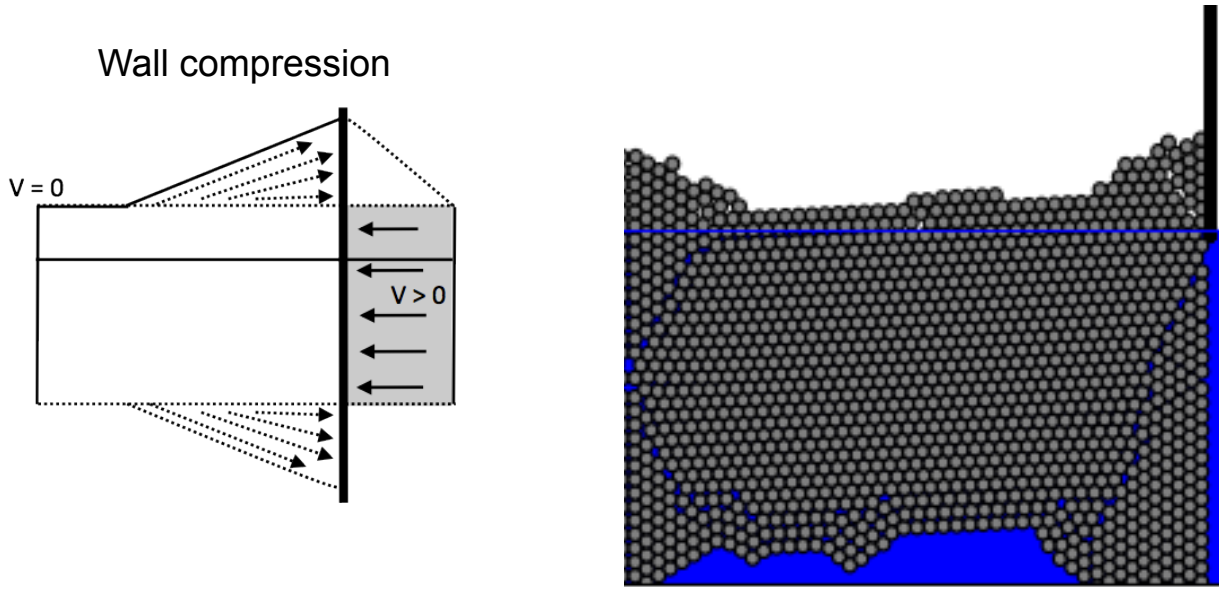

Figure B.2: A preliminary study: formation of mountainous ridges at Enceladus by collision of moving backstop and stationary ice (approximating far-field compressional tectonics). Formation of uplifted side walls and some depression at the center. Hill buildup at center is a remnant of our model geometry.

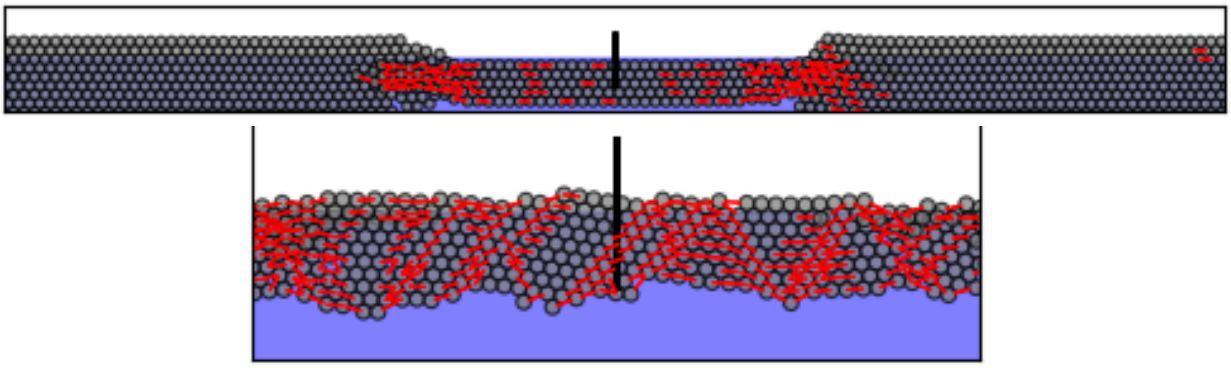

Figure B.3: Preliminary model application at Enceladus shows development of surface depression and mountainous ridges when extensional forces are applied to a thin brittle layer. Red symbolizes broken bonds, dependent on set ice strength. Inset (bottom) shows fractured ice in depressed region over localized ocean (zoomed view).

We note that these results are preliminary, and look forward to further developing this model (see Section 6.3, Future Work).

APPENDIX C

Laboratory Observations of Water Ice: Effect of Microstructure and Deformation Regimes on Anelasticity of Water Ice - Implications for Europa, Enceladus, and Titan

C.1 Introduction

Not only does ice exist in large ice sheets and glaciers here on Earth, but also on other planets, like Mercury and Mars, and in even larger quantities beyond the ice line. A majority of outer planet satellites - those of Jupiter, Saturn, Uranus, and Neptune - have outer shells comprised of ice.

The icy satellites of the outer planets generally have thick ice shells that, much like the mantle of the Earth, are subject to convective motion and tidal heating and dissipation. The understanding of these tidal processes plays an important part in the study of the geophysical, geological, and orbital evolution of these satellites. The investigation of tidal response in icy satellites will improve and/or enhance understanding of heat transfer mechanisms in geophysical models, internal dynamics of icy

shells (and additionally, ice sheets here on Earth), astrobiological potential at outer planet satellites, and help to interpret spacecraft data and to better plan and/or prepare for future missions.

Ice is dynamic. Not only can glaciers here on Earth be observed to flow down a mountainside - ice shells of the outer planet moons are subject to tides. How do we explain how ice flows, or "creeps"? Ice dynamics can be described with familiar descriptors to do with stress (forces acting on an object) such as compression, tension, and shear; and strain (a material's response to stress) such as rebound (or elasticity), viscosity, flow, rigidity, and fracturing. Forces that contribute to stresses on ice include gravity and tidal motions. It is necessary to understand the response of an ice shell to these stresses in order to further our understanding of heat dissipation in these satellites, and also to better understand the data that we see from outer planet exploration missions.

C.2 Theoretical Background

Most of the current models of planetary tidal heating use the Maxwell body theory to describe the response of the body to a tidal potential. The Maxwell body theory (e.g., *Maxwell* (1867)) describes the viscoelastic response of the material in the body as a function of its viscosity and rigidity. However, this theory does not account for multiple relaxation mechanisms or transient effects likely found in the planetary bodies of interest. Recently, laboratory measurements of ice creep as a function of stress have been undertaken to identify effects on attenuation by the different creep regimes (diffusion, dislocation, grain size, and basal slip) (e.g., *Goldsby and Kohlstedt* (2001); *Durham et al.* (2001)), and also other structural properties such as ice grain orientation, porosity, and partial melting, among others. Cyclic stress tests performed on planetary materials have demonstrated the fact that several relaxation mechanisms come into play, and the existence of transient behaviors in the material that are not

accurately described by the Maxwell theory. A literature review on rock anelasticity is found in *Efroimsky and Lainey* (2007), which shows that many laboratory studies demonstrated a frequency dependence of the friction coefficient between 10^{-4} and 10 Hz is such that $Q^{-1} \approx f^{-n}$, where n = 0.2 to 0.35. For a Maxwell body, the frequency dependence allows for n = -1.

There are not many measurements of the anelastic properties of ice (versus studies of rocky material), but those that do exist indicate that ice obeys the same frequency dependence as rock ($n \approx 0.2$ to 0.35). Though the Maxwell model provides a reasonable result in modeling attenuation at higher frequencies, the model cannot account for the transient mechanisms or different creep regimes known to exist in planetary icy shells. In the absence of relevant laboratory measurements, the Maxwell model has been extrapolated to the conditions found in outer planet satellites: tidal forcing frequencies between 10^{-5} and 10^{-7} Hz, tidal stress between 0.01 and 0.1 MPa, temperatures between 90 K and 273 K, and a range of compositions.

C.3 Laboratory Background

In recent years experimental work conducted at the Ice Physical Properties Laboratory at the NASA Jet Propulsion Laboratory has collected measurements of the viscoelastic properties of ice at tidal frequencies relevant to icy satellites such as Mimas, Europa, and Enceladus (among others). Results have been obtained for monocrystalline ice (dislocation creep-driven attenuation) using an *Instron* compression system modified to include cryogenic capabilities (described below). Results so far have intriguing implications for the modeling of the geophysical evolution of the icy satellites.

A completed project funded by the Michigan Space Grant Consortium during the summer of 2010 added to the current database of laboratory measurements of the attenuation properties of ice at conditions relevant to the icy satellites. We recorded

observations of ice with a larger grain size than had been previously observed, and focused on the grain boundary sliding regime of creep mechanisms. The addition of this new data set added to the existing data and to the building of a set of data important to the modeling of both planetary and terrestrial ice dynamics.

C.4 Theoretical Approach

C.4.1 Principles of the Experiments

Material attenuation can be expressed through the phase lag between the application of the stress (e.g., tidal stress) and the actual deformation of the object, both at laboratory- and satellite-scale. The experiment can be considered an analog to a damped harmonic oscillator driven by an external force (e.g., tidal attraction from the planet in the case of satellites, or the uniaxial cyclic loading in the case of our experiments).

If a periodic stress

$$\sigma = \sigma_0 e^{i\omega t} \tag{C.1}$$

of peak amplitude σ_0 and angular frequency ω is applied to an ice sample, the resulting strain of that sample at time t is expressed as

$$\varepsilon = \varepsilon_0 e^{i(\omega t+\delta)} \tag{C.2}$$

where ε_0 is the peak strain and δ is called the *phase lag angle* for mechanical relaxation. The decrease of energy per cycle ΔE_{diss} is given by *Hobbs* (1974):

$$\Delta E_{diss} = \int_0^{\frac{2\pi}{\omega}} \sigma \frac{d\varepsilon}{dt}\, dt = -\pi\sigma_0\varepsilon_0 sin(\delta) \tag{C.3}$$

The specific dissipation function Q of the material is defined by

$$Q^{-1} = \frac{-\Delta E_{diss}}{2\pi E} \tag{C.4}$$

ΔE_{diss} is the energy dissipated over one cycle and E is the total energy involved in that cycle. The parameter Q^{-1} is the internal friction coefficient, which can be expressed as (*Hobbs*, 1974):

$$Q^{-1} = tan(\delta) \tag{C.5}$$

The strain resulting from cyclic stress is anelastic because it takes a given relaxation time dt for the maximum strain to be achieved. Dissipation is due to the short-range motion of imperfections in the material, like lattice defects.

We performed sinusoidal stressing of our ice sample. During the first quarter of the cycle, elastic energy is stored in the sample. This mechanical energy is returned during the second quarter, but because of material inelasticity, viscous energy is lost during relaxation. The maximum strain achieved in response to cyclic stress is a function of the material elastic properties as well as a creep component whose contribution is a function of frequency. In our case, the creep component was the grain boundary sliding regime, and in our experiments, frequency varied between $3e^{-6}$ and 10^{-2} Hz.

C.4.2 The Andrade Model

In most cases, icy material under stress exhibits a transient, anelastic behavior not accounted for by the Maxwell description; from past experiments, it has been shown that models that include a broad relaxation term best approximate experimental data (*Jackson et al.*, 2002). Experiments have shown that there is a clear boundary between low-frequency and high-frequency regimes (Fig. C.1). This change in frequency dependence exhibits the differing process at work. At low frequencies, attenuation is dominated by viscous properties, and at high frequencies, attenuation is dominated

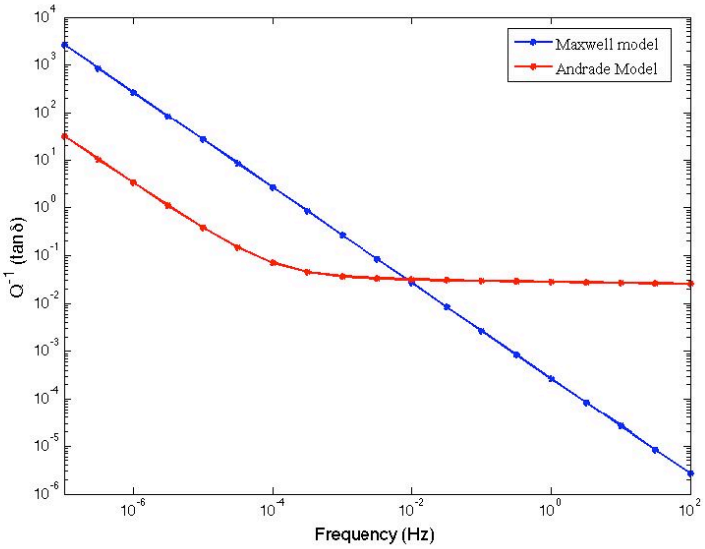

Figure C.1: Coefficient of friction (equivalent to the inverse of the dissipation factor) in ice as a function of frequency. This example employs an assumed grain size of 100 μm and a temperature of 240 K to show the difference in phase lag response predicted by the Maxwell model (blue) and the Andrade model (red). Note the change in frequency dependence between the models and the "elbow" behavior predicted by the Andrade model.

by anelastic properties. The "parabolic law" introduced by *Andrade* (1910) has been the most frequently reported match for many different materials. The creep function corresponding to the Andrade model is expressed as

$$J(t-t') = \frac{1}{\mu}\Theta(t-t') + \beta(t-t')^{\alpha} + \frac{1}{\eta}(t-t'), \tag{C.6}$$

μ is the unrelaxed shear modulus, η is the steady-state viscosity, and α and β are empirical parameters. Parameter α describes the duration of the transient response of the primary creep mechanism, and is dependent upon the stress and relaxation time of the dominant friction mechanism (*Castelnau et al.*, 2008). Parameter β is dependent upon temperature, frequency, and chemical composition, in addition to geometrical distribution and density of defects in the structure, and ultimately characterizes the amount of defects responsible for relaxation.

It has been observed in experiments, such as those practiced by *Castelnau et al.*

(2008); *Castillo-Rogez et al.* (2009), that water ice follows the same "elbow" law (i.e., frequency dependence) with the parameter α having similar values to those used for rocks. Specifically, fitting creep measurements has shown that the Andrade model best describes the observations. The complex compliance for a material obeying the Andrade model is given by (*Castillo-Rogez et al.*, 2011):

$$\bar{J}(\chi) = \frac{1}{\mu} - \frac{i}{\eta\chi} + \beta(i\chi)^{\alpha}\Gamma(1+\alpha) \tag{C.7}$$

where χ is the frequency. This leads to an expression for the phase lag (*Nimmo*, 2008):

$$Q^{-1} = tan\delta = -\frac{Im(\bar{J})}{Re(\bar{J})} = \frac{(\eta\chi)^{-1} + \chi^{-\alpha}\beta sin\left(\frac{\alpha\pi}{2}\right)\Gamma(\alpha+1)}{(\mu)^{-1} + \chi^{-\alpha}\beta cos\left(\frac{\alpha\pi}{2}\right)\Gamma(\alpha+1)} \tag{C.8}$$

Castillo-Rogez et al. (2011) have observed this behavior in the lab and demonstrated that the Andrade model provides the better fit. Fig. C.1 shows the departure from the Maxwell model of the friction coefficient Q^{-1} as determined using the Andrade model. Fig. C.2 shows the sine of the phase lag δ as a function of frequency, which shows the change in frequency dependence of the Andrade model from the Maxwell model, i.e., a noticeable feature in the Andrade curve is the changing slope at mid-frequencies in this plot.

Figs. C.3 and C.4 show phase lag as a function of frequency and temperature in ice for dislocation creep and grain boundary sliding regimes respectively, which demonstrate the behavior that we expected to see in our experimental results.

C.5 Experimental Approach and Methodology

The goal of the laboratory work concerned the inference of phase lag from our icy sample at various frequencies (attenuation spectrum) to be compared against the attenuation predicted by the Andrade model. And so, prior to lab work, it was

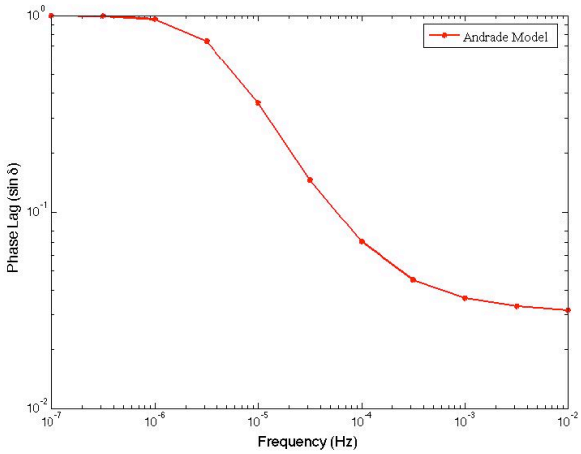

Figure C.2: Phase lag (sinδ) as a function of frequency according to the Andrade model. Viscous properties are dominant at low frequencies; anelastic properties become dominant at high frequencies. Note changing slope of the curve, characteristic of the Andrade attenuation spectrum.

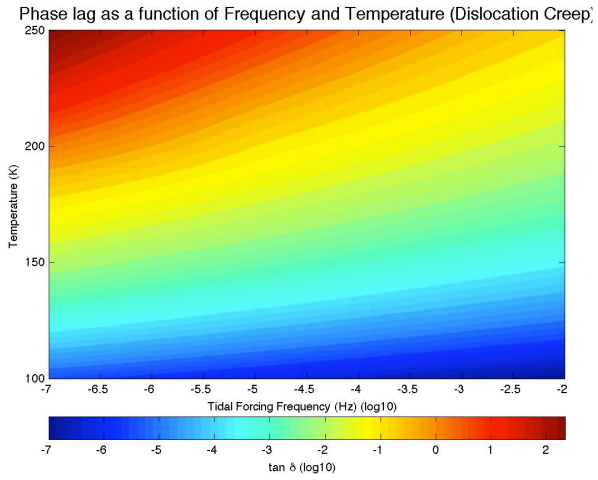

Figure C.3: Phase lag as a function of temperature and frequency as predicted by the Andrade approach. Red color indicates a larger phase lag, while bluer color represents smaller phase lag. Though similar in appearance, a noticeable difference here is the larger range of phase lag achievable in the dislocation creep regime (10^{-7} up to 10^{2}).

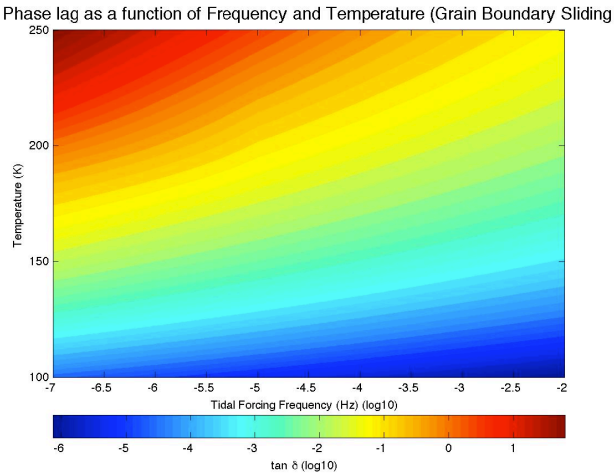

Figure C.4: Phase lag as a function of temperature and frequency as predicted by the Andrade approach. Red color indicates a larger phase lag, while bluer color represents smaller phase lag. Though similar in appearance, a noticeable difference here is the larger range of phase lag achievable in the grain boundary sliding regime (10^{-6} up to 10^{1}).

necessary and relevant to model the phase lag as predicted by the equations above. Using relevant tidal forcing frequencies and temperatures to the icy satellites, we were able to develop maps of phase lag as a function of temperature and frequency. Additionally, a "moon map" (Fig. C.5) was modeled in order to determine the creep regimes that may be encountered in the various moons. Each moon most likely undergoes more than one deformation regime, depending on what part of its ice shell is being considered, thus the map presented in Fig. C.5 focuses on the most representative regime. The results of these models are shown in Figs. C.3, C.4 and C.5. These models provide a baseline understanding of what to expect in our experimental results.

C.5.1 Physical Constraints

Earlier studies and experimentation in the Ice Lab at JPL have addressed the response of icy samples to stress in the dislocation creep regime. The goal of the 2010 summer work was to test the ice as the stress and temperature conditions force it

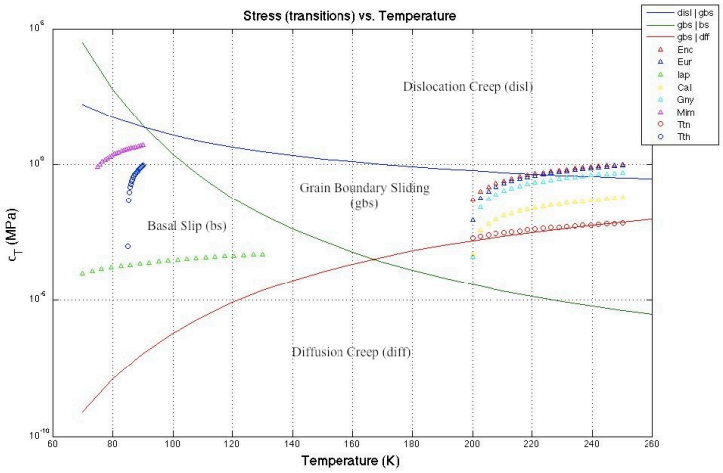

Figure C.5: Deformation map: Solid lines delimit conditions that promote various creep regimes. Dotted lines correspond to the conditions of tidal stress and temperature relevant to various icy moons in the solar system. This plot was obtained assuming a uniform grain size of 500 μm, and an assumed temperature of either the moon's surface temperature or, in the case of moons known to employ convection in their shells, a temperature of 200 K. Additionally, calculated tidal stress values based on orbital eccentricity were used to demonstrate the regime(s) that is likely occurring in each moon of interest.

to undergo deformation in the grain-boundary regime. Hence, as a first step, it was necessary to find the grain sizes, temperatures, and stresses that would make our lab tests relevant.

We started with the fact that earlier experiences in the lab provided that convenient temperatures with which to work were between 235 and 245 K. Next, we knew that the stress conditions we wanted to apply (and were feasible in the lab) were between 0.2 and 0.6 MPa. Hence, we could plug these variables into our model, and then determine what grain sizes would be most appropriate to achieve our science objectives. Fig. C.6 displays one of the plots we used to determine the grain size that would best approach our goals. The dotted vertical lines show the test stress, and each of the solid lines represents the transition between the dislocation creep regime and the grain boundary sliding regime. Notably, the red line, which represents the boundary for a grain size of 0.3 mm, is crossed nicely with the representative stresses. This led us to choose the 300 μm grain size.

C.5.2 Ice Factory Setup

It was determined that we would use a grain size of roughly 300 μm, and test the sample at approximately 240 K. To create the samples, we employed the cold room in the JPL Extraterrestrial Materials Simulation Laboratory. Set to -15°C, the room is complete with workbenches on which to create our samples. Pure, de-ionized water had been frozen in the storage cooler (-30° Celsius). We broke up and shaved down the solid blocks with a blender, and then used various sized sieves to sort out the ice particles into the required sizes. This process took approximately 45 minutes, during which we wore Personal Protective Equipment (PPE) that included parkas and winter gloves. After producing an adequate amount of ice grains at the requisite size, roughly 300 mL, we stored them in a beaker in the storage freezer in order to limit the sintering between particles.

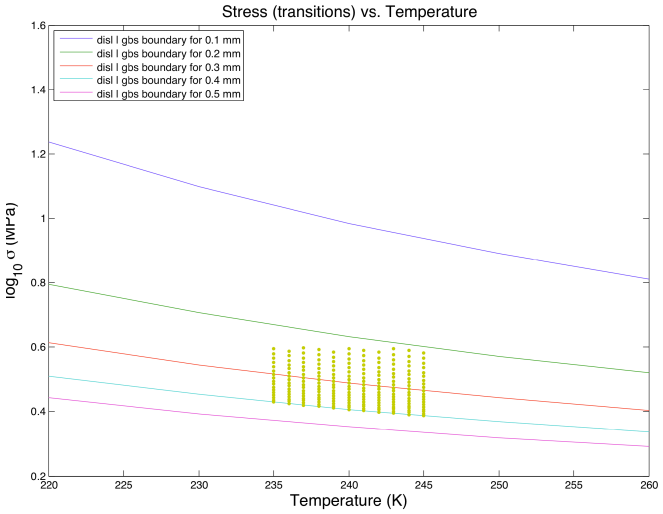

Figure C.6: Grain size determination: To determine which grain size to use for our sample, we used models like this one and constrained the possibilities to be between 235 and 245 K, and between 0.2 and 0.6 MPa. In limiting the grain size to be under 500 μm, we determined that 300 μm would work best, though such large sizes had not been tested in the lab before.

C.5.3 Compaction

The next step was to take the prepared ice seeds to the Ice Lab at the California Institute of Technology, where some of the JPL Ice Physics Lab equipment is located. We used a hydraulic press to compact the ice, with the intent of completely removing its porosity. Porosity within the sample would clearly affect the way the ice deformed, not to mention that the ice at the icy moons of interest is non-porous. A stainless steel cylinder with an approximately one-inch hole in the middle was loaded with the free ice particles, and then stamped down with a one-inch diameter steel rod that fit into the cylinder's center. This contraption was then loaded into a hydraulic press, surrounded by dry ice to keep the sample cold. Over a few hours, we compacted the ice by applying hydraulic pressure, careful not to increase pressure on the sample so much as to either induce too much pressure melting, or crack the sample. The rod started at approximately six inches above the lip of the cylinder, and by the end, was pushed all the way down. We carefully extracted the compacted ice, and had successfully prepared a roughly two-inch tall sample of non-porous pure water ice.

C.5.4 Tidal Stress Simulation Facility

This sample was then taken back to the JPL Ice Physics Lab where it was cut down with a band saw to ensure that the ends of the cylindrical ice sample were parallel and even for loading into the *Instron* instrument in the Tidal Stress Simulation Facility. The thin sections cut from the ends will be used to investigate microstructure effects with the cryogenic microscope. We loaded the sample into the *Instron*, which will apply stress at values we had previously determined through modeling.

The *Instron* system is equipped with a load cell, which allows loads up to 2 kN. For these compression studies, a cylindrical sample is placed between two platens. The bottom platen is fixed, while the top platen can be moved down to apply a given stress or stress rate, or a given strain or strain rate. The environmental chamber

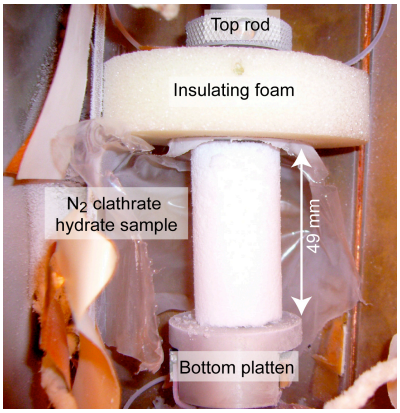

Figure C.7: A photo of the Instron system, in which the cylindrical ice sample is placed and tested through cyclical stresses from the top platen (this particular test concerned a clathrate sample).

in which the sample and platens are located can produce and control temperatures from 150 K up to ambient temperature. Data acquisition was performed with Labview software by Bluehill that was modified to provide a convenient user interface and automation capability. Data acquisition frequency ranges up to 5 kHz, which allows the measurement of phases down to an on the order of tenths of milliseconds.

The raw data acquired by the *Instron* system are the load exerted by the upper platen and measured by the load cell, and the upper platen vertical position, which provides information on the sample thickness, and thus its strain. Eight temperature measurements are acquired in order to characterize the thermal response of the system, and its impact on the measurements.

The sample is pressed between the two platens, as illustrated in Fig. C.7, within the cryogenic environmental chamber (small freezer) to keep it cold throughout the experiment, and subjected to cyclic loading that simulates tidal stressing (i.e., compression followed by expansion in a sinusoidal pattern). Our sample was subjected to a number of different frequencies between 10^{-2} Hz and 10^{-8} Hz, at an initial stress of 100 N with a cyclic stress of $\pm$50 N. Output data is analyzed using *Igor Pro* software.

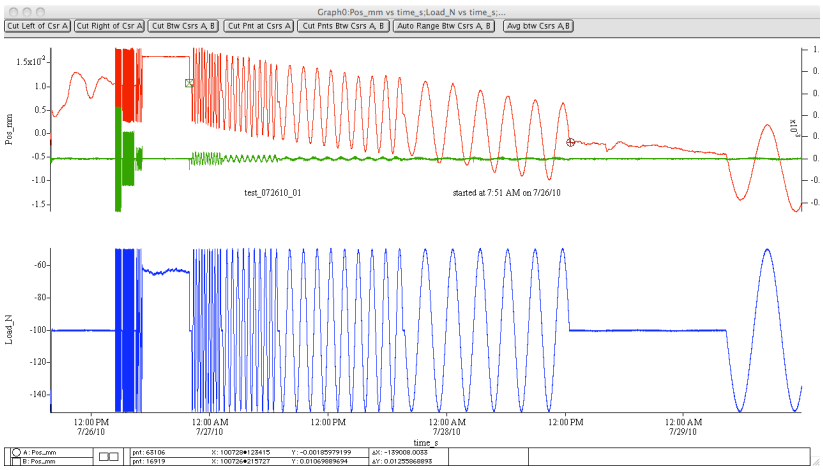

Figure C.8: A photo of the Instron system, in which the cylindrical ice sample is placed and tested through cyclical stresses from the top platen (this particular test concerned a clathrate sample).

C.6 Data Analysis

In order to infer the phase lag between the application of a load and the resulting vertical position change in the sample during the maximum compression stage, it is first necessary to load the data into the Igor Pro software. Once loaded, the number of points recorded and frequency can be found in the data. The raw position data clearly exhibits creep in most cases, which can be observed as the "tilted" appearance of the top plot (red, representing the position) in Fig. C.8, making it difficult to compare the curves, and therefore phase lag, directly.

Thus, it is necessary to take the derivative of both curves (Load and Position); from this process, we can then determine the zeros of the differentiated function, which clearly shows the lag between maximum load and maximum change in position. After differentiating, these rather noisy results are smoothed and then exported as a delimited data file.

The processed files are then subject to an automatic pointing process, which determines the average amount of lag between the load and position for each frequency. It is expected, based on theory discussed above, that the lag should vary with frequency.

Once these results are compiled, the set is then fit with the Andrade method.

C.7 Results

C.7.1 Experimentally-derived viscosity

In the scheme of things, it was necessary to infer the viscosity of the sample as input to the model used for fitting the attenuation spectrum. Inferring the viscosity through measurement is different than simply using the theoretical equations as found in the literature. In the literature, viscosity is commonly presented as (e.g., *Barr and Pappalardo* (2005)):

$$\eta = \frac{\sigma}{2\dot{\varepsilon}} \tag{C.9}$$

where σ is the stress and $\dot{\varepsilon}$ is the strain rate. Alternately, experimental results indicate that, as in *Durham et al.* (2001), viscosity can be expressed as:

$$\eta = \frac{1\overline{\sigma}}{3\dot{\varepsilon}} \tag{C.10}$$

Inferring a strain rate from our experimental results was fairly straightforward. By dividing the slope of the position curve by the height of the sample to ascertain the strain, we determined the strain rate by dividing this value by the change in time. This gave us the strain rate in units of s^{-1}. Then, plugging our strain rate into Eq. C.10, our experimentally derived viscosity was approximately 2.35×10^{13} Pa s, versus a predicted value from Eq. C.9 of 3.5×10^{13} Pa s, assuming a grain size of 150 μm, a strain rate of $2.8 \times 10^{-9} s^{-1}$, and a stress of 0.2 MPa.

C.7.2 Grain size: Expected vs. actual

As shown in Fig. C.5, we had originally prescribed grain sizes of approximately 300 μm in order to approach the regime boundary between dislocation creep and grain boundary sliding. In doing so, we used a grain size that had not been used before in the laboratory experiments, and therefore it was unknown how the grains would respond to compaction. We were unsure whether they would stay our requisite size, or if they themselves would be ground as a consequence of compaction to create smaller grains than we had planned. As it is a relatively new process with some uncertainty, it was not entirely unexpected that the grain sizes would change as they did (discussed below). When we began our *Instron* experiments, it became apparent that the supposed grain size had dropped by an approximate factor of 2. Hence, we did not approach the boundary between regimes as expected, but still gathered valuable data from our sample in the grain boundary sliding regime.

C.7.3 Microstructure

We used a cryo-microscope to investigate the microstructure of our sample. After the compaction process, we cut an approximately 1 mm thick slice from the end of our ice sample. This slice was then inserted into the cryo-stage of the microscope to ensure that the sample did not melt during observation. We were then able to investigate the slice of ice under varying magnifications in plane and polarized light (e.g., Fig. C.9). The computer-controlled microscope is linked to software which enables the user to measure the sizes of the ice grains, along with a statistical representation of all the grains in the image. It was also from these images that we confirmed the grain size being an average of 150 to 200 μm.

When the sample was extricated from the *Instron* system, we were able to investigate the changes that may have taken place during the many stress cycles. It was notable via the use of the microscope software that the grain sizes had not been

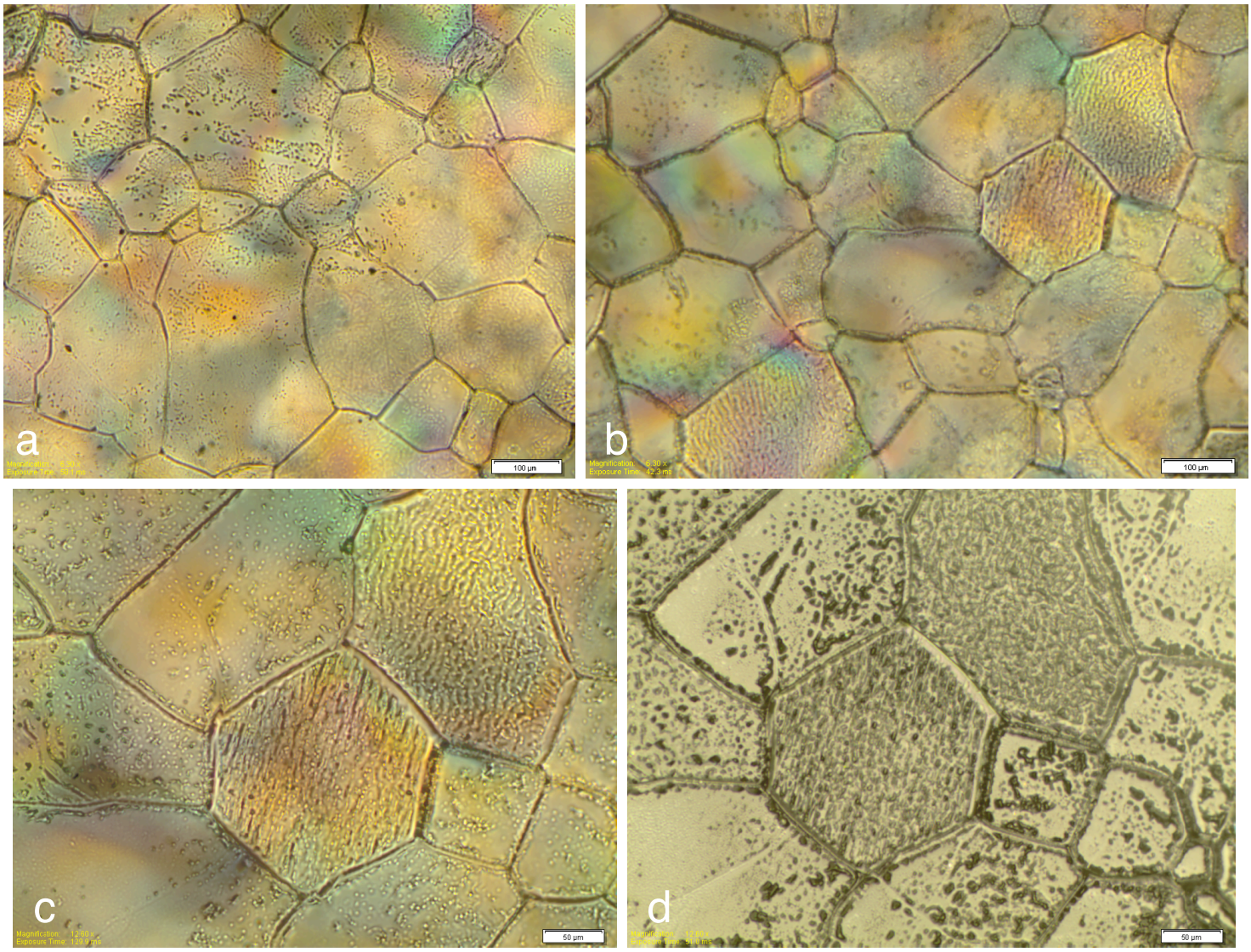

Figure C.9: Various captures taken by the cryo-microscope of the ice sample after compaction but prior to insertion into the Instron instrument. Lack of porosity and different grain sizes are observed. The sample featured an average grain size of 150 μm, +/- 50 μm. Figs. a-c were taken using a polarized light source and color represents changes in material. Figure (d) shows the same section as in (c) using reflected light. Notable here are the formation of small cracks (or sub-grain boundaries) in some of the larger grains (e.g., large grain at bottom left)

altered significantly from their original state. Also visible in the post-*Instron* images (Fig. C.10) are sub-grain boundaries that began to form due to the stresses applied. If stressed further, these sub-grain boundaries may have completely formed new grains. The post-stress images also look different from the pre-*Instron* images due to the fact that there was a certain amount of melting that occurred during transport from the freezer to the cryo-stage. This left a layer of melt and frost on the top of the sample, which made observation slightly more difficult than the pre-*Instron* observations. The apparent air bubbles do not represent porosity in the sample, rather melting on the surface. Another difference between the pre- and post-*Instron* observations was the thicknesses of the thin-slices in the cryo-stage. Though the first set of slices were cut using the band saw, and were therefore evenly cut and perfectly circular, the band saw was not available at the time of the post-*Instron* observations (due to another ongoing temperature-sensitive experiment in the Cold Room), so those slices were cut by hand using a razor blade. This caused the post-stress slices to be thicker and more like chips of ice in shape and not uniform in thickness. However, overall structure could still be observed using the microscope software to amalgamate various focused images at different thicknesses through the ice sample.

C.7.4 Data-model comparison: The Andrade Model

Once the data had been differentiated and smoothed, we then determined the points at which the Load and Position measurements underwent the maximum compression, found the difference, and thereby found the "lag" between application of the load and response in the sample. This lag was quantified as number of points in time. To determine the phase lag in degrees, by finding the sampling frequency for each frequency group and their respective periods, we could determine the phase lag by dividing 2π by the period and multiplying by the sampling frequency. We plotted the sine of our derived values for phase lag against frequency (Fig. C.11). Next, we

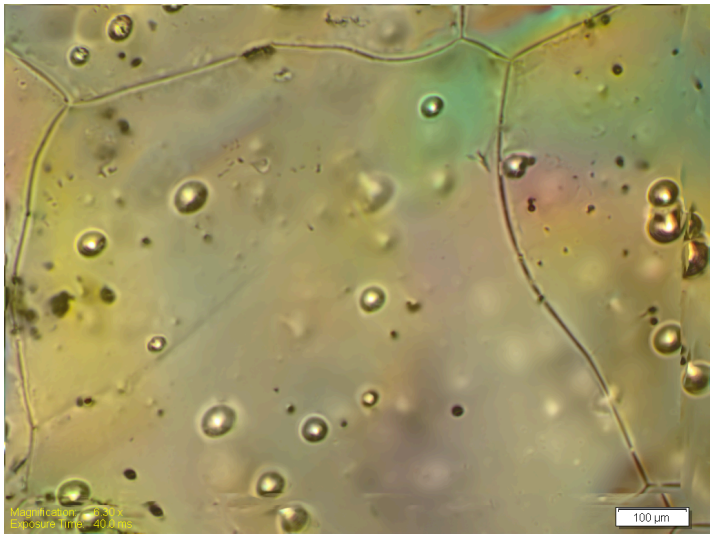

Figure C.10: Images of the post-Instron sample. Air bubbles are a product of melting that occurred during transport between the storage freezer and the cryo-stage. Images are composites of many focused images, as the sample had varying thickness across it. Some sub-grain boundaries can be observed in the larger grains, for example in the large grain at the top-left of (a), and the enlarged view of a grain featuring a sub-grain boundary formation in (c). Noticeable in all three images is the lack of porosity between grains, and for the most part, similar grain sizes as the pre-Instron images. These observations are consistent with past data sets.

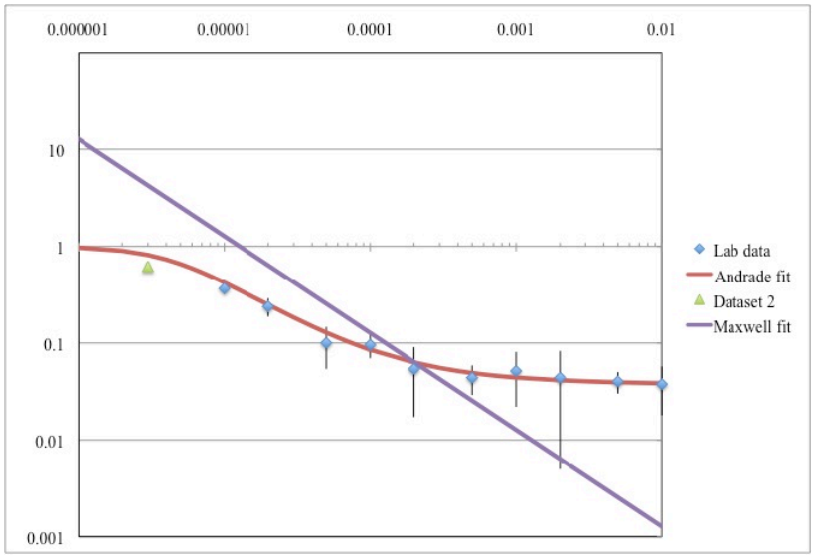

Figure C.11: Best fit of the Andrade model (red) to laboratory data collected in July-August 2010 (blue/green). Consistent with past data sets, it fits the data well at both high- and low-frequency. The Maxwell model (purple) does not fit the data as well as the Andrade curve, showing that our laboratory data supports the Andrade model.

fitted the Andrade model to our data by searching for the RMS between a theoretical fit based on Eq. C.8 and the laboratory data. We used a fixed value for viscosity (our derived value of 2.35×10^{13}), and varied values for the Young's modulus and parameters α and β within realistic bounds (e.g., Young's modulus between 1 and 10 GPa, since the value for polycrystalline ice is $\approx$5 to 8 GPa; α positive and less than 0.5). The best fit parameters were determined to be a Young's modulus of 2×10^9 (lower than predicted), α of 0.04, and β of 7×10^{-10} (Fig. C.11). Due to uncertainties, the fit slightly over-estimates the slope of the curve, though it is a fairly successful fit and consistent with past data sets.

C.8 Summary of Conclusions and Future Work

C.8.1 Conclusions

In order to gain knowledge of the dissipation processes within the icy satellites of the solar system, it is first necessary to conduct relevant experiments at the laboratory scale. As is the experimental process, it is prudent to conduct many sets of experiments to collect as many independent datasets as possible. This will allow for the fact that experimental work is exactly that; that is, the collection of many datasets accounts for the variability of behavior that may be observed.

The aim of the laboratory work conducted during the summer of 2010 was to contribute to a study of the attenuation properties of ice. Other experiments had already been conducted, and therefore this set of data would add to an existing dataset, and as such, also had a precedent with which to compare.

A unique experience was gained during the 2010 summer work in seeing an experiment through from beginning to end. Beginning with the creation of ice seeds from a block of pure deionized water ice, subjecting the resulting sample to relevant tidal stresses, and completing the project with inspection of data and physical effects on the structure after removal from the tidal facility, it was a nicely compacted project that was perfectly achievable in the allotted timescale.

After processing the raw data, specifically focusing on the Load and Position measurements from the *Instron* system, the measurements could then be compared to the model fits of the Andrade model and the Maxwell model. In this analysis, it was determined that the Andrade model is nicely supported by our experimental data. Furthermore, the data indicates that Maxwellian behavior is not supported by our experiment. Additionally, along with these overall results, the data also match well with the already existing datasets from the previous year. While investigating the sample's microstructure after exiting the *Instron* system it was observed that the grain

sizes did not change significantly, another feature that is correlated by past datasets. It was also possible to see sub-grain boundaries in the resulting sample, places where new grains would have formed if stress had continued to be applied. It was overall a successfully conducted experiment, both in terms of a learning experience and in terms of the resulting data.

C.8.2 Future work

With regard to future work, since the Planetary Tides Simulation Facility is the only one of its kind in the world, and the fact that these measurements are relatively new, more data must be obtained in order to gain full understanding of the processes driving attenuation in icy materials. The ultimate goal of the summer 2010 work was to add to the current knowledge database for mechanical properties of ice. Though these measurements and observations are at laboratory- and even microscopic-scale, they will soon have great implications for the understanding and modeling of the icy shells of the outer planet satellites. The next step is to make a new ice sample with different grain size and change the stress levels to which it is subjected. An interesting experiment to be conducted at some point in the future is that of approaching the boundary between deformation regimes in the ice, to observe the response in these conditions. First, however, it is necessary to conduct more experiments in the dislocation and grain boundary sliding regimes at a variety of conditions. The future amalgamation of these datasets shall be an excellent addition to the community in a new understanding of tidal dissipation and attenuation properties in planetary ices.

BIBLIOGRAPHY

BIBLIOGRAPHY

Abramov, O., and J. R. Spencer (2009), Endogenic heat from Enceladus' south polar fractures: New observations, and models of conductive surface heating, *Icarus*, *199*, 189–196, doi:10.1016/j.icarus.2008.07.016.

Allen, P. A., and J. R. Allen (2005), *Basin Analysis: Principles and Applications, 2nd Ed.*, 549-+ pp., Blackwell, Malden, MA.

Anderson, O. L., and P. C. Grew (1977), Stress Corrosion Theory of Crack Propagation With Applications to Geophysics (Paper 6R0573), *Rev. Geophys. Space GE*, *15*, 77, doi:10.1029/RG015i001p00077.

Andrade, E. N. D. C. (1910), On the Viscous Flow in Metals, and Allied Phenomena, *Royal Society of London Proceedings Series A*, *84*, 1–12.

Auzende, J.-M., R. N. Hey, B. Pelletier, D. Rouland, Y. Lafoy, E. Gracias, and P. Huchon (1995), Propagating rift west of the Fiji Archipelago (North Fiji Basin, SW Pacific), *J. Geophys. Res.*, *100*(9), 17,823–17,835, doi:doi:10.1029/95JB00612.

Barr, A. C. (2008), Mobile lid convection beneath Enceladus' south polar terrain, *J. Geophys. Res.-Planet*, *113*(E12), E07,009, doi:10.1029/2008JE003114.

Barr, A. C., and W. B. McKinnon (2007), Convection in Enceladus' ice shell: Conditions for initiation, *Geophys. Res. Lett.*, *34*(9), doi:10.1029/2006GL028799.

Barr, A. C., and R. T. Pappalardo (2005), Onset of convection in the icy Galilean satellites: Influence of rheology, *J. Geophys. Res.-Planet*, *110*(9), E12005, doi:10.1029/2004JE002371.

Barr, A. C., and L. J. Preuss (2010), On the origin of south polar folds on Enceladus, *Icarus*, *208*, 499–503, doi:10.1016/j.icarus.2010.03.038.

Bassis, J. N., and C. C. Walker (2011), Upper and lower limits on the stability of calving glaciers from the yield strength envelope of ice, *Proc. Royal Soc. A*, *57*, 1–17, doi:10.1098/rspa.2011.0422.

Bassis, J. N., R. Coleman, H. A. Fricker, and J. B. Minster (2005), Episodic propagation of a rift on the Amery Ice Shelf, East Antarctica, *Geophys. Res. Lett.*, *320*, L06,502, doi:10.1029/2004GL022048.

Bassis, J. N., H. A. Fricker, R. Coleman, Y. Bock, J. Behrens, D. Darnell, M. Okal, and J.-B. Minster (2007), Seismicity and deformation associated with ice-shelf rift propagation, *J. Glaciol.*, *53*, 523–536, doi:10.3189/002214307784409207.

Bassis, J. N., H. A. Fricker, R. Coleman, and J.-B. Minster (2008), An investigation into the forces that drive ice-shelf rift propagation on the Amery Ice Shelf, East Antarctica, *J. Glaciol.*, *54*, 17–27, doi:10.3189/002214308784409116.

Belton, M. J. S., et al. (1996), Galileo's First Images of Jupiter and the Galilean Satellites, *Science*, *274*, 377–385, doi:10.1126/science.274.5286.377.

Benthem, J. P., and W. T. Koiter (1973), *Asymptotic approximations to crack problems*, pp. 131–165, Springer.

Beuthe, M. (2008), Thin elastic shells with variable thickness for lithospheric flexure of one-plate planets, *Geophys. J. Int.*, *172*, 817–841, doi:10.1111/j.1365-246X.2007.03671.x.

Billings, S. E., and S. A. Kattenhorn (2005), The great thickness debate: Ice shell thickness models for Europa and comparisons with estimates based on flexure at ridges, *Icarus*, *177*, 397–412, doi:10.1016/j.icarus.2005.03.013.

Black, G. J., D. B. Campbell, and P. D. Nicholson (2001a), Icy Galilean Satellites: Modeling Radar Reflectivities as a Coherent Backscatter Effect, *Icarus*, *151*, 167–180, doi:10.1006/icar.2001.6616.

Black, G. J., D. B. Campbell, and S. J. Ostro (2001b), Icy Galilean Satellites: 70 cm Radar Results from Arecibo, *Icarus*, *151*, 160–166, doi:10.1006/icar.2001.6615.

Bland, M. T., R. A. Beyer, and A. P. Showman (2007), Unstable extension of Enceladus' lithosphere, *Icarus*, *192*, 92–105, doi:10.1016/j.icarus.2007.06.011.

Broek, D., and J. R. Rice (1975), Elementary Engineering Fracture Mechanics, *J. Appl. Mech.*, *42*, 751, doi:10.1115/1.3423697.

Bromirski, P. D., and R. A. Stephen (2012), Response of the Ross Ice Shelf, Antarctica, to ocean gravity-wave forcing, *Ann. Glaciol.*, *53*, 163–172, doi:10.3189/2012AoG60A058.

Bromirski, P. D., O. V. Sergienko, and D. R. MacAyeal (2010), Transoceanic infragravity waves impacting Antarctic ice shelves, *Geophys. Res. Lett.*, *37*, L02502, doi:10.1029/2009GL041488.

Brunt, K. M., E. A. Okal, and D. R. Macayeal (2011), Antarctic ice-shelf calving triggered by the Honshu (Japan) earthquake and tsunami, March 2011, *J. Glaciol.*, *57*, 785–788, doi:10.3189/002214311798043681.

Budd, W. (1966), The dynamics of the Amery Ice Shelf, *J. Glaciol.*, *6*, 335–358.

Bullard, E. C. (1936), Gravity Measurements in East Africa, *Royal Society of London Philosophical Transactions Series A*, *235*, 445–531, doi:10.1098/rsta.1936.0008.

Castelnau, O., P. Duval, M. Montagnat, and R. Brenner (2008), Elastoviscoplastic micromechanical modeling of the transient creep of ice, *J. Geophys. Res.-Solid Earth*, *113*, B11203, doi:10.1029/2008JB005751.

Castillo-Rogez, J., T. V. Johnson, M. H. Lee, N. J. Turner, D. L. Matson, and J. Lunine (2009), ^{26}Al decay: Heat production and a revised age for Iapetus, *Icarus*, *204*, 658–662, doi:10.1016/j.icarus.2009.07.025.

Castillo-Rogez, J. C., M. Efroimsky, and V. Lainey (2011), The tidal history of Iapetus: Spin dynamics in the light of a refined dissipation model, *J. Geophys. Res.-Planets*, *116*, E09008, doi:10.1029/2010JE003664.

Cavalieri, D., C. Parkinson, P. Gloersen, and H. J. Zwally (1996), Sea ice concentrations from nimbus-7 smmr and dmsp ssm/i-ssmis passive microwave data. [2002-2012].

Collins, G. C., and J. C. Goodman (2007), Enceladus' south polar sea, *Icarus*, *189*, 72–82, doi:10.1016/j.icarus.2007.01.010.

Collins, G. C., W. B. McKinnon, J. M. Moore, F. Nimmo, R. T. Pappalardo, L. M. Prockter, and P. M. Schenk (2009), *Tectonics of the outer planet satellites*, pp. 264–350, Cambridge Planetary Science, doi:10.1017/CBO9780511691645.008.

Colman, S. M., E. B. Karabanov, and C. H. Nelson (2003), Quaternary Sedimentation and Subsidence History of Lake Baikal, Siberia, Based on Seismic Stratigraphy and Coring, *J. Sediment. Res.*, *73*, 941–956, doi:10.1306/041703730941.

Cooper, J. F., R. E. Johnson, B. H. Mauk, H. B. Garrett, and N. Gehrels (2001), Energetic Ion and Electron Irradiation of the Icy Galilean Satellites, *Icarus*, *149*, 133–159, doi:10.1006/icar.2000.6498.

Cowles, B. A., A. B. Thakker, and G. E. King (1985), Fracture mechanics of multiple crack initiations: An application for fracture mechanics analyses of gas turbine engine disks, *U.S. Air Force AEDC Technical Library*.

Cox, S. J., and M. J. Cooker (2001), The pressure impulse in a fluid saturated crack in a sea wall, *Coast. Eng.*, *42*, 241–256, doi:10.1016/S0378-3839(00)00062-4.

Craven, M., I. Allison, H. A. Fricker, and R. Warner (2009), Properties of a marine ice layer under the Amery Ice Shelf, East Antarctica, *J. Glaciol.*, *55*, 717–728, doi:10.3189/002214309789470941.

Crawford, G. D., and D. J. Stevenson (1988), Gas-driven water volcanism in the resurfacing of Europa, *Icarus*, *73*, 66–79, doi:10.1016/0019-1035(88)90085-1.

De Angelis, H., and P. Skvarca (2003), Glacier Surge After Ice Shelf Collapse, *Science*, *299*, 1560–1563, doi:10.1126/science.1077987.

Delale, F., and F. Erdogan (1979), Effect of transverse shear and material orthotropy in a cracked spherical cap, *International Journal of Solids and Structures*, *15*(12), 907–926, doi:10.1016/0020-7683(79)90021-0.

Diner, D. J., et al. (2005), The value of multiangle measurements for retrieving structurally and radiatively consistent properties of clouds, aerosols, and surfaces, *Remote Sensing of Environment*, *97*(4), 495–518, doi:10.1016/j.rse.2005.06.006.

Doake, C. S. M., and D. G. Vaughan (1991), Rapid disintegration of the Wordie Ice Shelf in response to atmospheric warming, *Nature*, *350*, 328–330, doi:10.1038/350328a0.

Dombard, A. J., and W. B. McKinnon (2006a), Elastoviscoplastic relaxation of impact crater topography with application to Ganymede and Callisto, *J. Geophys. Res.-Planets*, *111*, E01001, doi:10.1029/2005JE002445.

Dombard, A. J., and W. B. McKinnon (2006b), Folding of Europa's icy lithosphere: an analysis of viscous-plastic buckling and subsequent topographic relaxation, *J. Struct. Geol.*, *28*, 2259–2269, doi:10.1016/j.jsg.2005.12.003.

Durham, W. B., L. A. Stern, and S. H. Kirby (2001), Rheology of ice I at low stress and elevated confining pressure, *J. Geophys. Res.*, *106*, 11,031–11,042, doi:10.1029/2000JB900446.

Efroimsky, M., and V. Lainey (2007), Physics of bodily tides in terrestrial planets and the appropriate scales of dynamical evolution, *J. Geophys. Res.-Planets*, *112*, E12003, doi:10.1029/2007JE002908.

Fagents, S. A. (2003), Considerations for effusive cryovolcanism on Europa: The post-Galileo perspective, *J. Geophys. Res.-Planets*, *108*, 5139, doi:10.1029/2003JE002128.

Fricker, H. A., S. Popov, I. Allison, and N. Young (2001), Distribution of marine ice beneath the Amery Ice Shelf, *Geophys. Res. Lett.*, *28*, 2241–2244, doi:10.1029/2000GL012461.

Fricker, H. A., N. W. Young, I. Allison, and R. Coleman (2002), Iceberg calving from the Amery Ice Shelf, East Antarctica, *Ann. Glaciol.*, *34*, 241–246, doi:10.3189/172756402781817581.

Fricker, H. A., N. W. Young, R. Coleman, J. N. Bassis, and J.-B. Minster (2005), Multi-year monitoring of rift propagation on the Amery Ice Shelf, East Antarctica, *Geophys. Res. Lett.*, *32*, L02502, doi:10.1029/2004GL021036.

Gdoutos, E. E. (1993), *Fracture Mechanics: An Introduction (Solid Mechanics and Its Applications)*, 386-+ pp., Springer.

Giese, B., R. Wagner, H. Hussmann, G. Neukum, J. Perry, P. Helfenstein, and P. C. Thomas (2008), Enceladus: An estimate of heat flux and lithospheric thickness from flexurally supported topography, *Geophys. Res. Lett.*, *35*, L24204, doi: 10.1029/2008GL036149.

Gioia, G., P. Chakraborty, S. Marshak, and S. W. Kieffer (2007), Unified model of tectonics and heat transport in a frigid Enceladus, *Proceedings of the National Academy of Science*, *1041*, 13,578–13,581, doi:10.1073/pnas.0706018104.

Glasser, N. F., and T. A. Scambos (2008), A structural glaciological analysis of the 2002 Larsen B ice-shelf collapse, *J. Glaciol.*, *54*, 3–16, doi: 10.3189/002214308784409017.

Glasser, N. F., B. Kulessa, A. Luckman, D. Jansen, E. C. King, P. R. Sammonds, T. A. Scambos, and K. C. Jezek (2009), Surface structure and stability of the Larsen C ice shelf, Antarctic Peninsula, *J. Glaciol.*, *55*, 400–410, doi: 10.3189/002214309788816597.

Glen, J. W. (1952), Experiments on the deformation of ice, *J. Glaciol.*, *2*, 111–114.

Goldsby, D. L., and D. L. Kohlstedt (2001), Superplastic deformation of ice: Experimental observations, *J. Geophys. Res.*, *106*, 11,017, doi:10.1029/2000JB900336.

Golombek, M. P., and W. B. Banerdt (1986), Early thermal profiles and lithospheric strength of Ganymede from extensional tectonic features, *Icarus*, *68*, 252–265, doi: 10.1016/0019-1035(86)90022-9.

Greeley, R., C. F. Chyba, J. W. Head, III, T. B. McCord, W. B. McKinnon, R. T. Pappalardo, and P. H. Figueredo (2004), *Geology of Europa*, pp. 329–362.

Green, A. E. (1962), On the Linear Theory of Thin Elastic Shells, *Proc. Royal Soc. A*, *266*, 143–160, doi:10.1098/rspa.1962.0053.

Greenberg, R., G. V. Hoppa, B. R. Tufts, P. Geissler, J. Riley, and S. Kadel (1999), Chaos on Europa, *Icarus*, *141*, 263–286, doi:10.1006/icar.1999.6187.

Griggs, J. A., and J. L. Bamber (2011), Antarctic ice-shelf thickness from satellite radar altimetry, *J. Glaciol.*, *57*, 485–498, doi:10.3189/002214311796905659.

Groenleer, J. M., and S. A. Kattenhorn (2008), Cycloid crack sequences on Europa: Relationship to stress history and constraints on growth mechanics based on cusp angles, *Icarus*, *193*, 158–181, doi:10.1016/j.icarus.2007.08.032.

Heeszel, D. S., H. A. Fricker, J. N. Bassis, S. O'Neel, and F. Walter (submitted), Mechanical controls on seismic swarms associated with a propagating ice shelf rift, *J. Geophys. Res.-Earth Surface*.

Helfenstein, P. (2010), Planetary science: Tectonic overturn on Enceladus, *Nat. Geosci.*, *3*, 75–76, doi:10.1038/ngeo763.

Helfenstein, P., J. Veverka, P. C. Thomas, B. Giese, T. Roatsch, T. Denk, G. Neukum, and C. C. Porco (2011), Tectonism and Terrain Evolution on Enceladus: I. Tectonic features and patterns, *Icarus*.

Hindmarsh, R. (1996), Stability of ice rises and uncoupled marine ice sheets, *Ann. Glaciol.*, *23*, 105–115.

Hinrichsen, D. (1999), *The Coastal Population Explosion*, pp. 27–29, National Ocean Service, NOAA.

Hobbs, P. V. (1974), *Ice Physics*, Clarendon Press, Oxford.

Holland, P., H. Corr, D. Vaughan, A. Jenkins, and P. Skvarca (2010), Marine ice in the Larsen Ice Shelf, *Geophys. Res. Lett.*, *36*(6), L11,604, doi:10.1029/2009GL038162.

Hooke, R. (2005), *Principles of Glacier Mechanics*.

Howett, C. J. A., J. R. Spencer, J. Pearl, and M. Segura (2011), High heat flow from Enceladus' south polar region measured using 10-600 cm^{-1} Cassini/CIRS data, *J. Geophys. Res.-Planets*, *116*(E15), E03003, doi:10.1029/2010JE003718.

Huchon, P., E. Gracia, E. Ruellan, M. Joshima, and J.-M. Auzende (1994), Kinematics of active spreading in the central North Fiji Basin (Southwest Pacific), *Mar. Geol.*, *116*(1-2), 69–87, doi:doi:10.1016/0025-3227(94)90169-4.

Huismans, R. S., Y. Y. Podladchikov, and S. Cloetingh (2001), Dynamic modeling of the transition from passive to active rifting, application to the Pannonian basin, *Tectonics*, *20*, 1021–1039, doi:10.1029/2001TC900010.

Hulbe, C. L., C. Ledoux, and K. Cruikshank (2010), Propagation of long fractures in the Ronne Ice Shelf, Antarctica, investigated using a numerical model of fracture propagation, *J. Glaciol.*, *56*, 459–472, doi:10.3189/002214310792447743.

Humbert, A., and D. Steinhage (2011), The evolution of the western rift area of the Fimbul Ice Shelf, Antarctica, *The Cryosphere*, *5*, 1089–1122, doi:10.5194/tcd-5-1089-2011.

Hurford, T. A., P. Helfenstein, G. V. Hoppa, R. Greenberg, and B. G. Bills (2007a), Eruptions arising from tidally controlled periodic openings of rifts on Enceladus, *Nature*, *447*, 292–294, doi:10.1038/nature05821.

Hurford, T. A., A. R. Sarid, and R. Greenberg (2007b), Cycloidal cracks on Europa: Improved modeling and non-synchronous rotation implications, *Icarus*, *186*, 218–233, doi:10.1016/j.icarus.2006.08.026.

Hutter, K., and T. J. Hughes (1984), Theoretical Glaciology, *J. Appl. Mech.*, *51*, 948, doi:10.1115/1.3167761.

Ip, W.-H., A. Kopp, D. J. Williams, R. W. McEntire, and B. H. Mauk (2000), Magnetospheric Ion Sputtering: The Case of Europa and its Surface Age, *Adv. Space Res.*, *26*, 1649–1652, doi:10.1016/S0273-1177(00)00112-5.

IPCC (2007), *Fourth Assessment Report of the Intergovernmental Panel on Climate Change: Climate Change 2007: The AR4 Synthesis Report*, Geneva: IPCC.

Jackson, I., J. D. Fitz Gerald, U. H. Faul, and B. H. Tan (2002), Grain-size-sensitive seismic wave attenuation in polycrystalline olivine, *J. Geophys. Res.-Solid Earth*, *107*, 2360, doi:10.1029/2001JB001225.

Jacobs, S. S., D. R. Macayeal, and J. L. Ardai, Jr. (1986), The recent advance of the Ross Ice Shelf, Antarctica, *J. Glaciol.*, *32*, 464–474.

Jansen, D., B. Kulessa, P. R. Sammonds, A. Luckman, E. C. King, and N. F. Glasser (2010), Present stability of the Larsen C ice shelf, Antarctic Peninsula, *J. Glaciol.*, *56*, 593–600, doi:10.3189/002214310793146223.

Jeffreys, H. (1915), Earth, Viscosity of the, *Monthly Notices of the Royal Astronomical Society*, *75*, 648–658.

Joughin, I., and R. B. Alley (2011), Stability of the West Antarctic ice sheet in a warming world, *Nat. Geosci.*, *4*, 506–513, doi:10.1038/ngeo1194.

Joughin, I., and D. R. MacAyeal (2005), Calving of large tabular icebergs from ice shelf rift systems, *Geophys. Res. Lett.*, *32*, L02501, doi:10.1029/2004GL020978.

Kargel, J. S. (1995), Cryovolcanism on the Icy Satellites, *Earth Moon Planets*, *67*, 101–113.

Kargel, J. S., and S. Pozio (1996), The Volcanic and Tectonic History of Enceladus, *Icarus*, *119*, 385–404, doi:10.1006/icar.1996.0026.

Kieffer, S. W., X. Lu, C. M. Bethke, J. R. Spencer, S. Marshak, and A. Navrotsky (2006), A Clathrate Reservoir Hypothesis for Enceladus' South Polar Plume, *Science*, *314*, 1764–, doi:10.1126/science.1133519.

Kornet, K., M. Różyczka, and T. F. Stepinski (2004), An alternative look at the snowline in protoplanetary disks, *Astron. Astrophys.*, *417*, 151–158, doi:10.1051/0004-6361:20034036.

Lagabrielle, Y., J. Goslin, H. Martin, J.-L. Thirot, and J.-M. Auzende (1997), Multiple active spreading centres in the hot North Fiji Basin (Southwest Pacific): a possible model for Archaean seafloor dynamics?, *Earth Planet. Sc. Lett.*, *149*(1-4), 1 – 13, doi:10.1016/S0012-821X(97)00060-5.

Larour, E., E. Rignot, and D. Aubry (2004), Modelling of rift propagation on Ronne Ice Shelf, Antarctica, and sensitivity to climate change, *Geophys. Res. Lett.*, *31*, L16404, doi:10.1029/2004GL020077.

Lawn, B. (1975), *Fracture of Brittle Solids*, Cambridge Solid State Science Series.

Lazzara, M. A., K. C. Jezek, T. A. Scambos, D. R. MacAyeal, and C. J. van der Veen (1999), On the recent calving of icebergs from the Ross Ice, *Polar Geogr.*, *23*, 201–212, doi:10.1016/j.icarus.2007.07.016.

Lee, S., R. T. Pappalardo, and N. C. Makris (2005), Mechanics of tidally driven fractures in Europa's ice shell, *Icarus*, *177*, 367–379, doi:10.1016/j.icarus.2005.07.003.

Leith, A. C., and W. B. McKinnon (1996), Is There Evidence for Polar Wander on Europa?, *Icarus*, *120*, 387–398, doi:10.1006/icar.1996.0058.

Levison, H. F., M. J. Duncan, K. Zahnle, M. Holman, and L. Dones (2000), NOTE: Planetary Impact Rates from Ecliptic Comets, *Icarus*, *143*, 415–420, doi:10.1006/icar.1999.6313.

Liu, R., C. H. Wang, and R. G. Bathgate (1999), Crack closure in spherical shells, *Int. J. Fracture*, *99*(4), 307–323.

Lopes, M. C., and M. W. Carroll (2008), *Alien Volcanoes*, The Johns Hopkins University Press.

Luckman, A., D. Jansen, B. Kulessa, E. C. King, P. Sammonds, and D. I. Benn (2012), Basal crevasses in Larsen C Ice Shelf and implications for their global abundance, *The Cryosphere*, *6*, 113–123, doi:http://dx.doi.org/10.5194/tc-6-113-2012.

MacAyeal, D. R., et al. (2006), Transoceanic wave propagation links iceberg calving margins of Antarctica with storms in tropics and Northern Hemisphere, *Geophys. Res. Lett.*, *33*, L17502, doi:10.1029/2006GL027235.

Mahadevan, L., R. Bendick, and H. Liang (2010), Why subduction zones are curved, *Tectonics*, *29*(6), doi:10.1029/2010TC002720.

Maimon, O., V. Lyakhovsky, O. Melnik, and O. Navon (2012), The propagation of a dyke driven by gas-saturated magma, *Geophys. J. Int.*, *189*, 956–966, doi:10.1111/j.1365-246X.2012.05342.x.

Manga, M., and C.-Y. Wang (2007), Pressurized oceans and the eruption of liquid water on Europa and Enceladus, *Geophys. Res. Lett.*, *34*, L07202, doi:10.1029/2007GL029297.

Maxwell, J. C. (1867), On the Dynamical Theory of Gases, *Royal Society of London Philosophical Transactions Series I*, *157*, 49–88.

McGrath, D., K. Steffen, H. Rajaram, T. Scambos, W. Abdalati, and E. Rignot (2012), Basal crevasses on the Larsen C Ice Shelf, Antarctica: Implications for meltwater ponding and hydrofracture, *Geophys. Res. Lett.*, *39*, L16504, doi:10.1029/2012GL052413.

McKenzie, D. (1978), Some remarks on the development of sedimentary basins, *Earth Planet. Sc. Lett.*, *40*(1), 25 – 32, doi:10.1016/0012-821X(78)90071-7.

McKinnon, W. B. (2006), On convection in ice I shells of outer Solar System bodies, with detailed application to Callisto, *Icarus*, *183*, 435–450, doi:10.1016/j.icarus.2006.03.004.

McNutt, M. K. (1984), Lithospheric flexure and thermal anomalies, *J. Geophys. Res.*, *89*, 11,180–11,194, doi:10.1029/JB089iB13p11180.

Meehl, G. A., W. M. Washington, W. D. Collins, J. M. Arblaster, A. Hu, L. E. Buja, W. G. Strand, and H. Teng (2005), How Much More Global Warming and Sea Level Rise?, *Science*, *307*, 1769–1772, doi:10.1126/science.1106663.

Meier, M. F. (1984), Contribution of Small Glaciers to Global Sea Level, *Science*, *226*, 1418–1421, doi:10.1126/science.226.4681.1418.

Mighell, K. (2000), Goodness-of-fit Testing of Low-Count Data using the Modified Chi-Square-Gamma Statistic, in *American Astronomical Society Meeting Abstracts*, *Bulletin of the American Astronomical Society*, vol. 32, p. 762.

Mitri, G., and A. P. Showman (2008), Thermal convection in ice-I shells of Titan and Enceladus, *Icarus*, *193*, 387–396, doi:10.1016/j.icarus.2007.07.016.

Miyamoto, H., G. Mitri, A. P. Showman, and J. M. Dohm (2005), Putative ice flows on Europa: Geometric patterns and relation to topography collectively constrain material properties and effusion rates, *Icarus*, *177*, 413–424, doi:10.1016/j.icarus.2005.03.014.

Moore, W. B. (2006), Thermal equilibrium in Europa's ice shell, *Icarus*, *180*, 141–146, doi:10.1016/j.icarus.2005.09.005.

Mottram, R. H., and D. I. Benn (2009), Testing crevasse-depth models: a field study at Breiðamerkurjökull, Iceland, *J. Glaciol.*, *55*, 746–752, doi:10.3189/002214309789470905.

Mueller, D. R., L. Copland, A. Hamilton, and D. Stern (2008), Examining Arctic Ice Shelves Prior to the 2008 Breakup, *EOS Transactions*, *89*, 502–503, doi:10.1029/2008EO490002.

Muller, G., M. Cooker, W. Allsop, T. Bruce, L. Franco, and P. Hull (2000), Numerical Modelling of Impact Pressure Propagation in Cracks, in *Coastal Engineering 2000*, vol. 276, p. 136.

Muller, G., P. Hull, W. Allsop, T. Bruce, M. Cooker, and L. Franco (2002), Wave effects on blockwork structures: model tests, *J. Hydraul. Res.*, *42*(2), 117–124.

Myer, L. R. (2000), Fractures as collections of cracks, *Int. J. Rock Mech. Min.*, *37*(1), 231–243.

Nimmo, F. (2004), Stresses generated in cooling viscoelastic ice shells: Application to Europa, *J. Geophys. Res.-Planets*, *109*(18), E12001, doi:10.1029/2004JE002347.

Nimmo, F. (2008), Tidal Dissipation and Faulting, in *Science of Solar System Ices*.

Nimmo, F., and R. T. Pappalardo (2006), Diapir-induced reorientation of Saturn's moon Enceladus, *Nature*, *441*, 614–616, doi:10.1038/nature04821.

Nimmo, F., and P. Schenk (2006), Normal faulting on Europa: implications for ice shell properties, *J. Struct. Geol.*, *28*, 2194–2203, doi:10.1016/j.jsg.2005.08.009.

Nimmo, F., B. Giese, and R. T. Pappalardo (2003), Estimates of Europa's ice shell thickness from elastically-supported topography, *Geophys. Res. Lett.*, *30*, 1233, doi:10.1029/2002GL016660.

Nimmo, F., J. R. Spencer, R. T. Pappalardo, and M. E. Mullen (2007), Shear heating as the origin of the plumes and heat flux on Enceladus, *Nature*, *447*, 289–291, doi: 10.1038/nature05783.

Nye, J. F. (1957), The Distribution of Stress and Velocity in Glaciers and Ice-Sheets, *Royal Society of London Proceedings Series A*, *239*, 113–133, doi: 10.1098/rspa.1957.0026.

Olgin, J. G., B. R. Smith-Konter, and R. T. Pappalardo (2011), Limits of Enceladus's ice shell thickness from tidally driven tiger stripe shear failure, *Geo. Res. Lett.*, *380*, L02,201, doi:10.1029/2010GL044950.

Ong, L. C. F., R. Cox, and M. Arakawa (2004), Evidence that chaos terrain on Jupiter's moon Europa is formed by crust-penetrating impacts), p. 144.

Ori, G. G., and V. R. Baker (1995), Geological Mechanisms of Resurfacing on Venus (Atalanta and Niobe Planitae, Atropos Tessera, Vesta and UT Rupes), in *Lunar and Planetary Institute Science Conference Abstracts*, *Lunar and Planetary Inst. Technical Report*, vol. 26, p. 1085.

Pappalardo, R. T., and E. Crow-Willard (2010), Tectonized Terrains of Enceladus: The Same but Different, *AGU Fall Meeting Abstracts*, pp. C5+.

Parker, A. P. (1998), Stability of arrays of multiple-edge cracks, *Contractor Reports, US Army Armament Research*.

Parkinson, C. D., M.-C. Liang, Y. L. Yung, and J. L. Kirschivnk (2008), Habitability of Enceladus: Planetary Conditions for Life, *Origins Life Evol. B*, *38*, 355–369, doi:10.1007/s11084-008-9135-4.

Passey, Q. R. (1983), Viscosity of the lithosphere of Enceladus, *Icarus*, *53*, 105–120, doi:10.1016/0019-1035(83)90024-6.

Paterson, W. S. B. (2000), *The Physics of Glaciers, Third Edition*, Butterworth-Heinemann, Oxford.

Patthoff, D. A., and S. A. Kattenhorn (2011), A fracture history on Enceladus provides evidence for a global ocean, *Geophys. Res. Lett.*, *38*, L18201, doi: 10.1029/2011GL048387.

Phillips, C. B., A. S. McEwen, G. V. Hoppa, S. A. Fagents, R. Greeley, J. E. Klemaszewski, R. T. Pappalardo, K. P. Klaasen, and H. H. Breneman (2000), The search for current geologic activity on Europa, *J. Geophys. Res.*, *105*, 22,579–22,598, doi:10.1029/1999JE001139.

Porco, C., D. DiNino, and F. Nimmo (2013), How the Jets, Heat and Tidal Stresses Across the South Polar Terrain of Enceladus are Related, *LPI Contributions*, *1719*, 1775.

Porco, C. C., et al. (2006), Cassini Observes the Active South Pole of Enceladus, *Science*, *311*, 1393–1401, doi:10.1126/science.1123013.

Pritchard, H. D., S. R. M. Ligtenberg, H. A. Fricker, D. G. Vaughan, M. R. van den Broeke, and L. Padman (2012), Antarctic ice-sheet loss driven by basal melting of ice shelves, *Nature*, *484*, 502–505, doi:10.1038/nature10968.

Prockter, L., and P. Schenk (2005), Origin and evolution of Castalia Macula, an anomalous young depression on Europa, *Icarus*, *177*, 305–326, doi: 10.1016/j.icarus.2005.08.003.

Prockter, L. M., and G. W. Patterson (2009), *Morphology and Evolution of Europa's Ridges and Bands*, p. 237.

Qin, R., W. R. Buck, and L. Germanovich (2007), Comment on "Mechanics of tidally driven fractures in Europa's ice shell" by S. Lee, R.T. Pappalardo, and N.C. Makris [2005. Icarus 177, 367 379], *Icarus*, *189*, 595–597, doi:10.1016/j.icarus.2007.01.013.

Rahmstorf, S., G. Foster, and A. Cazenave (2012), Comparing climate projections to observations up to 2011, *Environ. Res. Lett.*, *7*(4), 044,035, doi:10.1088/1748-9326/7/4/044035.

Reissner, E. (1969), On Finite Symmetrical Deflections of Thin Shells of Revolution, *J. Appl. Mech.*, *36*(2), doi:10.1115/1.3564619.

Rhoden, A. R., B. Militzer, E. M. Huff, T. A. Hurford, M. Manga, and M. A. Richards (2010), Constraints on Europa's rotational dynamics from modeling of tidally-driven fractures, *Icarus*, *210*, 770–784, doi:10.1016/j.icarus.2010.07.018.

Rignot, E. (2006), Changes in ice dynamics and mass balance of the Antarctic ice sheet, *Royal Society of London Philosophical Transactions Series A*, *364*, 1637–1655, doi:10.1098/rsta.2006.1793.

Rignot, E., and S. S. Jacobs (2002), Rapid Bottom Melting Widespread near Antarctic Ice Sheet Grounding Lines, *Science*, *296*, 2020–2023, doi:10.1126/science.1070942.

Rignot, E., and R. H. Thomas (2002), Mass Balance of Polar Ice Sheets, *Science*, *297*, 1502–1506, doi:10.1126/science.1073888.

Rignot, E., G. Casassa, P. Gogineni, W. Krabill, A. Rivera, and R. Thomas (2004), Accelerated ice discharge from the Antarctic Peninsula following the collapse of Larsen B ice shelf, *Geophys. Res. Lett.*, *31*, L18401, doi:10.1029/2004GL020697.

Rignot, E., J. L. Bamber, M. R. van den Broeke, C. Davis, Y. Li, W. J. van de Berg, and E. van Meijgaard (2008), Recent Antarctic ice mass loss from radar interferometry and regional climate modelling, *Nat. Geosci.*, *1*, 106–110, doi:10.1038/ngeo102.

Rist, M. A., P. R. Sammonds, S. A. F. Murrell, P. G. Meredith, H. Oerter, and C. S. M. Doake (1996), Experimental fracture and mechanical properties of Antarctic ice: preliminary results, *Ann. Glaciol.*, *23*, 284–292.

Rist, M. A., P. R. Sammonds, H. Oerter, and C. S. M. Doake (2002), Fracture of Antarctic shelf ice, *J. Geophys. Res.-Solid Earth*, *107*, doi:10.1029/2000JB000058.

Roberts, J. H., and F. Nimmo (2008), Near-Surface Heating on Enceladus and the South Polar Thermal Anomaly, in *Lunar and Planetary Institute Science Conference Abstracts*, *Lunar and Planetary Institute Science Conference Abstracts*, vol. 39, p. 1481.

Ross, M. N., and G. Schubert (1987), Tidal heating in an internal ocean model of Europa, *Nature*, *325*, 133, doi:10.1038/325133a0.

Rott, H., W. Rack, P. Skvarca, and H. de Angelis (2002), Northern Larsen Ice Shelf, Antarctica: further retreat after collapse, *Ann. Glaciol.*, *34*, 277–282, doi:10.3189/172756402781817716.

Rudolph, M. L., and M. Manga (2009), Fracture penetration in planetary ice shells, *Icarus*, *199*, 536–541, doi:10.1016/j.icarus.2008.10.010.

Sandwell, D., and G. Schubert (2010), A contraction model for the flattening and equatorial ridge of Iapetus, *Icarus*, *210*, 817–822, doi:10.1016/j.icarus.2010.06.025.

Scambos, T. A., J. Bohlander, and B. Raup (1996), Images of antarctic ice shelves. [2002-2012].

Scambos, T. A., C. Hulbe, and M. Fahnestock (2003), Climate-induced ice shelf disintegration in the Antarctic Peninsula, *Antarct. Res. Ser.*, *79*, 79–92, doi:10.1029/AR079p0079.

Scambos, T. A., J. A. Bohlander, C. A. Shuman, and P. Skvarca (2004), Glacier acceleration and thinning after ice shelf collapse in the Larsen B embayment, Antarctica, *Geophys. Res. Lett.*, *31*, L18402, doi:10.1029/2004GL020670.

Schenk, P., I. Matsuyama, and F. Nimmo (2008), True polar wander on Europa from global-scale small-circle depressions, *Nature*, *453*, 368–371, doi:10.1038/nature06911.

Schenk, P. M. (1989), Crater formation and modification on the icy satellites of Uranus and Saturn - Depth/diameter and central peak occurrence, *J. Geophys. Res.*, *94*, 3813–3832, doi:10.1029/JB094iB04p03813.

Schenk, P. M., and W. B. McKinnon (2009), One-hundred-km-scale basins on Enceladus: Evidence for an active ice shell, *Geophys. Res. Lett.*, *36*, 536–541, doi:10.1029/2009GL039916.

Schenk, P. M., C. R. Chapman, K. Zahnle, and J. M. Moore (2004), *Ages and interiors: the cratering record of the Galilean satellites*, pp. 427–456.

Schlische, R. W. (1991), Half-graben basin filling models: new constraints on continental extensional basin development, *Basin Res.*, *3*(3), 123–141.

Schmidt, B. E., D. D. Blankenship, G. W. Patterson, and P. M. Schenk (2011), Active formation of 'chaos terrain' over shallow subsurface water on Europa, *Nature*, *479*, 502–505, doi:10.1038/nature10608.

Schubert, G., J. D. Anderson, B. J. Travis, and J. Palguta (2007), Enceladus: Present internal structure and differentiation by early and long-term radiogenic heating, *Icarus*, *188*, 345–355, doi:10.1016/j.icarus.2006.12.012.

Schulson, E. M. (1999), The structure and mechanical behavior of ice, *JOM-J. Min. Met. Mat. S.*, *51*(2), 21–27, doi:10.1007/s11837-999-0206-4.

Sergienko, O. V. (2010), Elastic response of floating glacier ice to impact of long-period ocean waves, *J. Geophys. Res.-Earth Surface*, *115*(14), F04028, doi:10.1029/2010JF001721.

Sleep, N. H., J. A. Nunn, and L. Chou (1980), Platform Basins, *Annu. Rev. Earth Pl. Sc.*, *8*, 17, doi:10.1146/annurev.ea.08.050180.000313.

Smith, R. A. (1976), The application of fracture mechanics to the problem of crevasse penetration, *J. Glaciol.*, *17*, 223–228.

Smith, R. A. (1978), *Iceberg cleaving and fracture mechanics - a preliminary survey*, pp. 176–190, Pergamon, New York, NY.

Smith-Konter, B., and R. T. Pappalardo (2008), Tidally driven stress accumulation and shear failure of Enceladus's tiger stripes, *Icarus*, *198*, 435–451, doi:10.1016/j.icarus.2008.07.005.

Solomon, S. C., S. K. Stephens, and J. W. Head (1982), On Venus impact basins - Viscous relaxation of topographic relief, *J. Geophys. Res.*, *87*, 7763–7771, doi:10.1029/JB087iB09p07763.

Spahn, F., et al. (2006), Cassini Dust Measurements at Enceladus and Implications for the Origin of the E Ring, *Science*, *311*, 1416–1418, doi:10.1126/science.1121375.

Spencer, J., C. Howett, J. Pearl, M. Segura, and Cassini Cirs Team (2009a), High-Resolution Observations of Enceladus' Endogenic Thermal Radiation in 2008, *AGU Spring Meeting Abstracts*, p. A4.

Spencer, J. R., J. C. Pearl, C. J. Howett, M. E. Segura, and Cassini Team (2008), High Spatial Resolution Observations of Thermal Emission from Enceladus' Active South Pole, *AGU Fall Meeting Abstracts*, p. B1372.

Spencer, J. R., A. C. Barr, L. W. Esposito, P. Helfenstein, A. P. Ingersoll, R. Jaumann, C. P. McKay, F. Nimmo, and J. H. Waite (2009b), *Enceladus: An Active Cryovolcanic Satellite*, pp. 683–+, doi:10.1007/978-1-4020-9217-6-21.

Spencer, J. R., et al. (2006), Cassini Encounters Enceladus: Background and the Discovery of a South Polar Hot Spot, *Science*, *311*, 1401–1405, doi:10.1126/science.1121661.

Squyres, S. W., R. T. Reynolds, P. M. Cassen, and S. J. Peale (1982), The evolution of Enceladus, *J. Geophys. Res.*, *87*, 7763–7771, doi:10.1029/JB087iB09p07763.

Steffen, K., P. U. Clark, J. G. Cogley, D. Holland, S. Marshall, E. Rignot, and R. Thomas (2008), Rapid changes in glaciers and ice sheets and their impacts on sea level, *Abrupt Climate Change. A Report by the U.S. Climate Change Science Program and the Subcommittee on Global Change Research*, pp. 60–142.

Tada, H., P. C. Paris, and G. R. Irwin (2000), *The Stress Analysis of Cracks Handbook*, 696-+ pp., American Society of Mechanical.

Tanimoto, T. (1997), Bending of spherical lithosphere - axisymmetric case, *Geophys. J. Int.*, *129*, 305–310, doi:10.1111/j.1365-246X.1997.tb01583.x.

Tanimoto, T. (1998), State of stress within a bending spherical shell and its implications for subducting lithosphere, *Geophys. J. Int.*, *134*, 199–206, doi:10.1046/j.1365-246x.1998.00554.x.

Theocaris, P. S., and N. I. Ioakimidis (1977), Numerical integration methods for the solution of singular integral equations, *Quart. Appl. Math.*, *35*(1), 173–187.

Thomas, P. C., et al. (2007), Shapes of the saturnian icy satellites and their significance, *Icarus*, *190*, 573–584, doi:10.1016/j.icarus.2007.03.012.

Thomas, R. H. (1979), The dynamics of marine ice sheets, *J. Glaciol.*, *24*, 167–177.

Timoshenko, S. P., and S. Woinosky-Krieger (1959), *Theory of Plates and Shells, 2nd Ed.*, McGraw-Hill Companies, New York, NY.

Tobie, G., O. Čadek, and C. Sotin (2008), Solid tidal friction above a liquid water reservoir as the origin of the south pole hotspot on Enceladus, *Icarus*, *196*, 642–652, doi:10.1016/j.icarus.2008.03.008.

Tobie, G., et al. (2010), Surface, Subsurface and Atmosphere Exchanges on the Satellites of the Outer Solar System, *Space Sci. Rev.*, *153*, 375–410, doi:10.1007/s11214-010-9641-3.

Turcotte, D. L., R. J. Willemann, W. F. Haxby, and J. Norberry (1981), Role of membrane stresses in the support of planetary topography, *J. Geophys. Res.*, *86*, 3951–3959, doi:10.1029/JB086iB05p03951.

van der Veen, C. J. (1998a), Fracture mechanics approach to penetration of surface crevasses on glaciers, *Cold Reg. Sci. Technol.*, *27*, 31–47, doi:10.1016/S0165-232X(97)00022-0.

van der Veen, C. J. (1998b), Fracture mechanics approach to penetration of bottom crevasses on glaciers, *Cold Reg. Sci. Technol.*, *27*(3), 213–223, doi:10.1016/S0165-232X(98)00006-8.

Van der Veen, C. J., and A. A. Balkema (1999), *Fundamentals of glacier dynamics*, 403-+ pp., CRC Press, Rotterdam, Netherlands.

Vening-Meinesz, F. A. (1950), Les grabens africains, resultat de compression ou de tension dans la croute terrestre, *Bull. Inst. R. Colon. Belge*, *21*, 539–552.

Verbiscer, A., R. French, M. Showalter, and P. Helfenstein (2007), Enceladus: Cosmic Graffiti Artist Caught in the Act, *Science*, *315*, 815–, doi:10.1126/science.1134681.

Walker, C. C., and J. N. Bassis (2011a), Simulations of mechanical failure in ice: Implications of terrestrial fracture models as applied to they icy satellites of the outer solar system, *AGU Fall Meeting Abstracts*, p. A663.

Walker, C. C., and J. N. Bassis (2011b), Bounds on compressional features in Enceladus' ice shell from terrestrial ice sheet models, in *EPSC-DPS Joint Meeting 2011*, p. 1260.

Walker, C. C., J. N. Bassis, and M. W. Liemohn (2012), On the application of simple rift basin models to the south polar region of Enceladus, *J. Geophys. Res.-Planets*, *117*, E07003, doi:10.1029/2012JE004084.

Walker, C. C., J. N. Bassis, H. A. Fricker, and R. J. Czerwinski (submitteda), Decadal variability in Antarctic ice shelf rift propagation, *J. Geophys. Res.-Earth Surface*.

Walker, C. C., J. N. Bassis, H. A. Fricker, and R. J. Czerwinski (submittedb), Variable and intermittent propagation of rifts on the Amery Ice Shelf, East Antarctica, *J. Geophys. Res.-Earth Surface*.

Watts, A. B. (2001), *Isostasy and Flexure of the Lithosphere*, Cambridge University Press, UK.

Weeks, W. F., and G. F. N. Cox (1984), The mechanical properties of ice: A status report, *Ocean Phys. Eng.*, *9*, 135–198.

Weertman, J. (1973), Can a water-filled crevasse reach the bottom surface of a glacier?, *IAHS Publication*, *95*.

Weissel, J. K., and G. D. Karner (1989), Flexural uplift of rift flanks due to mechanical unloading of the lithosphere during extension, *J. Geophys. Res.*, *941*, 13,919–13,950, doi:10.1029/JB094iB10p13919.

Withjack, M. O., R. W. Schlische, and P. E. Olsen (2002), *Rift-basin structure and its influence on sedimentary basins*, pp. 57–81, doi:10.2110/pec.02.73.0057.

Wolters, G., and G. Muller (2004), The propagation of wave impact induced pressures into cracks and fissures, *Geological Society London Engineering Geology Special Publications*, *20*, 121–130, doi:doi:10.1144/GSL.ENG.2004.020.01.09.

Zahnle, K., P. Schenk, L. Dones, and H. Levison (2003), Cratering Rates in the Outer Solar System, in *Lunar and Planetary Institute Science Conference Abstracts*, *Lunar and Planetary Inst. Technical Report*, vol. 34, edited by S. Mackwell and E. Stansbery, p. 1522.